Measurement of the Charged Current Cross Section in Positron–Proton Collisions at HERA

Dissertation
zur
Erlangung der naturwissenschaftlichen Doktorwürde
(Dr. sc. nat.)

vorgelegt der
Mathematisch-naturwissenschaftlichen Fakultät
der
Universität Zürich

von

Nicole Werner

aus
Deutschland

Promotionskomitee

Prof. Dr. Ulrich Straumann (Vorsitz)
Dr. Andrew Mehta
Prof. Dr. Peter Truöl
Dr. Stefania Xella–Hansen

Zürich 2004

To the memory of my father

Abstract

A measurement of the inclusive charged current cross section in positron–proton collisions at a centre–of–mass energy of $\sqrt{s} = 320\,\text{GeV}$ is presented. The data were taken in the years 1999 and 2000 with the H1 detector at HERA and correspond to an integrated luminosity of $\mathcal{L} = 65.25\,\text{pb}^{-1}$. For the kinematic range of four–momentum transfer Q^2 between $300\,\text{GeV}^2$ and $15,000\,\text{GeV}^2$ and Bjørken x between 0.013 and 0.65 the measurements are compared to earlier results and to the Standard Model expectations. The calculation of the theoretical predictions is based on a dedicated NLO QCD analysis performed by the H1 collaboration.

The double differential, single differential and total charged current cross sections are found to be in good agreement with the Standard Model expectation and with former H1 results. For the total charged current cross section in the kinematic region of $Q^2 > 1000\,\text{GeV}^2$ and $y < 0.9$ a value of $\sigma_{CC}^{tot} = (18.11 \pm 0.59(stat.) \pm 1.16(sys.))$ pb is obtained.

A description of the construction and mode of operation of the new central inner multiwire proportional chamber, CIP2k, situated in the centre of the H1 detector is presented in the appendix.

Kurzfassung

Gegenstand der vorliegenden Arbeit ist die Messung des inklusiven Wirkungsquerschnitts für Ereignisse des geladenen Stroms in Positron–Proton Kollisionen bei einer Schwerpunktenergie von $\sqrt{s} = 320\,\text{GeV}$. Die zugrunde liegenden Daten wurden in den Jahren 1999 und 2000 mit dem H1–Detektor an der Speicherringanlage HERA aufgezeichnet und entsprechen einer integrierten Luminosität von $\mathcal{L} = 65.25\,\text{pb}^{-1}$. Die Messungen wurden in einem kinematischen Bereich von Q^2 zwischen $300\,\text{GeV}^2$ und $15,000\,\text{GeV}^2$ und Bjørken x zwischen 0.013 und 0.65 mit früheren Ergebnissen und theoretischen Vorhersagen verglichen. Die theoretischen Erwartungen beruhen auf einer von der H1–Kollaboration durchgeführten NLO QCD Analyse.

Sowohl die doppelt und einfach differentiellen als auch der totale Wirkungsquerschnitt für Ereignisse des geladenen Stroms zeigen keine signifikante Abweichung von den Vorhersagen des Standardmodells. Sie stimmen innerhalb der Fehler gut mit vorherigen H1–Messungen überein. Für den totalen Wirkungsquerschnitt von Ereignissen des geladenen Stroms wurde für den kinematischen Bereich $Q^2 > 1000\,\text{GeV}^2$ und $y < 0.9$ ein Wert von $\sigma_{CC}^{tot} = (18.11 \pm 0.59(stat.) \pm 1.16(sys.))$ pb bestimmt.

Eine Beschreibung der Konstruktion und Funktionsweise der neuen inneren, zentralen Vieldraht–Proportionalkammer, CIP2k, im Zentrum des H1–Detektors findet sich im Anhang.

Contents

Introduction **1**

1 Theoretical Overview of Positron–Proton Scattering at HERA **3**

1.1 Deep–Inelastic Scattering (DIS) . . . 3

1.2 Kinematic Variables of DIS . . . 4

1.3 Electroweak Cross Sections in DIS . . . 5

1.3.1 Structure Functions in the Quark Parton Model (QPM) . . . 8

1.3.2 Comparison of NC and CC Cross Sections . . . 9

1.4 Quantum Chromodynamics . . . 10

1.4.1 Main Assumptions of QCD . . . 12

1.4.2 Renormalisation . . . 12

1.4.3 Factorisation and Evolution Equations . . . 13

2 Technical Aspects of the Measurement **17**

2.1 Overview of the H1 Detector . . . 17

2.2 The Object Oriented Data Analysis Framework . . . 21

2.2.1 The Data Storage . . . 21

2.2.2 The Generic Analysis Tools . . . 22

2.3 Reconstruction of Event Kinematics . . . 23

2.4 Hadronic Energy Measurement . . . 25

2.4.1 Reconstruction of the Hadronic Final State . . . 26

2.4.2 Calibration of the Liquid Argon Calorimeter . . . 26

2.5 Monte Carlo Models . . . 27

3 Data Selection **33**

3.1 Selection of Charged Current Events 33

3.1.1 Trigger Conditions and Efficiencies 34

3.1.2 Kinematic Selection Criteria 36

3.2 Background Rejection 36

3.2.1 Non–ep Background 37

3.2.2 ep Induced Background 40

3.2.3 Visual Scanning 45

3.2.4 Final Event Sample 45

4 Extraction of the Charged Current Cross Section **47**

4.1 Extraction of the Double Differential Cross Section 47

4.1.1 The Binning 47

4.1.2 Determination of the Double Differential Cross Section 50

4.2 Single Differential Cross Sections 51

4.3 Systematic Uncertainties 52

5 Results **55**

5.1 The Double Differential Cross Section 55

5.2 The Single Differential Cross Sections 59

5.2.1 The Q^2 Dependence of the Cross Section 59

5.2.2 The x Dependence of the Cross Section 62

5.3 The Total CC Cross Section σ_{CC}^{tot} 64

Summary and Outlook **65**

A Tables of Results **66**

B The Upgraded Central Inner Proportional Chamber CIP2k 70

B.1 Mode of Operation and Construction of the CIP2k 70

B.1.1 Geometry of the Chamber 71

B.1.2 Readout Electronics 72

B.1.3 Mechanical construction 72

B.1.4 The gas system 73

B.2 High Voltage 75

B.2.1 High Voltage Supply 75

B.2.2 High Voltage Performance 75

Bibliography 79

Introduction

HERA is a lepton–proton collider of 6 km circumference and is hence a unique facility in the world. The leptons, electrons or positrons, circulate with an energy of $28\,\text{GeV}$ whereas the protons have an energy of $920\,\text{GeV}$. The particles collide in two collider experiments, H1 and ZEUS, at a centre–of–mass energy of $320\,\text{GeV}$. In deep–inelastic scattering (DIS) processes a gauge–boson emitted by the lepton couples to a point–like constituent of the proton, a parton. According to the de Broglie relation the four–momentum of the exchanged boson, Q^2, corresponds to its wavelength, $\lambda = 1/\sqrt{Q^2}$ [1] and thus its resolution power with respect to the proton. With the HERA accelerator the accessible range of Q^2 is increased by more than two orders of magnitude compared to earlier fixed target experiments [1]–[6]. This allows to study the proton structure down to distances of $10^{-18}\,\text{m}$, corresponding to about one thousandth of the proton's radius.

In neutral current interactions the exchanged boson is an uncharged photon or Z^0–boson. The outgoing lepton is of the same type as the incoming one. Charged current processes are characterised by the exchange of a charged $W^\pm$ boson and an outgoing neutrino. The study of neutral and charged current processes plays a key role in testing the Standard Model of particle physics, the theory of electroweak and strong interactions. The unification of the electromagnetic and the weak force at an energy scale Q^2 of the Z^0 and $W^\pm$ mass was confirmed by HERA measurements [7, 8]. The theory of strong interactions, Quantum Chromodynamics (QCD), makes predictions about the couplings between the partons. The measurements of the neutral and charged current cross sections are fundamental for the understanding of the proton substructure. They give complementary access to the parton content of a proton. In dedicated QCD analyses the parton distribution functions of the proton could recently be extracted [9, 10].

In this thesis a measurement of the charged current cross section is presented. It is based on data collected by the H1 detector in the years 1999 and 2000 in positron–proton collisions. The data correspond to an integrated luminosity of $65.25\,\text{pb}^{-1}$. Compared to previous measurements [11, 12] in the present analysis reprocessed data, based on a better understanding of the H1 detector, are used for the first time.

For future high precision measurements considerably more data are needed. After the luminosity upgrade of HERA and the collider experiments during the years 2000–2002, the specific

---

[1] In this thesis a system of natural units is used whereby $\hbar = c = 1$. Consequently, energies, momenta and masses are all quoted in units of GeV.

luminosity is expected to increase by a factor of three. In addition polarimeters for polarisation of the beam leptons were installed. This allows for further crucial tests of the Standard Model.

During the upgrade phase the H1 collaboration redesigned and reimplemented the data storage and physics analysis software in a new object oriented framework based on C++. The analysis presented in this thesis was performed in this new software environment and is compared to earlier results. It is an important preparation for future measurements like the first measurement of the charged current cross section as a function of the polarisation of the beam leptons.

As part of the H1 upgrade a new first level z–vertex trigger based on signals of the new central inner multiwire proportional chamber, CIP2k, was installed. An essential part of this thesis was the construction and implementation of the new chamber. Its mode of operation and first performance studies are presented in the appendix.

Chapter 1

Theoretical Overview of Positron–Proton Scattering at HERA

The analysis presented in the following addresses the study of deep–inelastic positron–proton scattering events at HERA, and in particular the extraction of the cross section for charged current processes. The underlying theory for this scattering process at HERA and our current model of the proton structure are presented in this chapter. Rather than being a comprehensive treatment of the theory, it covers the main aspects of HERA kinematics and the motivation for the measurement carried out by the analysis. This analysis is a crucial step for future measurements, as are the upcoming determinations of the charged and neutral current cross sections for polarised lepton beams and improvements on the measurements of parton distribution functions (PDFs). The expressions for the measured cross sections will thus be given as a function of lepton beam polarisation and parton evolution will be introduced.
Comprehensive reviews of deep–inelastic scattering (DIS), the quark parton model (QPM) and quantum chromodynamics (QCD) can be found in [13] and [14], for example.

1.1 Deep–Inelastic Scattering (DIS)

By scattering α–particles off a gold foil Geiger and Marsden observed in 1908 to their surprise that some of the particles were backscattered. Rutherfords consecutive interpretation of atoms being composed of a nucleus and electrons revolutionised the picture of the subatomic world at the beginning of the last century. From then on elastic lepton–proton scattering revealed information about the proton's charge and dimension. However, to study whether protons are elementary particles or whether they are composed of smaller particles, higher energies are needed in order to perform inelastic scattering experiments. According to the de Broglie relation an increase of the momentum of a probe particle corresponds to a decrease of its wavelength and hence an improvement of its resolution power for the study of substructure.

In deep–inelastic lepton–proton[1] scattering processes a boson emitted by the lepton interacts with particles inside the proton and causes its dissociation. In the Standard Model of particle physics (see section 1.3) the interaction can be mediated by four different bosons, namely the electromagnetically interacting photon, γ, and the three weakly interacting bosons, Z_0, and $W^\pm$. Two of them, the electrically neutral γ and Z_0, occur in **N**eutral **C**urrent (NC) ep interactions $ep \to eX$. In NC events the scattered positron and a system of hadrons X form the final state that is measured in the detector. Through the exchange of the charged $W^\pm$ boson **C**harged **C**urrent (CC) $ep \to \nu_e X$ interactions are mediated. The crucial characteristic of CC events is the (anti–)neutrino, $\overset{(-)}{\nu}_e$, in the final state which cannot be detected with the H1 detector. However, the missing transverse momentum can be observed and measured.
A graph of the kinematics for each of these processes is shown in figure 1.1.

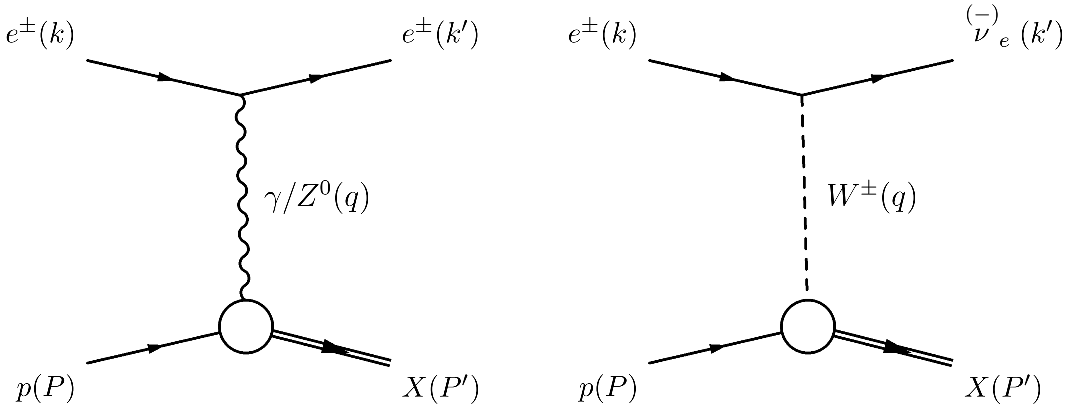

Figure 1.1: *Scattering diagrams for deep–inelastic neutral current (left) and charged current (right) processes.*

1.2 Kinematic Variables of DIS

In figure 1.1 the four–vectors of the incoming lepton and proton are denoted by k and P, respectively. In the final state k' and P' denote the four–momenta of the outgoing lepton and of the system of hadronic particles X, respectively. $q = k - k'$ is the four–momentum carried by the exchanged boson.

Variables that are commonly used for the description of the event kinematics at HERA are the following:

---

[1] In case of HERA the lepton is either an electron or a positron. This analysis is performed with positron data only. It is tried to be as generic as possible here. However, when necessary, focus is put on positrons rather than on electrons.

- The negative four–momentum transfer squared, Q^2, carried by the exchanged boson:

  $$Q^2 = -q^2 = -(k - k')^2 \tag{1.1}$$

  This represents the resolution power of the boson with respect to the proton.

- The inelasticity y:

  $$y = \frac{q \cdot P}{k \cdot P} = 1 - \frac{E'}{E}, \tag{1.2}$$

  where E and E' represent the energies of the incoming and the outgoing lepton, respectively. In the rest frame of the proton this Lorentz invariant variable corresponds to the fraction of the incoming lepton's energy carried by the exchanged boson.

- The Bjørken scaling variable x:

  $$x = \frac{Q^2}{2P \cdot q}. \tag{1.3}$$

  In the Quark Parton Model (s. section 1.3.1) this corresponds to the fraction of proton momentum carried by the parton which is struck by the exchanged boson.

Equations 1.1–1.3 are related to the centre–of–mass energy squared, $s = (k + P)^2$ via the following relation:

$$Q^2 = sxy \tag{1.4}$$

Since the centre–of–mass energy squared, s, is fixed at $\approx 320\,\text{GeV}^2$ for collisions at HERA the event kinematics can be uniquely reconstructed from the measurement of two independent kinematic observables. The reconstruction method is described in section 2.3.
The range of Q^2 and x covered by the HERA collider experiments extends down to $x = 10^{-5}$ and up to $Q^2 = 50,000\,\text{GeV}^2$. This exceeds the kinematic region accessible at fixed target experiments by more than two orders of magnitude in x and Q^2 [1]–[6]. The kinematic plane accessible at HERA and at various fixed target experiments is shown in figure 1.2.

1.3 Electroweak Cross Sections in DIS

Glashow, Weinberg and Salam are regarded as the founders of electro–weak theory, considered as one of the greatest achievements of particle physics in the 20^{th} century. Together with Quantum Chromodynamics (see section 1.4) the Glashow–Weinberg–Salam theory [15] builds the Standard Model of particle physics.

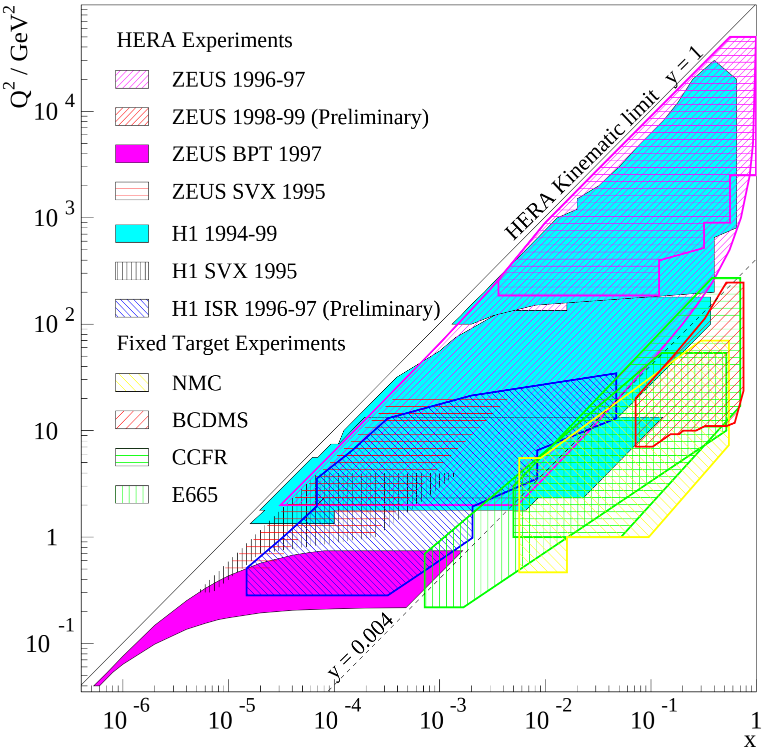

Figure 1.2: *Coverage in kinematic plane (x, Q^2) of various DIS experiments.*

In leading order electroweak theory the differential NC cross section for the scattering of a charged lepton off a nucleus as a function of x and Q^2 can be expressed in terms of three structure functions, $\tilde{F}_2$, $\tilde{F}_L$ and $\tilde{F}_3$:

$$\frac{d^2\sigma_{NC}^{e^\pm p}}{dxdQ^2} = \frac{2\pi\alpha^2}{xQ^4} \cdot \Phi_{NC}^{e^\pm p}, \tag{1.5}$$

with

$$\Phi_{NC}^{e^\pm p} = Y_+\tilde{F}_2 \mp Y_- x\tilde{F}_3 - y^2\tilde{F}_L, \tag{1.6}$$

where $Y_\pm = 1 \pm (1-y)^2$ contains the helicity dependences of the Z^0 exchange. $\Phi_{NC}^{e^\pm p}$ is the so called REDUCED NC CROSS SECTION.

The cross section shows the same characteristic $1/Q^4$ dependence as the Rutherford scattering cross section. Moreover, it is proportional to the fine structure constant squared, α^2, due to the exchange of a virtual photon, γ^*, the dominant contribution at low Q^2. The structure functions $\tilde{F}_i$ parameterise the structure of the proton. $\tilde{F}_2$ and $x\tilde{F}_3$ can be decomposed into five structure functions that are independent of the charge of the incoming lepton [16]: F_2 corresponding to pure photon exchange, $F_2^{Z^0}$ and $xF_3^{Z^0}$ related to Z^0 exchange and the γZ^0 interference terms, $F_2^{\gamma Z^0}$ and $xF_3^{\gamma Z^0}$. The generalised structure functions can be expressed as superpositions:

$$\tilde{F}_2^{\pm} = F_2 + P_Z(-v \mp \lambda a)F_2^{\gamma Z^0} + P_Z^2(v^2 + a^2 \pm 2\lambda va)F_2^{Z^0} \tag{1.7}$$

$$x\tilde{F}_3^{\pm} = P_Z(\pm a + \lambda v)xF_3^{\gamma Z^0} + P_Z^2(\mp 2va - \lambda(v^2 + a^2))xF_3^{Z^0} \tag{1.8}$$

with $v = -1/2 + \sin^2\theta_W$ being the vector coupling and $a = -1/2$ the axial–vector coupling of the Z^0 boson to the lepton, where θ_W is the Weinberg angle. λ denotes the polarisation of the beam leptons.

P_Z is related to the relative amount of Z^0 exchange to contributions from γ exchange:

$$P_Z(Q^2) = \frac{Q^2}{(Q^2 + M_{Z^0}^2)} \frac{1}{4\sin^2\theta_W \cos^2\theta_W}. \tag{1.9}$$

The contribution of the longitudinal structure function $\tilde{F}_L$ to the NC cross section is only significant at high y. It can be decomposed in a similar way as $\tilde{F}_2$. The parity violating structure function $x\tilde{F}_3$ only includes contributions from the γZ^0 interference and from the pure Z^0 exchange. Thus it is small for $Q^2 \ll M_{Z^0}^2$, where Z^0 exchange is negligible.

The inclusive differential charged current cross section for ep interactions can also be expressed in terms of three structure functions $\tilde{W}_2$, $\tilde{W}_3$ and $\tilde{W}_L$:

$$\frac{d^2\sigma_{CC}^{e^\pm}}{dxdQ^2} = \frac{G_F^2}{2\pi x}\Big(\frac{M_W^2}{Q^2 + M_W^2}\Big)^2 \phi_{CC}^{e^\pm}, \tag{1.10}$$

with the reduced CC cross section

$$\phi_{CC}^{e^\pm} = \frac{1}{2}\Big(Y_+\tilde{W}_2^\pm \mp Y_- x\tilde{W}_3^\pm - y^2\tilde{W}_L^\pm\Big), \tag{1.11}$$

where $G_F = \frac{\pi\alpha}{\sqrt{2}\sin^2\Theta_W M_W^2}$ is the Fermi coupling constant and M_W is the mass of the $W^\pm$ boson.

CC interactions are purely weak processes without any contribution from electromagnetic parts. The only gauge boson involved in CC processes is the $W^\pm$. Thus, no interference terms emerge in the decomposition of the generalised structure functions $\tilde{W}_i$ and it only depends on the polarisation λ of the beam leptons:

$$\tilde{W}_2^\pm = P_W^2[(1 \pm \lambda)/2]W_2^\pm \tag{1.12}$$

$$x\tilde{W}_3^\pm = P_W^2[(1 \pm \lambda)/2]xW_3^\pm \tag{1.13}$$

with

$$P_W(Q^2) = \frac{Q^2}{(Q^2 + M_{W^\pm}^2)} \frac{1}{4\sin^2\theta_W}. \tag{1.14}$$

1.3.1 Structure Functions in the Quark Parton Model (QPM)

In 1969 Feynman introduced the parton model in which the proton is made up of constituents named partons. In this model partons are point–like spin–$\frac{1}{2}$ particles which behave like free particles inside the proton. The lepton–proton scattering process can thus be interpreted as a sum of incoherent elastic lepton–parton scattering processes. In case of the cross section for neutral current interactions and neglecting Z^0 exchange this can mathematically be expressed as a sum of elastic eq scattering cross sections:

$$\frac{d\sigma}{dxdQ^2} = \frac{2\pi\alpha^2}{xQ^4}\sum_i \int_0^1 d\xi q_i(\xi) e_i^2 \frac{\xi}{2}[1+(1-y)^2]\delta(x-\xi) \tag{1.15}$$

The summation runs over all partons, q, of flavour i and charge e_i. The probability to probe a parton with proton momentum fraction ξ is $q(\xi)$. An important assumption introduced by Bjørken is that the parton distribution functions q_i (see section 1.4.3) only depend on the dimensionless observable x and do not change with Q^2. This so called BJØRKEN SCALING was first observed at SLAC in 1969 [17] at $x = 0.25$.

Later, when it became evident that the concept of partons was identical with that of the quark picture, the model was referred to as QUARK PARTON MODEL (QPM).

In the QPM structure functions are related to the distribution of quarks inside the proton.

F_2, $F_2^{\gamma Z^0}$ and $F_2^{Z^0}$ are related to the sum of quark and anti–quark momentum distributions, xq and $x\bar{q}$, respectively, whereas $xF_3^{\gamma Z^0}$ and $xF_3^{Z^0}$ are related to their difference:

$$[F_2, F_2^{\gamma Z^0}, F_2^{Z^0}] = x\sum_i [e_i^2, 2e_iv_i, v_i^2 + a_i^2](q_i + \bar{q}_i) \tag{1.16}$$

$$[xF_3^{\gamma Z^0}, xF_3^{Z^0}] = 2x\sum_i [e_ia_i, v_ia_i](q_i - \bar{q}_i), \tag{1.17}$$

where the sum runs over all quark flavours i with $xq_i(x)$ ($x\bar{q}_i(x)$) as the probability of probing a quark q_i (anti–quark $\bar{q}_i$) carrying the momentum fraction x of the proton momentum. The electric charge of the fermions in units of the elementary charge e is denoted by e_i. The vector and axial–vector couplings of the Z^0 to the fermions are denoted by v_i and a_i. The difference $q - \bar{q}$ determines the distribution of valence quarks q_{val}.

At low Q^2 the pure γ exchange dominates the neutral current cross section. For equations 1.7–1.8 this means that the P_Z terms vanish in this kinematic region. The cross section reduces to:

$$\frac{d^2\sigma}{dxdQ^2} = \frac{2\pi\alpha^2}{xQ^4}Y_+\sum_i e_i^2[xq_i + x\bar{q}_i] \tag{1.18}$$

Over the most kinematic region at HERA F_2 dominates, i.e. the contribution from the pure photon exchange. Only at large values of Q^2 first the contribution from the γZ^0 interference (linear in P_Z) and then pure Z^0 exchange (quadratic in P_Z) becomes important and finally dominates the cross section at large Q^2.

In leading order (LO) QCD the structure functions related to the CC cross section, W_2 and W_3 are, depending on the beam lepton charge, sensitive to the sums and differences of quark and anti–quark distributions:

$$\begin{aligned} W_2^+ &= 2x(\bar{U}+D) \quad , \quad W_2^- = 2x(U+\bar{D}) \\ xW_3^+ &= 2x(D-\bar{U}) \quad , \quad xW_3^- = 2x(U-\bar{D}) \end{aligned} \tag{1.19}$$

where xU, xD, $x\bar{U}$ and $x\bar{D}$ are defined as the sum of up–type, down–type, anti–up–type and anti–down–type quark distributions. For processes below the b quark mass threshold, which are dominant at HERA, this means:

$$\begin{aligned} xU &= x(u+c) \\ xD &= x(d+s) \\ x\bar{U} &= x(\bar{u}+\bar{c}) \\ x\bar{D} &= x(\bar{d}+\bar{s}) \end{aligned} \tag{1.20}$$

1.3.2 Comparison of NC and CC Cross Sections

Equations 1.5 and 1.10 indicate that the Q^2 dependence of the NC and CC cross sections arises from the propagator terms. In NC $\frac{d\sigma}{dQ^2} \sim \frac{1}{Q^4}$, due to the dominance of photon exchange. At $Q^2 \approx 100\,\mathrm{GeV}^2$ the cross section is about a factor 1000 larger than the CC cross section because in this kinematic region γ exchange dominates. However, figure 1.3 (left) shows that at $Q^2 \gtrapprox M_Z^2, M_W^2$ both cross sections are of the same order of magnitude, illustrating electro–weak unification in DIS.
In e^-p interactions both cross sections are larger than in the case of e^+p scattering. In NC the positive (negative) γZ^0 interference term in the e^-p (e^+p) interactions is responsible for this effect. It can be employed to measure xF_3 [18]. In CC events this effect comes from the different couplings to the proton valence quarks. W^- bosons are sensitive to u–quarks whereas W^+ bosons couple to d–quarks (see eqs. 1.19). Since protons consist of two u and one d valance quarks the CC cross section for e^-p scattering is higher than for e^+p scattering.

An important feature of charged current interactions is that they are of weak nature exclusively. The charge of the W boson as well as its sensitivity to the parton helicities make charged current interactions particularly well suited to study parton distributions and weak interactions within the Standard Model. As can be seen from equations 1.19, u– and d–quark densities are directly accessible in $e^+p \rightarrow \bar{\nu}_e X$ and $e^-p \rightarrow \nu_e X$ scattering, respectively. In CC interactions a positively (negatively) polarised incoming positron results in a right handed (left handed) W^+ boson. Since in the Standard Model only right handed (left handed) W^+ (W^-) bosons exist the cross section vanishes for left handed (right handed) W^+ (W^-) bosons. A cross section measurement at longitudinal lepton polarisation of $\lambda = -0.5$ and $\lambda = 0.5$ in combination with the measurement presented here could demonstrate the expected linear dependence on polarisation: $\sigma^{CC}_{pol} = (1 \pm \lambda)\sigma^{CC}_{unpol}$ according to equations 1.10-1.13. For e^+p scattering at HERA a prediction is shown in figure 1.3 (right). A measured significant discrepancy from this prediction would be a sign for new physics beyond the Standard Model.

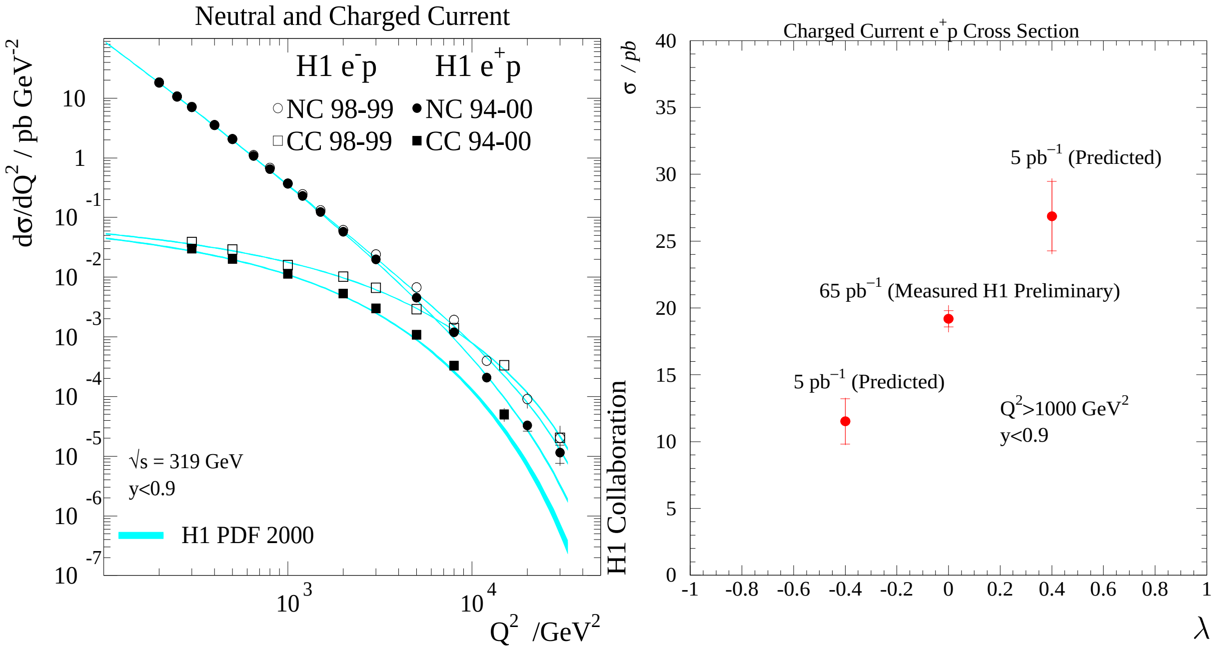

Figure 1.3: *Left: The Q^2 dependence of NC (circles) and CC (squares) cross section $d\sigma/dQ^2$. The results are compared to the corresponding Standard Model expectation using a NLO QCD fit [9]. Right: Predicted dependence of e^+p CC cross section on polarisation of the initial positrons [19]. The statistical uncertainties are calculated using Monte Carlo statistics for an integrated luminosity of 5 pb^{-1} at $\lambda = -0.5$ and $\lambda = 0.5$.*

1.4 Quantum Chromodynamics

At first sight the QPM is very successful in describing the data of DIS experiments. However, some main issues are not addressed by this theory. In order not to violate the Pauli Exclusion Principle for baryons composed of three quarks of the same flavour the concept of colour charge was introduced already in 1965. More striking problems are the contradictory interpretations of the quarks. On the one hand the description of lepton–proton scattering as elastic scattering of leptons off quasi–free quarks is very successfull. This involves the assumption that the bindings between quarks are weak. On the other hand an explanation for the non–existance of free quarks can only be given by the fact that they are strongly bound together in hadrons.

Only five years after Bjørken scaling had been measured at SLAC violations of the scaling behaviour were observed in muon nucleon scattering [20]. F_2 was found to be strongly dependent on Q^2. Figure 1.4 shows a measurement of the structure function F_2 combining H1 results with results from fixed target experiments. As can be seen, the accessible kinematic region of x and Q^2 was significantly expanded by HERA data and scaling violation becomes obvious. For small values of x, F_2 rises strongly with Q^2 whereas for high x values it falls considerably. The scaling observed at SLAC emerges at medium x of ≈ 0.25.

Since the proton structure function F_2 is directly sensitive to the parton distributions inside the proton according to equation 1.16, these can no longer be assumed to be independent of Q^2. Thus the quark and anti–quark momentum distributions of quark flavour i become $xq_i(x, Q^2)$

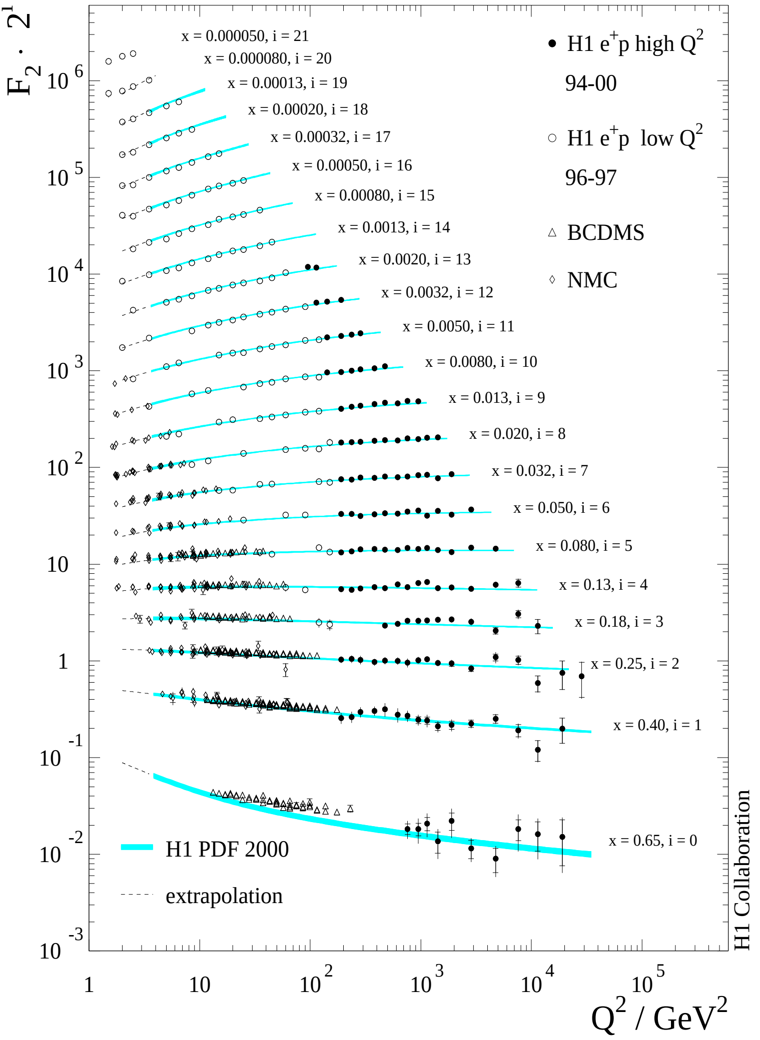

Figure 1.4: *The proton structure function F_2 measured in lepton–proton scattering at H1 and at fixed target experiments BCDMS [2] and NMC [5]. The data are compared with the corresponding Standard Model expectation using a NLO QCD fit [9].*

and $x\bar{q}_i(x, Q^2)$. Another indication for the need of a more comprehensive model was the fact that the partons were found to carry only about 50% of the proton's momentum. To cope with this observation more constituents of the proton needed to be introduced, namely the gluons.

These problems can be understood in the framework of a non–abelian gauge theory of strong interactions, QUANTUM CHROMODYNAMICS (QCD).

1.4.1 Main Assumptions of QCD

QCD is a field theory to describe interactions between quarks and gluons. Its main assumptions are:

- Every quark flavour exists in three different colours (colour charge).
- The interaction is invariant under colour exchange, i.e. it is invariant under $SU(3)$ transformations.
- The net colour charge of all hadrons is neutral.
- Only particles which have a neutral net colour charge can exist as free particles. Quarks and gluons carry colour and therefore only exist in bound states (CONFINEMENT).

1.4.2 Renormalisation

The gauge bosons that mediate the strong force are the massless gluons. They couple to quarks, as depicted in figure 1.5(a)-(b), and thus mediate forces between them. In contrast to the equally massless photon they couple among themselves due to their colour charge. The gluon's self coupling results in a strong dependence of the strong coupling constant, α_s, on the hardness of the interaction which corresponds to Q^2 and is also referred to as energy scale. Analogous to the fine structure constant, α, in QED, α_s is a fundamental constant in QCD that has to be determined from experiment. At large scales, i.e. small distances or high Q^2 the quarks can be regarded as free particles. In this region of so called ASYMPTOTIC FREEDOM the coupling between quarks and gluons is small and perturbation theory is applicable.

In higher orders gluon self coupling leads to infinite contributions arising from quark and gluon loops depicted in figure 1.5 (b)-(c). A renormalisation procedure is needed to account for these so called ULTRAVIOLET DIVERGENCES. This procedure requires the introduction of a RENORMALISATION SCALE, μ_r, at which the integration over contributing loops is cut off and terms of higher order are subtracted. Physical observables $\mathcal{O}$, however, must not depend on the arbitrary scale μ_r. This requirement leads to the RENORMALISATION GROUP EQUATION:

$$\mu_r^2 \frac{\delta \mathcal{O}}{\delta \mu_r^2} + \mu_r^2 \frac{\delta \alpha_s}{\delta \mu_r^2} \frac{\delta \mathcal{O}}{\delta \alpha_s} = 0. \tag{1.21}$$

As a consequence the coupling constant α_s depends on the choice of the renormalisation scale μ_r. For further details on the renormalisation procedure see [13], for example.

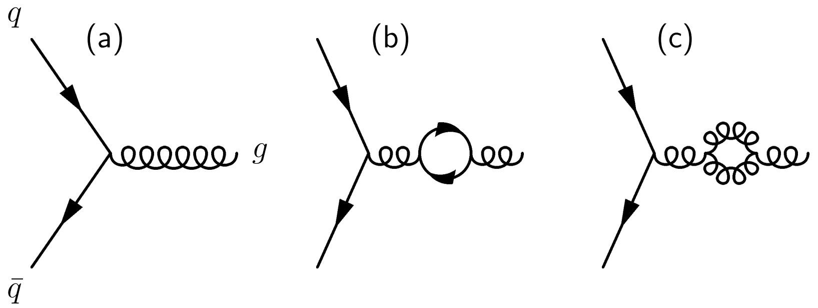

Figure 1.5: *Feynman diagrams related to gluon coupling. (a) shows a graph of order α_s. Processes depicted in (b) and (c) are of the order of α_s^3. These and higher order processes give rise to ultraviolet divergencies.*

1.4.3 Factorisation and Evolution Equations

Although so far it is not possible to calculate the lepton–proton scattering cross section, and so the structure of the proton, from first principles, the FACTORISATION THEOREM OF QCD delivers an ansatz to determine the parton distributions inside the proton. Deep–inelastic lepton–proton scattering is still considered as a sum of incoherent lepton–parton scatterings as given in equation 1.15 for the QPM. By folding this perturbatively calculable lepton–proton cross section with initial PARTON DISTRIBUTION FUNCTIONS $f_{q_i/p}$, giving the density of partons q_i in the proton p at a reference scale Q_0^2, the cross section can be factorised as given in the following:

$$\sigma_{ep} = \sum_{q_i} [\sigma_{eq_i} \otimes f_{q_i/p}(x)] \tag{1.22}$$

An intuitive picture of the summation is shown in figure 1.6 in form of a scattering diagram.

The initial parton distributions $f_{q_i/p}(x)$ denote the probability densities to resolve a quark q_i carrying proton momentum fraction x. They cannot be calculated but have to be determined experimentally. They are, however, universal, i.e. they are defined process independent and depend only on the hadron they belong to. Hence, once measured for one reaction they can be employed for the calculation of other interaction processes.

The calculation of the cross section for lepton–parton interaction, σ_{eq_i}, turns out to be sophisticated since higher order corrections are divergent. One type of divergencies evolve from radiation of soft gluons with small momenta $k \to 0$. These can be cancelled with virtual corrections to those processes without soft gluon emissions. Another type are the so called INFRARED DIVERGENCIES due to collinear emission of gluons with small transverse momenta $k_\perp \to 0$ radiated off the partons q_i. These can be regulated and absorbed into the parton distribution functions (PDFs) in order to get a finite result. By this procedure the PDFs become dependent on the FACTORISATION SCALE μ_f similar to the way absorption of ultraviolet divergencies leads to a dependence of the strong coupling constant, α_s, on the RENORMALISATION SCALE. For all $k_t < \mu_f$ the parton emissions are included in the PDFs $f_{q_i/p}$.

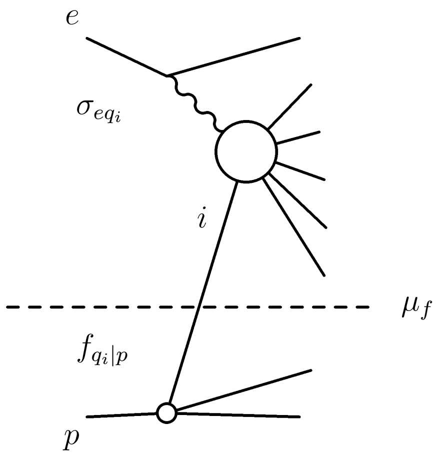

Figure 1.6: *In deep–inelastic ep scattering the cross section can be factorised into a perturbatively calculable lepton–parton cross section σ_{eq_i} and parton distribution functions $f_{q_i/p}$ with a factorisation scale μ_f.*

Figure 1.7 provides a visualisation of the factorisation process. Thereby also the electron–parton scattering cross sections with removed divergencies depend on the factorisation scale μ_f and the ep cross section becomes:

$$\sigma_{ep} = \sum_i [\sigma_{eq_i}(\mu_f^2) \otimes f_{q_i/p}(x, (\mu_f^2))] \tag{1.23}$$

Analogous to the renormalisation procedure, in the factorisation procedure observables must not depend on the scale μ_f. The analogue to the renormalisation group equation which leads to a dependence of α_s on μ_r is given by the Dokshitzer–Gribov–Lipatov–Altarelli–Parisi DGLAP PARTON EVOLUTION EQUATIONS [21]. This system of coupled differential equations comprises the dependence of parton distribution functions on μ_f. Choosing Q^2 as the factorisation scale the evolution equations for quark distribution f_{q_i} of flavour i and the gluon distribution f_g are:

$$\frac{df_{q_i}(x,Q^2)}{d\ln Q^2} = \frac{\alpha_s(Q^2)}{2\pi} \int_x^1 \frac{d\xi}{\xi} [\sum_i P_{qq}(\frac{x}{\xi}) f_{q_i}(\xi, Q^2) + P_{qg}(\frac{x}{\xi}) f_g(\xi, Q^2)] \tag{1.24}$$

$$\frac{df_g(x,Q^2)}{d\ln Q^2} = \frac{\alpha_s(Q^2)}{2\pi} \int_x^1 \frac{d\xi}{\xi} [\sum_i P_{gq}(\frac{x}{\xi}) f_{q_i}(\xi, Q^2) + P_{gg}(\frac{x}{\xi}) f_g(\xi, Q^2)] \tag{1.25}$$

The SPLITTING FUNCTIONS $P_{qq}(z), P_{qg}(z), P_{gq}(z)$ and $P_{gg}(z)$ are calculable perturbatively. In leading order, $P_{ba}(z)$ is related to the probability for parton a to split into partons b and c carrying momentum fractions z and $1-z$, respectively. All four vertices are depicted in figure 1.8.

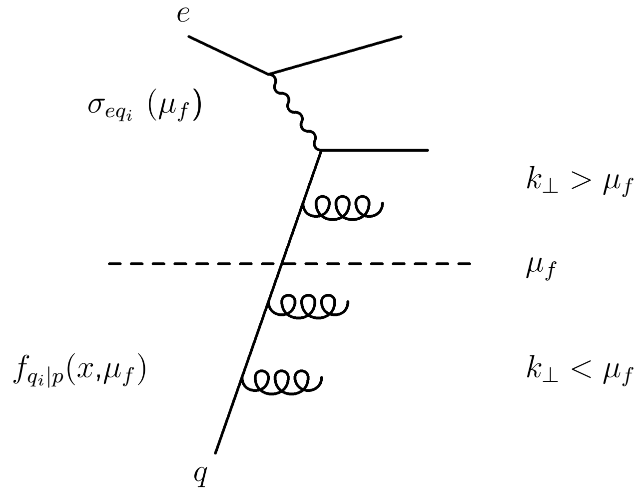

Figure 1.7: *Diagram of soft gluon emissions that contribute to infrared divergencies. The factorisation scale is μ_f. For transverse momenta $k_\perp < \mu_f$ parton emissions are included in the PDFs $f_{q_i/p}$.*

Once the parton distribution functions are determined at fixed reference scale, Q_0^2, the DGLAP equations can be used to predict how they evolve for increasing values of Q^2. The x dependence of the PDFs is not delivered by the DGLAP evolution but has to be parameterised at fixed Q_0^2. For the determination of the free parameters, fits to measured structure functions are performed. Figure 1.9 shows the latest H1 measurement on parton distribution functions [9] compared to latest theoretical predictions from the MRST [22] and CTEQ [23] collaborations.

For a precise determination of the proton structure functions and the extraction of PDFs at HERA a very accurate measurement of the NC and CC cross sections is essential. Moreover, the CC cross section measurement allows us to directly test the linear dependence of the cross section on the lepton polarisation and thus the electroweak theory as part of the Standard Model, as soon as HERA II starts running with polarised lepton beams.

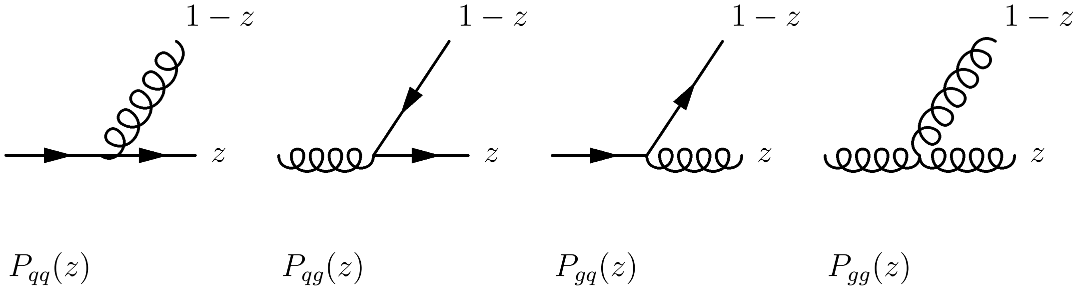

Figure 1.8: *Leading order diagrams contributing to the splitting functions P_{ba}.*

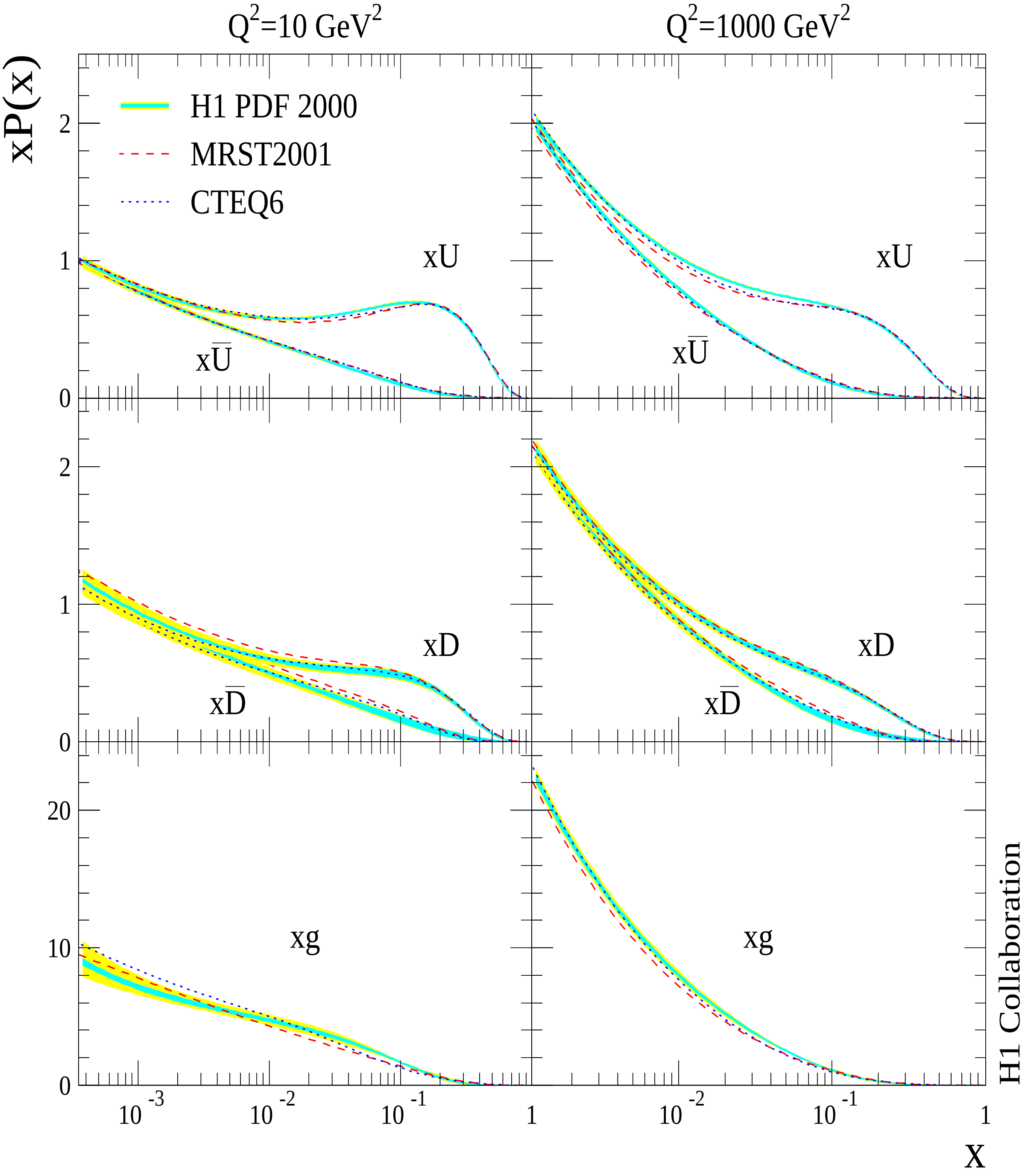

Figure 1.9: *Parton distributions as determined from H1 fit to H1 data only. The distributions are shown at* $Q^2 = 10\,\mathrm{GeV}^2$ *(left) and* $Q^2 = 1000\,\mathrm{GeV}^2$ *(right). For comparison theoretical predictions from the MRST [22] and CTEQ [23] collaborations are shown.*

Chapter 2

Technical Aspects of the Measurement

The H1 detector is one out of two collider experiments at the lepton–proton storage ring **H**adron–**E**lektron–**R**ing–**A**nlage (HERA) at **D**eutsches **E**lektronen–**Sy**nchrotron (DESY) in Hamburg. Bunches of leptons, electrons or positron, and protons fly in opposite direction in two rings of a circumference of 6.3 km. Every 96 ns the bunches are brought to collision inside the two detectors. In case of deep–inelastic scattering (see section 1.1) the proton splits up and hadrons and leptons are produced. The purpose of the detectors H1 and ZEUS is to measure these final state particles.

The chain from detector signals to the reconstructed event kinematics is highly complex and involves many steps. In this chapter the main steps from data taking and data storage to reconstruction of event kinematics are outlined. Thereafter, techniques for the reconstruction of the hadronic final state and for the calibration of the LAr calorimeter are presented. Finally the Monte Carlo models used for the theoretical description of the measurement and for the determination of detector acceptance and efficiencies are introduced.

2.1 Overview of the H1 Detector

The construction of the H1 detector follows the principle of a modern collider experiment. Its peculiarity is its asymmetric assembly due to the different beam energies of leptons (27.5 GeV) and protons (920 GeV): There is more instrumentation in the proton direction.
A side view of the H1 detector with components relevant for the reconstruction of charged current events is shown in figure 2.1. The H1 coordinate system is indicated with positive z-axis in direction of the proton beam. The polar angle θ is measured with respect to this axis.

The main components from inside outwards are: The central tracking chambers and chambers for measuring tracks in direction of the proton beam. These are surrounded by electromagnetic and hadronic calorimeters with almost 4π solid angle coverage. The calorimetry consists of a **L**iquid **Ar**gon **Cal**orimeter (LArCal) in the central region, a lead–scintillator fibre calorimeter

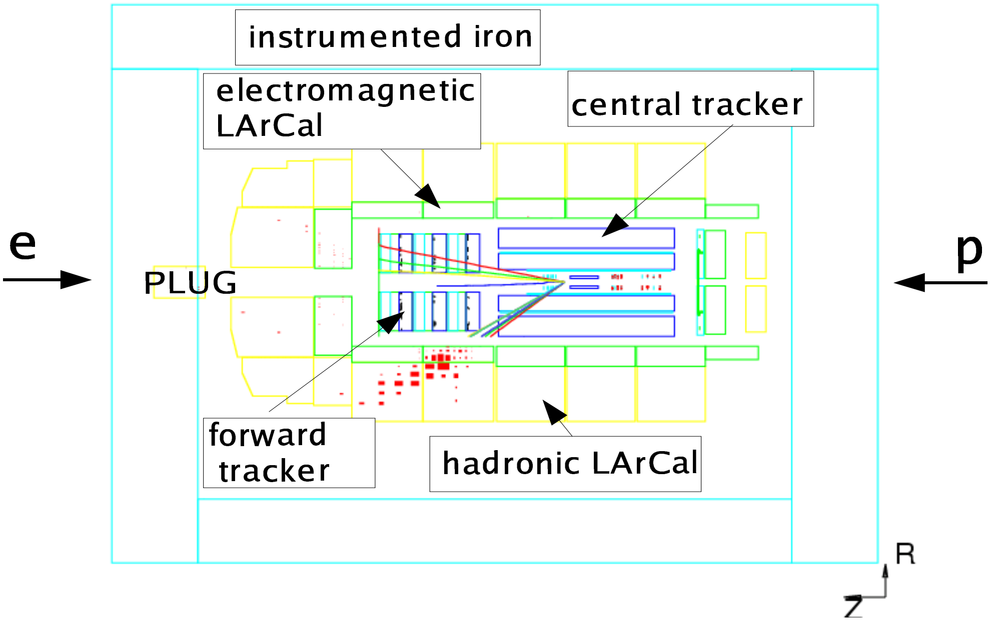

Figure 2.1: *An overview of the components of the H1 detector relevant for this analysis.*

(SpaCal) in direction of the lepton beam and a silicon instrumented sampling calorimeter (PLUG) in direction of the proton beam. The outer detector part consists of several layers of instrumented iron for muon detection. A detailed description of the H1 detector can be found elsewhere [24, 25].

The Central Tracking System

The central tracking system is composed of two cylindrical multiwire proportional chambers (CIP and COP), two z drift chambers (CIZ and COZ) and two jet chambers (CJC1 and CJC2), as shown in figure 2.2. Closest to the beam pipe two silicon trackers (CST and BST) provide signals for secondary vertex measurements.

The **C**entral **I**nner and **C**entral **O**uter **P**roportional Chambers CIP and COP [26] are mainly used for triggering purposes (see appendix B). The **C**entral **I**nner and **C**entral **O**uter $\boldsymbol{z}$ chambers [27, 28] are drift chambers that provide an accurate measurement of the z position of tracks. The two **C**entral **J**et **C**hambers CJC1 and CJC2 [29] are designed to provide an accurate track measurement in the $r - \phi$ plane.

The central tracking system covers the angular region of $12^\circ \leq \theta \leq 155^\circ$. The spacial resolution of the jet chambers is $\sigma_{r\phi} = 170\,\mu$m in $r\phi$ and $\sigma_z = 22\,$mm in z. For the z chambers the corresponding quantities are $\sigma_{r\phi} = 25$ and $58\,$mm and $\sigma_z = 350\,\mu$m [25].

The Forward Tracking System

The forward tracking system provides detection of tracks in forward direction with an angular coverage of $7^\circ \leq \theta \leq 25^\circ$. Its angular and momentum resolutions are $\sigma_{\theta\phi} = 1$ mrad and $\sigma_p/p^2 = 0.03/$ GeV, respectively [30].

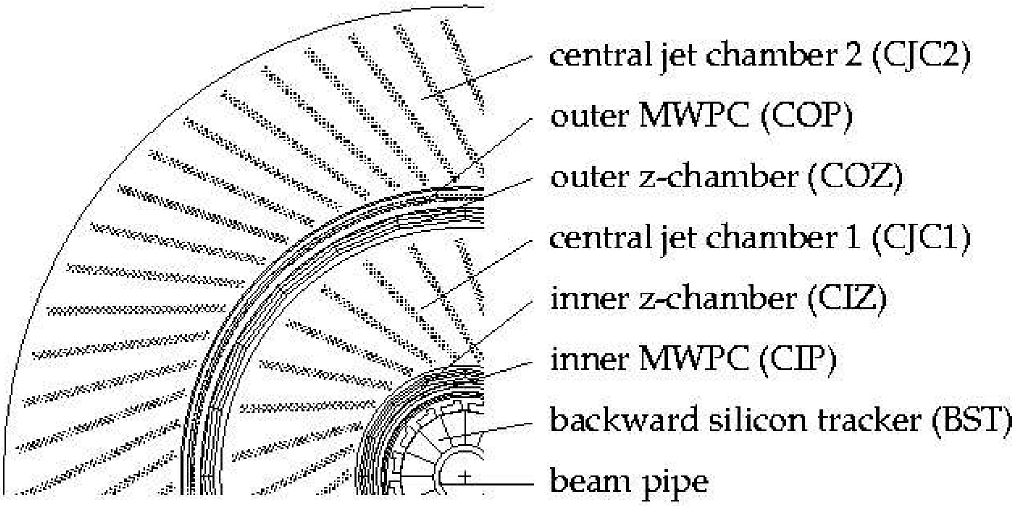

Figure 2.2: *The central tracking system of the H1 detector.*

The Liquid Argon Detector

In the measurement presented here the LArCal takes the leading part in measuring the four vector p_h of the hadronic final state.

The LArCal covers the angular region of $4^\circ \leq \theta \leq 154^\circ$. It consists of eight individual wheels as shown in figure 2.3 (a), five forming the central and forward barrel region of the detector, an inner and outer forward part (IF and OF) and a backward barrel part (BBE). All wheels apart from the outer forward and the backward part consist of an electromagnetic and a hadronic section. The OF consists of a hadronic part only, and the BBE only of an electromagnetic section. In ϕ each wheel is segmented into eight octants as shown in figure 2.3 (b).

The LArCal is a non–compensating sampling calorimeter. It is designed to provide clear particle identification of electrons muons and neutral particles, as well as to measure high–energetic hadronic jets. For this purpose it has a high granularity of 44,000 cells. Each cell consists of absorber plates, liquid argon as active medium, a readout plane and a high voltage plane. The absorber medium in the electromagnetic part is lead which results in the electromagnetic showers being usually entirely contained within this part. The granularity of the electromagnetic part is higher than that of the hadronic part because of the compact structure of electromagnetic showers. The thickness of the absorber plates corresponds to 20 to 30 radiation lengths. The energy resolution of the electromagnetic part of the LArCal was measured to be $\sigma_{em}/E = 0.11/\sqrt{E[\text{GeV}]} \oplus 0.01$ for electrons [31].
In the hadronic part stainless steel is used as absorber medium. The material thickness corresponds to five to eight interaction lengths. The LArCal is non–compensating with a charge output for hadrons being about 30% smaller than that for electrons. The signals measured within the hadronic part of the calorimeter have thus to be corrected offline to the signals measured in the electromagnetic part. The energy resolution of the hadronic part was found to be $\sigma_{had}/E = 0.50/\sqrt{E[\text{GeV}]} \oplus 0.02$ for charged pions in a test beam [31].

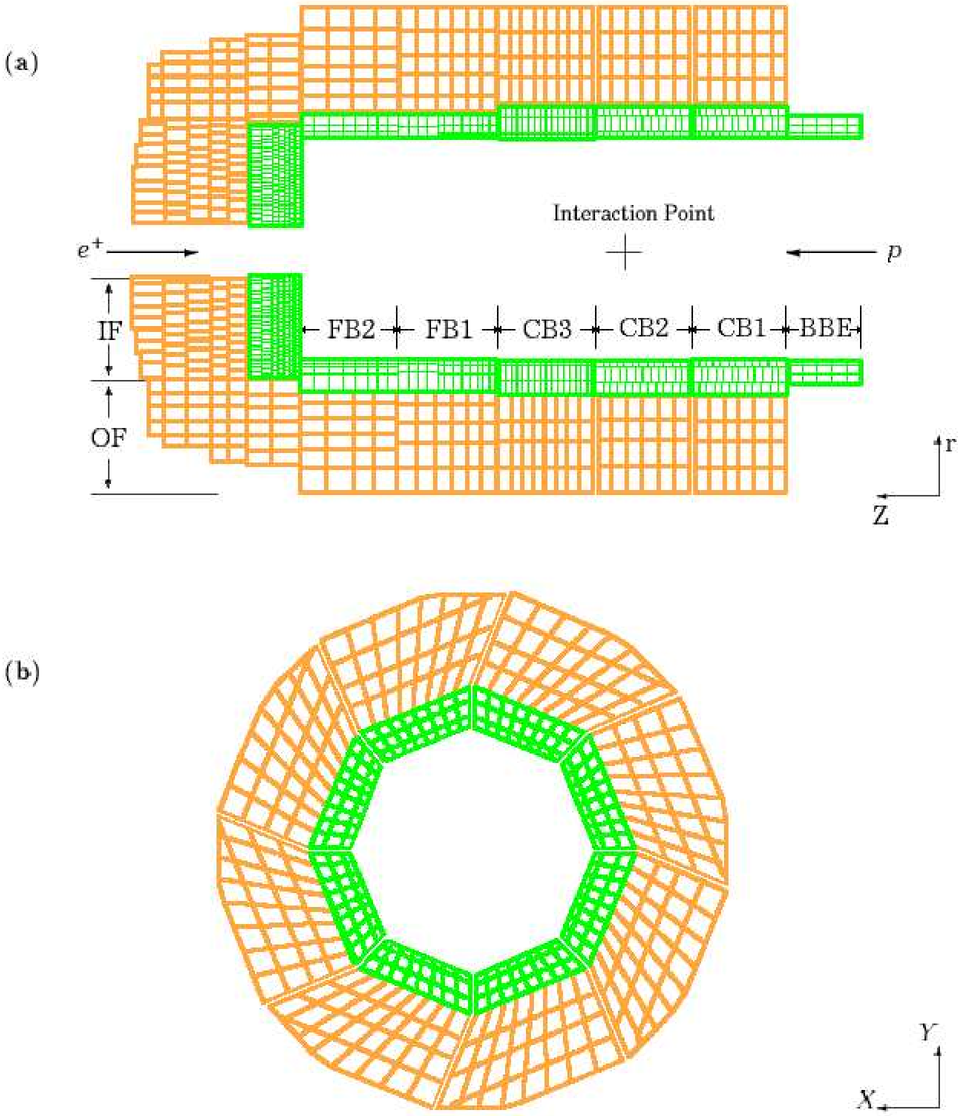

Figure 2.3: *The Liquid Argon Calorimeter. (a) The wheel structure and (b) the octant structure of a wheel.*

The PLUG Calorimeter

The PLUG calorimeter covers the very forward region of $0.6^\circ \leq \theta \leq 3.5^\circ$. It fills the gap in acceptance between the beampipe and the LArCal in order to minimise the loss of transverse momentum in forward direction. The PLUG is also a sampling calorimeter with copper as absorber material and silicon as active medium. Due to the large amount of dead material in forward direction the resolution of the PLUG calorimeter is rather poor. It was measured to be $\sigma/E = 1.0/\sqrt{E[\text{GeV}]}$ [32].

2.2 The Object Oriented Data Analysis Framework

In case an ep event is triggered by the H1 trigger system [24, 33] full detector information is stored on raw data tapes. This information is used for full event reconstruction and classification using the H1REC [34] software package. The subsequent output is written to **P**roduction **O**utput **T**apes (POTs) and a reduced version is written to **D**ata **S**torage **T**apes (DSTs).

During the preparation and upgrade phase for HERA II a new H1 software environment H1 OO based on ROOT [35] and object oriented programming in C++ was designed and implemented. The main goals of this sophisticated change from already established software tools to new software are:

- Provide a modern and extendable framework with standardised physics algorithms that can be incorporated and supported by all H1 physics analyses.
- Attract new students with a modern programming environment.

Hence, common event information storage is as well taken care of as implementation of generic physics analysis tools.
The so far used programs FPACK, BOS, HBOOK and PAW [36] are replaced by ROOT which includes efficient storage, analysis and graphics display facilities.

2.2.1 The Data Storage

The physics data are stored in a three–layer system. The first level, ODS, is produced by conversion of DST files such that the contents are 1–to–1 equivalent for both storage types. The ODS contains reconstructed tracks, clusters and detector–level information. Micro–ODS (μODS) as the second level is designed to allow fast access to particle information, as are electromagnetic and hadronic particles, their four–vectors and the scattered lepton, for example. As a third level the H1 Analysis Tag (HAT) contains event–level information like z–vertex position, run number and trigger information, for example. The HAT variables are stored in simple types as bytes, shorts, integers or floats which makes HAT files approximately four times smaller than μODS files and substantially smaller than ODS, allowing a very fast preselection of events.
For a certain event, information of all levels can be accessed by the user. The relations between the different levels for a given event is managed by the H1TREE class.
For information that is not stored in the official HAT and μODS files users can add a USER–TREE to persistently store any information he or she needs. This is faster than accessing ODS information, especially because the USER–TREE can be filled for a subsample of events only. Detailed information about the H1 OO project can be found in the internal document [37] and in [38]. A diagram of the H1 OO storage levels is shown in figure 2.4.

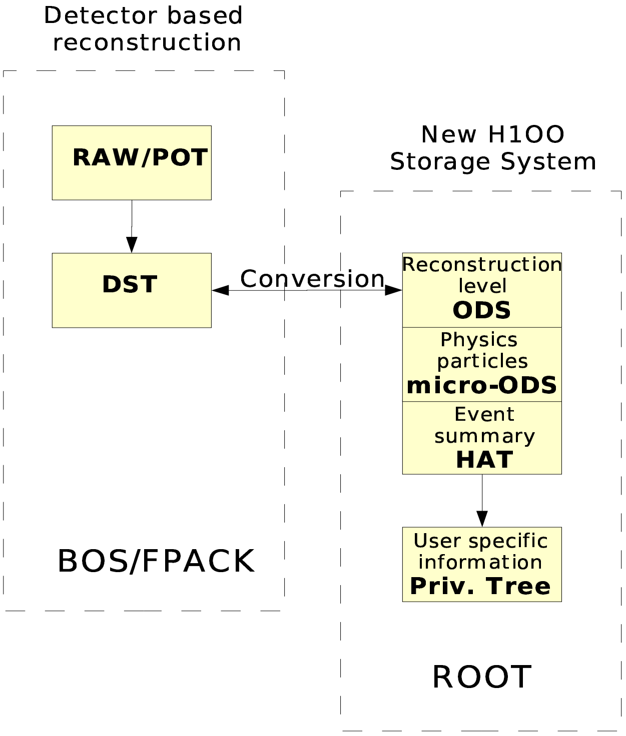

Figure 2.4: *Schematic overview of the different storage levels.*

2.2.2 The Generic Analysis Tools

Many analysis steps are generic for all kinds of physics analyses. Therefore tools have been developed which can be shared by different users and be adapted to their special analyses. The analysis presented here is performed in a new analysis framework which is based on the described new data storage system. It provides the user with additional event information calculated from variables on μODS and HAT by the H1CALCULATOR class. These calculated variables include event kinematic variables described in section 2.3. Also necessary for most analyses are event weightings regarding luminosity weights and trigger weights, for example. This is also implemented in the H1CALCULATOR class. Several manager classes take care of common analysis steps such as file management, event selection, histogram filling and binning. For a detailed description of the H1 generic OO analysis framework refer to [38]. A schematic overview of the analysis framework used for the following analysis is shown in figure 2.5.

The analysis presented here has been performed in the described new H1 OO analysis framework and compared to results obtained with the former Fortran–based H1 analysis package H1PHAN [39].

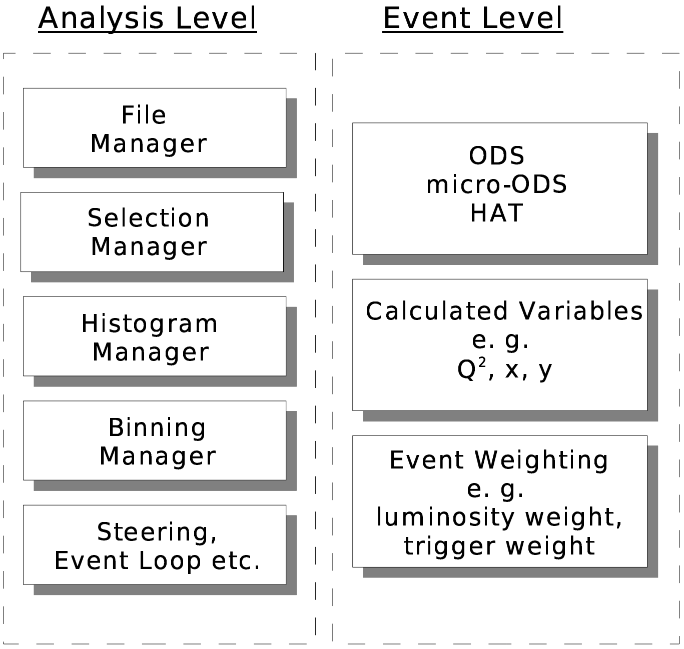

Figure 2.5: *Schematic overview of the analysis framework.*

2.3 Reconstruction of Event Kinematics

The kinematics of ep interaction events can be determined from either the lepton information alone, or from the measured hadronic system alone, or from a combination of both, permitting important systematic cross-checks and detector calibration. The measurement of the hadronic system relies mostly on the calorimetry.

The Hadron Method: For events without a scattered lepton measured in the detector, like charged current events for example, this method has to be applied. The kinematics are exclusively reconstructed from the information from the hadronic final state:

$$y_h = \frac{E_h - p_{z,h}}{2E_e}, \tag{2.1}$$

$$Q_h^2 = \frac{p_{x,h}^2 + p_{y,h}^2}{1 - y_h}. \tag{2.2}$$

The energy of the incoming lepton is denoted by E_e. The four–vector components of the hadronic system h are calculated as the four–momentum sum over all final state hadrons. They are denoted by E_h, $p_{x,h}$, $p_{y,h}$ and $p_{z,h}$. The hadron method relies on the assumption that the contribution from hadrons lost in the beam pipe is negligible [40]. It is the only method applicable in charged current events.

For neutral current events the kinematic variables can be reconstructed by various methods since the measurement of the scattered lepton provides redundant information.

THE ELECTRON METHOD: In this method the kinematic variables are calculated exclusively from the measured energy E'_e and angle θ_e of the scattered lepton:

$$y_e = 1 - \frac{E'_e}{E_e} \sin^2 \frac{\theta_e}{2}, \tag{2.3}$$

$$Q^2_e = 4E'_e E_e \cos^2 \frac{\theta_e}{2} = \frac{E'_e \sin^2 \theta_e}{1 - y_e} = \frac{p^2_{T,e}}{1 - y_e}, \tag{2.4}$$

where $p_{T,e}$ denotes the transverse momentum of the scattered lepton.

An additional method used for the reconstruction of neutral current events is THE DOUBLE ANGLE METHOD: For event reconstruction both, information from the scattered lepton and from the hadronic final state are used. The angle γ_h is defined as the azimuthal angle of the hadronic final state. In the quark parton model (see section 1.3.1) it is the angle of the scattered quark:

$$\cos \gamma_h = \frac{p^2_{T,h} - (E_h - p_{z,h})^2}{p^2_{T,h} + (E_h - p_{z,h})^2}, \tag{2.5}$$

where $p_{T,h} = \sqrt{p^2_{x,h} + p^2_{y,h}}$ denotes the transverse momentum of the hadronic final state.

The kinematic variables can be calculated from γ_h and θ_e as follows:

$$Q^2_{DA} = 4E^2_e \frac{\sin \gamma_h (1 - \cos \gamma_h)}{\sin \gamma_h + \sin \theta_e - \sin(\theta_e + \gamma_h)}, \tag{2.6}$$

$$x_{DA} = \frac{E_e}{E_p} \frac{\sin \gamma_h + \sin \theta_e + \sin(\theta_e + \gamma_h)}{\sin \gamma_h + \sin \theta_e - \sin(\theta_e + \gamma_h)}. \tag{2.7}$$

Since it is independent of the energy measurement this method is used for calorimeter calibration. It is used for calibration of the electromagnetic energy scale of the LArCal by determining the energy of the scattered lepton via both angles θ_e and γ_h:

$$E'_e = \frac{2E_e \sin \gamma_h}{\sin \gamma_h + \sin \theta_e - \sin(\gamma_h + \theta_e)}. \tag{2.8}$$

In THE SIGMA METHOD the denominator of y_h in equation 2.1 is replaced by $\sum_i (E_i - p_{z,i})$, where i runs over all final state particles, including the scattered positron. Due to energy and momentum conservation this expression equals $2E_e$. The advantage of this method is that it corrects for initial state radiation. The sum yields the true lepton energy which enters into the ep interaction. Hence, in case that the incident lepton radiates off bremsstrahlung photons which escape detection, the energy of the lepton entering the ep interaction is smaller than E_e. The kinematic variables can be written as

$$y_\Sigma = \frac{\Sigma}{\Sigma + E'_e(1-\cos\theta_e)}, \tag{2.9}$$

$$Q^2_\Sigma = \frac{E'_e \sin^2\theta_e}{1-y_\Sigma}, \tag{2.10}$$

with the sum

$$\Sigma = \sum_{h_i}(E_{h_i} - p_{z,h_i}) \tag{2.11}$$

running over all hadronic final state particles h_i.

The reconstruction methods vary in resolution. The equations for the hadron method that has to be used in the following analysis of CC events, lead to:

$$\frac{\delta Q^2_h}{Q^2_h}|_{y_h} \propto \frac{\delta y_h}{1-y_h}. \tag{2.12}$$

Accordingly, the resolution degrades strongly in Q^2 with increasing y_h. With increasing transverse momentum of the hadronic final state $p_{T,h}$ the Q^2 resolution increases:

$$\frac{\delta Q^2_h}{Q^2_h}|_{p_{T,h}} \propto \frac{\delta p_{T,h}}{p_{T,h}}. \tag{2.13}$$

The y resolution is almost independent of y_h.

The electron method provides a better Q^2 resolution over the entire phase space but the x and y resolution degrade strongly with decreasing y_e according to:

$$\frac{\delta y_e}{y_e}|_{E'_e} = \frac{y_e - 1}{y_e}\frac{\delta E'_e}{E'_e}, \qquad \frac{\delta y_e}{y_e}|_{\theta_e} = \frac{1-y_e}{y_e}\cot\left(\frac{\theta_e}{2}\right)\delta\theta_e. \tag{2.14}$$

2.4 Hadronic Energy Measurement

The accurate reconstruction of the hadronic final state h is crucial for a precise measurement of the CC cross section. In this section the calculation of the hadronic final state four–vector p_h and the calibration of the hadronic LAr calorimeter is discussed.

2.4.1 Reconstruction of the Hadronic Final State

The four–vector p_h of the hadronic final state h is reconstructed using detector information from the LArCal, the SpaCal, the instrumented iron and the central tracking system. For low particle momenta p the energy resolution of the LArCal is worse than the energy resolution of the tracking detectors. Thus, even though most of the energy is measured in the LArCal, tracking information is used to improve the energy measurement for events with low momentum particles. The FSCOMB algorithm [41] provides an optimised reconstruction method and is therefore used in the following analysis. It is based on the track selection package in H1PHAN [39] in which the main requirements for a "good" track are a starting point close to the interaction vertex and a minimum track length. In FSCOMB every "good" low momentum track with $p_{track} < 2\,\text{GeV}$ is extrapolated to the LArCal and a cylinder with radius r = 25 (50) cm in the electromagnetic (hadronic) section is assigned to it. If the energy within this cylinder, E_{LArCal}, exceeds the track momentum p_{track}, E_{LArCal} is used for the reconstruction of the hadronic final state. Otherwise the clusters behind the track are subtracted from the energy sum and the track momentum, p_{track}, is used for the calculation of p_h. For track momenta $p_{track} \geq 2\,\text{GeV}$ only information from the LArCal is used.
In order to minimise effects from calorimeter noise dedicated techniques have been developed that allow rejection of low energy isolated clusters in the calorimeter. Any energy deposit in the LArCal that is not associated with a low momentum track or rejected as noise is taken into account for the measurement of p_h:

$$p_h = (E_h, p_{x,h}, p_{y,h}, p_{z,h}) = p_{LArCal} + p_{SpaCal} + p_{track} - p_{noise} \tag{2.15}$$

The hadronic energy measurement is further improved by including hadronic energy depositions in the SpaCal. For further details on the hadronic energy measurement see [42].

2.4.2 Calibration of the Liquid Argon Calorimeter

Calibration of the hadronic system is based on the fact that in NC events the transverse momenta of the hadronic final state and of the scattered lepton have to be balanced. Hence, it relies on a precisely calibrated positron energy scale achieved by using equation 2.8 and the measured angle of the scattered lepton, θ_e, and that of the hadronic system, γ_h. The comparison of the nominal value for the energy of the scattered lepton with the measured value allows an absolute calibration of the electromagnetic energy scale. For further details see [43] and [44].

The hadronic final state is generally spread over a wide range in the calorimeter which makes the calibration of the hadronic energy scale more sophisticated. The calibration method is outlined in [42]. It is based on the measurement of the ratio of $p_{T,h}$ and $p_{T,e}$, the transverse momentum of the hadronic system and that of the scattered lepton after electromagnetic scale calibration, respectively. The balance in transverse momentum, $p_{T,bal} = p_{T,h}/p_{T,e}$, is expected to be 1 in NC events. In an iterative process the data are adjusted for every wheel of the

LArCal until they are in good agreement with the Monte Carlo simulation (see next section). In contrast to the calibration of the electromagnetic energy scale this provides no absolute but a relative calibration to the Monte Carlo simulation.
Since the response of the LArCal depends on $p_{T,h}$ in a next step a further correction is applied to data and Monte Carlo simulation. It ensures linearity of the energy measurement for the whole event sample.

Figure 2.6 demonstrates the quality of the hadronic calibration for six regions of the LAr calorimeter. In Figure 2.6 (left) the mean value of the ratio $< p_{T,h}/p_{T,e} >$ as a function of $p_{T,e}$ is shown for NC data and Monte Carlo simulation. In figure 2.6 (right) the agreement between data and Monte Carlo simulation is shown as ratio $(< p_{T,h}/p_{T,e} >^{Data})/(< p_{T,h}/p_{T,e} >^{MC})$.

After calibration the hadronic energy measurement for data and Monte Carlo events agree within 2% as can be seen in figure 2.7 where the ratio between $p^{D}_{T,bal}$ measured in data and $p^{MC}_{T,bal}$ measured in Monte Carlo events is shown versus the hadronic angle γ_h. In the two kinematic regions $12 < p_{T,h} < 25\,$GeV and $p_{T,h} > 25\,$GeV good agreement is achieved over the whole angular range. The ratio y_h/y_e as a function of the hadronic angle γ_h is also compared in figure 2.8 and the data are found to be described by the Monte Carlo simulation within 2%.

For the presented analysis the code for the calibration procedure described in [11] was translated into C++.

2.5 Monte Carlo Models

Theoretical predictions of particle interaction processes are modeled in so called MONTE CARLO MODELS. They are used for the comparison between data and theoretical predictions. All processes that contribute to a specific cross section that is measured in an analysis have to be modeled in order to be able to calculate quantities like detector acceptance and number of background events, for instance (see chapter 4). For the CC event selection two main background processes from ep interactions have to be considered, namely background from DIS NC and from photoproduction NC events (see section 3.2). In this analysis two Monte Carlo generators are used to model CC and background events. These are DJANGOH 1.2 [45] for DIS and PYTHIA 5.7 [46] for photoproduction processes.

The Monte Carlo generator models the hard subprocess of ep interactions in three phases. First the elementary scattering process is simulated based on the parton distributions used in the model and the theoretically predicted cross section. In a second step higher order QED and QCD radiation effects are taken into account using phenomenological models. In the last step a phenomenological model takes care of the hadronisation of the partons.

Once the generation process is completed the generated particles are then processed in H1SIM [34], a program based on GEANT [47] to simulate the H1 detector. In the detector simulation the interaction of hadrons and leptons with the detector material and the resulting response of all subdetector electronics are simulated.

In the last step the signals simulated by H1SIM are used for the reconstruction in H1REC [34]. Here, as for data, particle energies and momenta are reconstructed from detector signals.

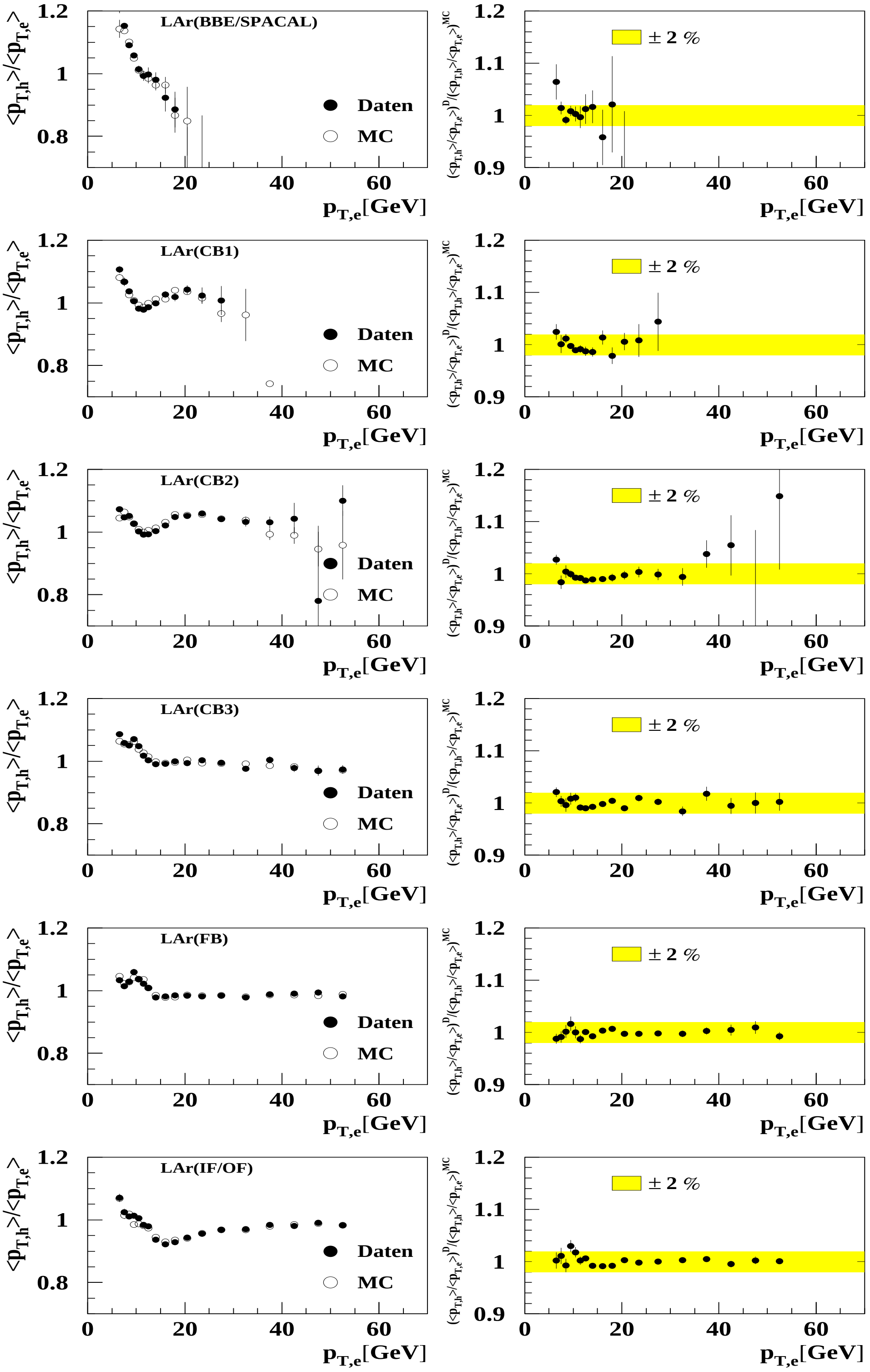

Figure 2.6: *The ratios* $< p_{T,h}/p_{T,e} >$ *(left) and* $(< p_{T,h}/p_{T,e} >^{Data})/(< p_{T,h}/p_{T,e} >^{MC})$ *(right) as a function of* $p_{T,e}$ *for neutral current data (solid points) and Monte Carlo simulation (open points) in six regions of the LAr calorimeter. Taken from [11].*

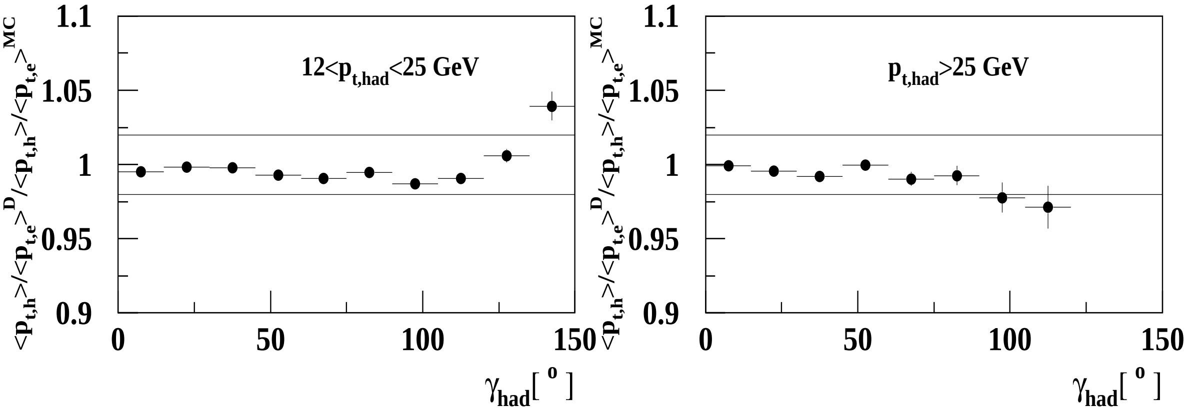

Figure 2.7: *Ratio between $p_{T,bal}^D$ for data ($< P_{T,h} > / < P_{T,e} >^D$) and $p_{T,bal}^{MC}$ for Monte Carlo simulation ($< P_{T,h} > / < P_{T,e} >^{MC}$) versus the hadronic angle γ_h for $12 < p_{T,h} < 25$ GeV (left) and for $p_{T,h} > 25$ GeV (right). The lines indicate a 2% band around a ratio of 1. Taken from [11].*

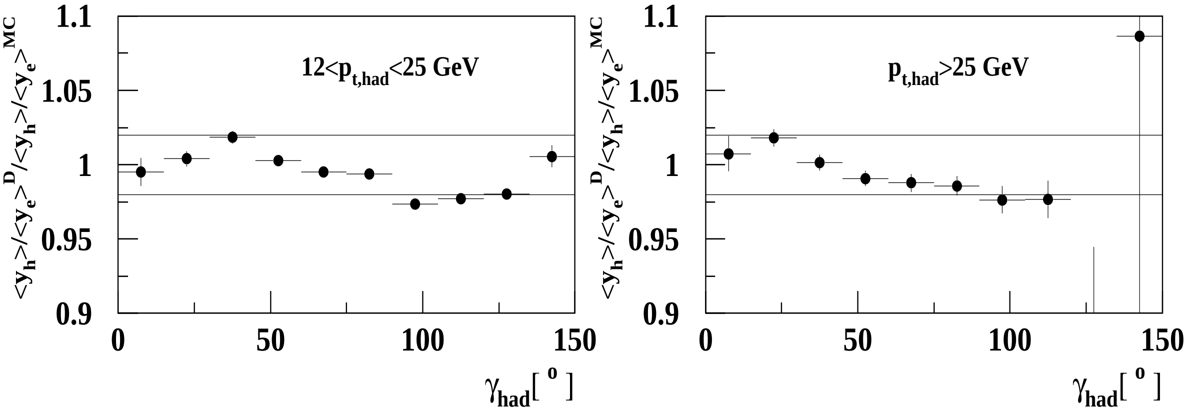

Figure 2.8: *Ratio between $< y_h > / < y_e >^D$ for data and $< y_h > / < y_e >^{MC}$ for Monte Carlo simulation versus the hadronic angle γ_h for $12 < p_{T,h} < 25$ GeV (left) and for $p_{T,h} > 25$ GeV (right). The lines indicate a 2% band around a ratio of 1. Taken from [11].*

CC and NC DIS Events

In this analysis DIS events are generated using DJANGOH 1.02. This generator simulates DIS lepton–proton interactions based on LEPTO [48] including QED and QCD radiative effects by including the HERACLES programme [49]. For the fragmentation of the partons the program JETSET [50] based on the LUND string fragmentation model [51] is implemented. The hard subprocess is generated according to the cross section obtained from CTEQ5L [52] parameterisations for the PDFs. This simulated cross section is then reweighted to the NC and CC cross sections measured previously at H1. The reweighting is done using a NLO QCD fit, H1 PDF 97 [42], to previous data.

Photoproduction Events

Photoproduction events are NC ep interactions with $Q^2 \approx 0\,\mathrm{GeV}^2$ which corresponds to the exchange of a quasi–real photon. In these events the scattering angle θ_e of the outgoing lepton is very small. We distinguish between two types of photoproduction events: DIRECT and RESOLVED photoproduction [53].

In direct processes the photon interacts directly with the quark or gluon coming from the proton. Figures 2.9 (a) and (b) show examples for direct photoproduction processes, namely the Boson–Gluon–Fusion and the QCD–Compton process, respectively. Hadrons produced in these kinds of processes have typically high transverse momenta because the total photon energy enters into the interaction process.

The second class of photoproduction events are the so called resolved processes where the photon fluctuates into a hadronic state before the interaction with a parton from the proton. Thus, a parton from the photon couples to a parton from the proton. A diagram for such a process is depicted in 2.9 (c). In addition to the proton remnant the hadronic remnant of the photon can be measured in the detector. Jets produced in resolved processes have typically smaller transverse momenta than those produced in direct processes.

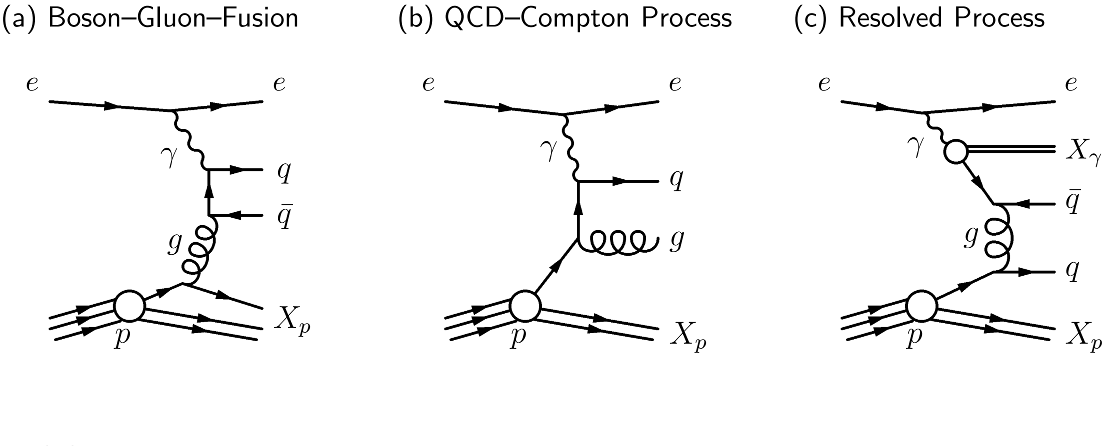

Figure 2.9: *Diagrams for photoproduction processes in leading order α_s. Direct photoproduction (a and b) and resolved photoproduction (c) are shown.*

Photoproduction events are modeled by the PYTHIA 5.7 event generator using GRV LO [54] parton densities for the proton and the photon. PYTHIA is a program for the generation of high-energy physics events based on leading order matrix elements, parton showers and LUND hadronisation.

Direct and resolved processes are considered as well as open heavy flavour production (see figure 2.9 (a)) of $c\bar{c}$ and $b\bar{b}$ and production of prompt photons.

Real $W^{\pm}$ Production Events

Two diagrams as examples for the process $ep \rightarrow \nu_e W^{\pm} X$ are shown in figure 2.10. The cross section for the production of real $W^{\pm}$ bosons at HERA is very small. Nevertheless, these events are considered as possible background since they have the CC event characteristic of missing transverse momentum measured in the detector. Production of real $W^{\pm}$ bosons is modeled by EPVEC [55].

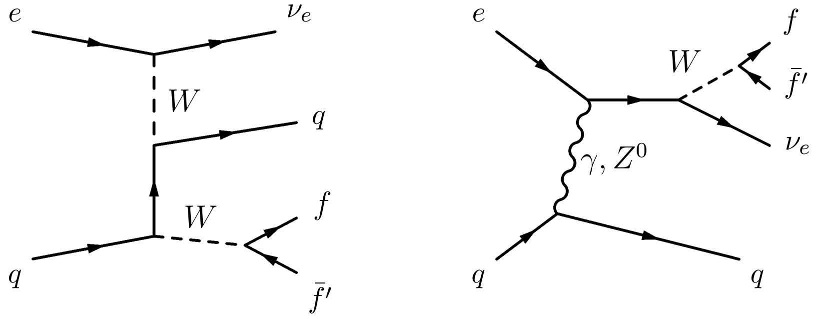

Figure 2.10: *Examples for W production diagrams including a neutrino ν_e in the final state.*

Luminosities

In order to get a statistical uncertainty of the Monte Carlo predictions that is smaller than that of the data over the entire phase space of the measurement the integrated luminosities of the Monte Carlo sets are high compared to the luminosity of the data.

The luminosities of the Monte Carlo samples used for the presented analysis are summarised in table 2.1.

CC DJANGO	
$Q^2 [\text{GeV}^2]$	Luminosity $[\text{pb}^{-1}]$
> 100	5360.49
$> 10,000$	291,279.03

NC DJANGO	
$Q^2 [\text{GeV}^2]$	Luminosity $[\text{pb}^{-1}]$
> 60	49.83
> 100	82.306
> 1000	365.80
$> 10,000$	35,246.62

γp PYTHIA	
Process	Luminosity $[\text{pb}^{-1}]$
direct	550
resolved	100
open $c\bar{c}$	140
open $b\bar{b}$	240
prompt photons	1400

$W^{\pm}$ Production EPVEC
Luminosity $[\text{pb}^{-1}]$
100,069

Table 2.1: *Luminosities of the Monte Carlos samples used in this analysis.*

Chapter 3

Data Selection

The present analysis is based on data from positron-proton collisions recorded with the H1 detector in the years 1999 and 2000. It only considers events in which the required detector components, namely the central trackers, the LArCal and the luminosity system were on high voltage. The analysed data correspond to an integrated luminosity of $\mathcal{L} = 65.25\,\text{pb}^{-1}$.

The charged current event selection used in this analysis is based on the selection used in [9] and [18]. The same method for the reconstruction of the hadronic final state has been used. Significant changes to the cited analyses have been performed.
The first main difference lies in the fact that reprocessed data (DST3) are used for this analysis whereas formerly pre-reprocessed data (DST1) were used. During reprocessing improved knowledge of the detector performance enters into the reconstruction software H1REC, and data as well as Monte Carlo simulations pass through the reconstruction again. In the reprocessing mainly the reconstruction of tracks and the fitting of the vertex changed. Therefore parameters that rely on track measurement are influenced. Since the CC event selection is mainly based on calorimeter information the influence of the reprocessing on the event selection is small as will be discussed in the following.
The second significant change lies in the transfer to the new $\mathrm{H1\ OO}$ analysis framework and with it the implementation of modified non-ep background finders.

In this chapter the selection criteria and selection efficiency studies are presented.

3.1 Selection of Charged Current Events

The fundamental feature of charged current events is an imbalance in transverse momentum measured in the detector. The weakly interacting neutrino escapes detection and causes a missing transverse momentum, $p_{T,miss}$, which is equal to the transverse momentum of the hadronic system, $p_{T,h}$. The selection of charged current events is essentially based on this striking signature.

3.1.1 Trigger Conditions and Efficiencies

The trigger conditions used for this analysis were developed in [11]. Triggering of CC events is based on first level trigger elements that register an imbalance in the LArCal energy deposits, indicating missing transverse momentum. Combined with timing information from the tracking chambers these trigger elements form the subtriggers ST66 and ST77. Supplementary, ST71 was set up in order to improve the trigger efficiency for small values of $p_{T,miss}$ and high values of y_h [43]. For a further improvement on the CC trigger efficiency events triggered by the NC triggers ST67 and ST75 are also accepted.

The definitions of the subtriggers relevant for the present analysis are listed in table 3.1. Table 3.2 contains a description of the trigger elements.

The efficiencies of these CC triggers cannot be determined using CC events due to their low statistics. In Monte Carlo simulation the trigger response is not described correctly such that it also cannot be used for the determination of the trigger efficiencies. Therefore the technique of *Pseudo–CC* data production was introduced [56]. For the production of *Pseudo–CC* events NC events are identified and subsequently all information related to the scattered positron is removed for all subdetectors and all triggers. Under the assumption that the hadronic final state is similar for NC and CC events the *Pseudo–CC* events are indistinguishable from CC events. This has been verified by studies of the hadronic final state in NC and CC interactions [57]. Since for $Q^2 \lessapprox 10,000\,\text{GeV}^2$ the NC cross section is significantly higher than the CC cross section (see section 1.3.2) the statistics of *Pseudo–CC* events exceeds that of CC events. To ensure that the x and Q^2 spectra of CC events are reproduced correctly the *Pseudo–CC* events are reweighted with respect to the CC spectra with the weight:

$$w(x,Q^2) = \frac{d^2\sigma_{CC}/dxdQ^2}{d^2\sigma_{NC}/dxdQ^2}, \tag{3.1}$$

where the CC and NC cross sections, $d^2\sigma_{CC}/dxdQ^2$ and $d^2\sigma_{NC}/dxdQ^2$, are calculated using parton densities from the NLO QCD fit H1 PDF97 [42].

Subtrigger	Definition
ST66	LAr–Etmiss$>4.4\,$GeV $\&\&$ LAr–IF>1 $\&\&$ (Ray–T0 $\|\|$ LAr–T0)
ST77	LAr–Etmiss$>5.2\,$GeV $\&\&$ Ray–T0
ST71	LAr–BigRay$\&\&$DCRPh–Tc $\&\&$ zVtx–sig>1 $\&\&$ DCRPh–T0 $\&\&$ Ray–T0 L2: LAr–BigT–miss
ST75	LAr–electron–2 $\&\&$ DCRPh–THig $\&\&$ Ray–T0
ST67	LAr–electron–1 $\&\&$ (Ray–T0 $\|\|$ LAr–T0)

Table 3.1: *Definition of subtriggers relevant for this analysis. Only the main trigger elements are listed. The symbols && and || denote the logical AND and OR, respectively.*

Trigger Element	Description
LAr–Etmiss	vector sum of transverse energy in LArCal 'trigger towers' exceeds a threshold value
LAr–IF	energy sum in forward LArCal 'trigger towers' exceeds a threshold value
LAr–T0	timing of LArCal signals compatible with nominal bunch crossing
LAr–BigRay	Local coincidence between MWPC 'rays' and calorimeter 'towers'
LAr–electron–1	energy in local region of LArCal (trigger tower) exceeds a threshold value of 6 GeV
LAr–electron–2	energy in local region LArCal (trigger tower) exceeds a threshold value of 7.5 GeV
LAr–BigT–miss	level 2: vector sum of transverse energy in LArCal summed over several 'trigger towers' ('big towers') exceeds threshold value
Ray–T0	at least 1 track candidate in MWPC (ray) indicates a vertex
zVtx–sig	certain number of rays indicate common vertex
DCRPh–T0	at least 1 track candidate with transverse momentum $p_T > 450$ GeV; drift time smaller than time between two consecutive bunch crossings
DCRPh–Tc	at least 3 track candidates with transverse momentum $p_T > 450$ GeV
DCRPh–THig	at least 1 track candidate with transverse momentum $p_T > 800$ GeV

Table 3.2: *Trigger elements of the LArCal and of the central tracking system.*

In figure 3.1 the overall trigger efficiency, ϵ, is shown as a function of the hadronic transverse momentum, $p_{T,miss}$, and the hadronic angle, γ_h. As the trigger efficiency ϵ is not described by the simulation all Monte Carlo events are reweighted to the data in order to allow for a comparison between data and Monte Carlo simulation in the analysis.

At low values of $p_{T,miss}$ and high values of y_h most of the energy of the hadronic final state is measured in the central part of the LArCal. In this region the noise level and hence the local energy thresholds for the triggers are high which leads to the observed inefficiency. For small angles γ_h which corresponds to low values of y_h the hadronic final state is mainly scattered in forward direction where the opening for the beam pipe is situated and triggering of missing energy deposits is experimentally difficult.

Since all subtriggers used for triggering of CC events are based on energy depositions in the calorimeter and do not rely on the track reconstruction the trigger efficiency is not influenced by the reprocessing. It can thus be adopted from [11]. A systematic uncertainty of 4% on the trigger efficiency is quoted.

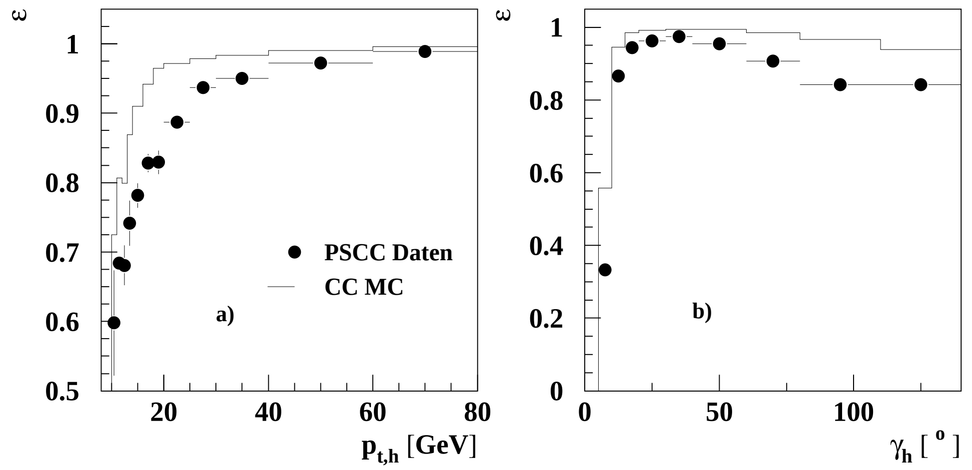

Figure 3.1: *Total trigger efficiency as a function of hadronic transverse momentum, $p_{T,h}$ (left), and hadronic angle, γ_h (right), taken from [11].*

3.1.2 Kinematic Selection Criteria

$p_{T,miss} \geq 12$ GeV:

The CC cross section is steeply falling with increasing $p_{T,miss}$ (see figure 3.6). However, the requirement $p_{T,miss} \geq 12$ GeV is necessary because below this threshold CC events cannot be triggered efficiently, as shown in figure 3.1. In addition, the amount of background events (see section 3.2) increases drastically for low values of $p_{T,miss}$.

$0.03 \leq y_h \leq 0.85$:

At low values of y_h the hadronic final state is scattered in forward direction, corresponding to low values of γ_h. In this region the trigger efficiency is steeply falling, as can be seen in figure 3.1. This is accounted for by the requirement $y_h \geq 0.03$. The upper limit $y_h \leq 0.85$ excludes the y_h region where the Q^2 resolution of the hadron method strongly decreases (see section 2.3).

3.2 Background Rejection

The main background sources in the selection of charged current events can be classified into two categories:

1. Non-ep background induced by muons from cosmic rays or by proton beam halo muons
2. ep induced background from NC or photoproduction events

In this section the methods which are applied in order to efficiently reject these types of background events are discussed.

3.2.1 Non–ep Background

Muons from cosmic rays and from the proton beam halo are the main sources for particles which do not originate from lepton–proton interactions but are measured in the detector and can fake events with missing transverse momentum. Cosmic muons are produced when high–energetic cosmic particles hit the atmosphere of the earth. Halo muons arise from interactions of beam protons with the wall of the beam pipe or with gas molecules in the beam pipe. Figures 3.2 and 3.3 show event topologies of either type of muon induced background events. There are several means available to reject these non–ep background events:

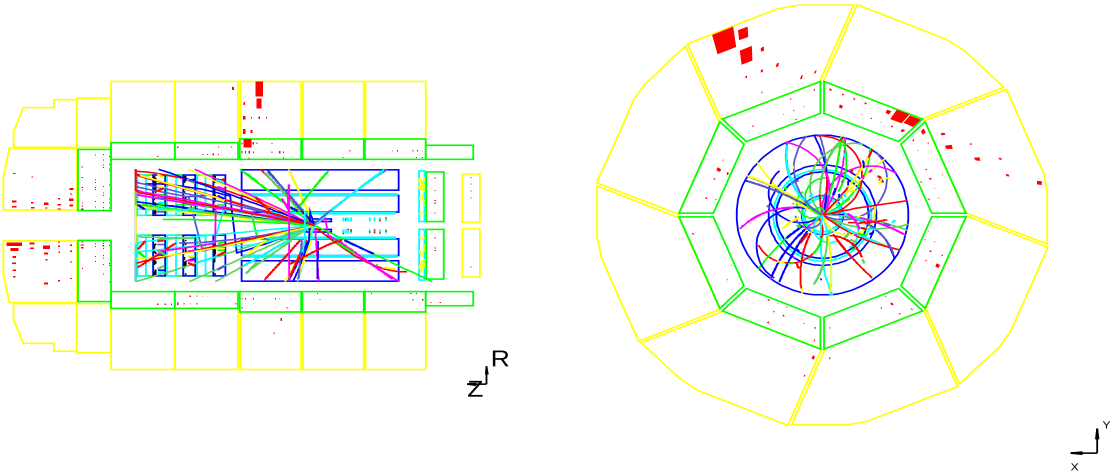

Figure 3.2: *An ep event overlayed by a cosmic muon displayed with the H1 event display. The energy deposited in the LAr calorimeter by a muon crossing the detector can be seen.*

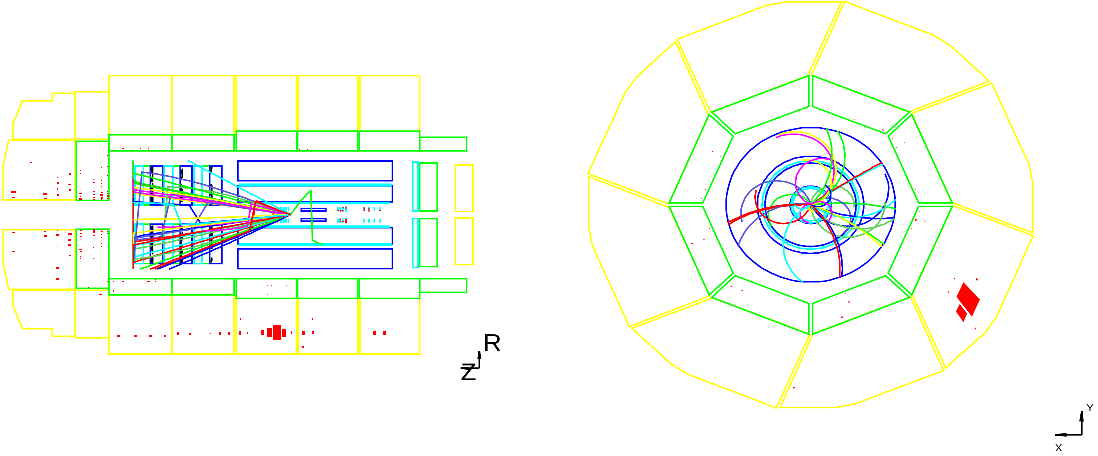

Figure 3.3: *A halo muon event displayed with the H1 event display. The energy deposited in the LAr calorimeter by a muon on its way through the detector parallel to the z–axis can be seen.*

Vertex Requirement

In events originating from ep interactions an event vertex close to the nominal interaction point can be reconstructed. Due to the changing beam conditions the nominal position is not fixed but has a gaussian distribution around an average value. Only data with a reconstructed vertex within ± 35 cm around the nominal position are accepted yielding a cut on the z–vertex position of

$$-32.2\,\text{cm} \leq z_{vertex} \leq 37.8\,\text{cm}. \tag{3.2}$$

In order to get a high efficiency for the vertex reconstruction, information from the central and forward tracking chambers is used. Comparison of the vertex efficiency before and after reprocessing in figure 3.4 shows that it changed slightly.
The position of the reconstructed vertex is constrained by the track reconstruction which changed with the reprocessing. However, for the selected events with $y_h \geq 0.03$ the discrepancy is less than 1% for the Monte Carlo simulations and the efficiency is above 98%.

The difference for the data before and after the reprocessing is assumed to be of the same magnitude since the data and Monte Carlo simulation pass through the same reprocessing algorithms. Therefore, the systematic uncertainty of $2\% - 5\%$ is adopted from [9].
Note that the Monte Carlo simulation used before the reprocessing is based on the cross section obtained from MRSH [58] parameterisations for the PDFs whereas the simulation after the reprocessing is based on the CTEQ5L [52] parameterisations. However, this does not affect the vertex finding efficiency.

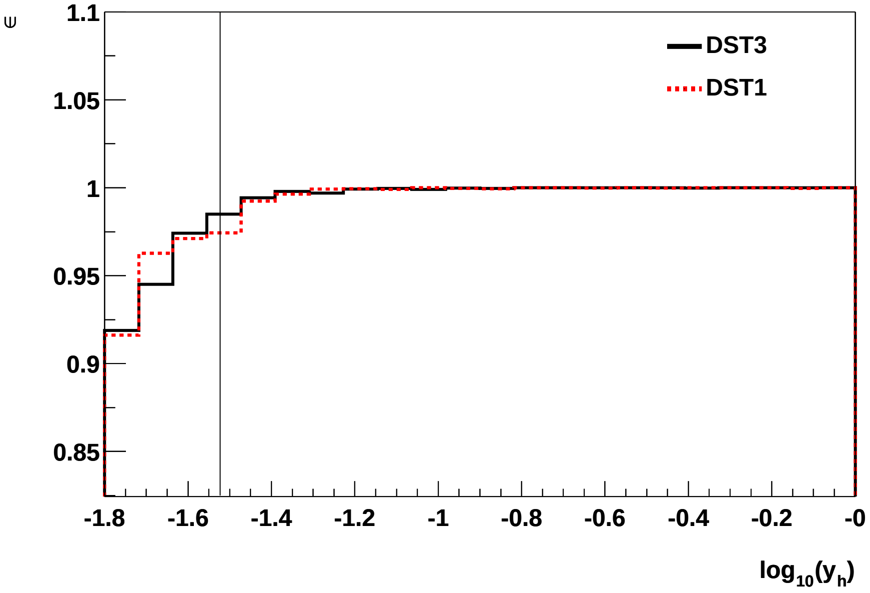

Figure 3.4: *Efficiency ϵ for finding a central or forward vertex in CC events versus y_h. Shown is a comparison between the efficiency after (full line) and before (dashed line) the reprocessing. The line indicates the cut at $y_h \geq 0.03$.*

Background Finders

The clear topology of cosmic ray and beam halo events allowed for the development of dedicated algorithms to identify non–ep background events. In order to reject events that occur outside the timing window of real ep collisions, these so called *non–ep background finders* include requirements on the timing of the tracking chambers and the calorimeter signals. The non–ep background finders fulfill a compromise of being very efficient in rejecting background ($> 99.6\%$) and rejecting as few real CC events as possible ($< 3.5\%$). In a preselected sample of 824,000 events used for this analysis as possible candidates for CC events 660,000 events are identified by the background finders.
A comprehensive overview of the algorithms implemented into the new $\mathrm{H1\ OO}$ framework is given in an internal H1 note [59].

In order to improve the non-ep background rejection several other requirements have to be fulfilled in addition to the background finders implemented into $\mathrm{H1\ OO}$:

- CLUSTER TRACK LINK: If the highest energy cluster is measured in the central region of the LArCal, $\theta > 30°$, it is required to be associated with a track in the central tracker. If no track is found in a cone with radius $R = \sqrt{(\eta_E - \eta_{tr})^2 + (\phi_E - \phi_{tr})^2}$ the event is rejected. The variables η_E and η_{tr} denote the pseudo rapidities of the energy cluster and the track, respectively.

- FORWARD HADRONIC FINAL STATE: The fraction of background is higher for events with a vertex found by the forward tracking chambers than for those events in which the vertex is reconstructed from tracks in the central tracking chambers. Therefore events with a vertex reconstructed in the forward tracking chambers are only accepted if

  - the hadronic final state is reconstructed in forward direction , $\gamma_h \leq 20°$,
    or
  - the LArCal cluster with the highest energy is found in forward direction, $\theta \leq 20°$, and $y_h \leq 0.1$.

- COHERENT NOISE: Calorimeter noise can fake missing transverse momentum. Especially noise from a number of neighbouring cells can produce large values of $p_{T,miss}$. Algorithms have been developed to identify such coherent noise and are implemented into the LArCal monitoring software ARMON [60]. They are used for this analysis to reject runs with a large amount of coherent noise.

The probability, ϵ, to keep real charged current events after applying all non–ep background rejection criteria is shown in figure 3.5. The distribution is shown as a function of y_h for CC Monte Carlo simulation before and after reprocessing. Due to the reprocessing the inefficiency on the CC event selection emerging from topological non–ep background rejection changed less than 1% over the whole y_h range. In particular for $y_h \geq 0.03$ the difference is negligible. In the final measurement of the CC cross section a systematic uncertainty on the CC event losses due to non–ep background finders of 3% is adopted from [11].

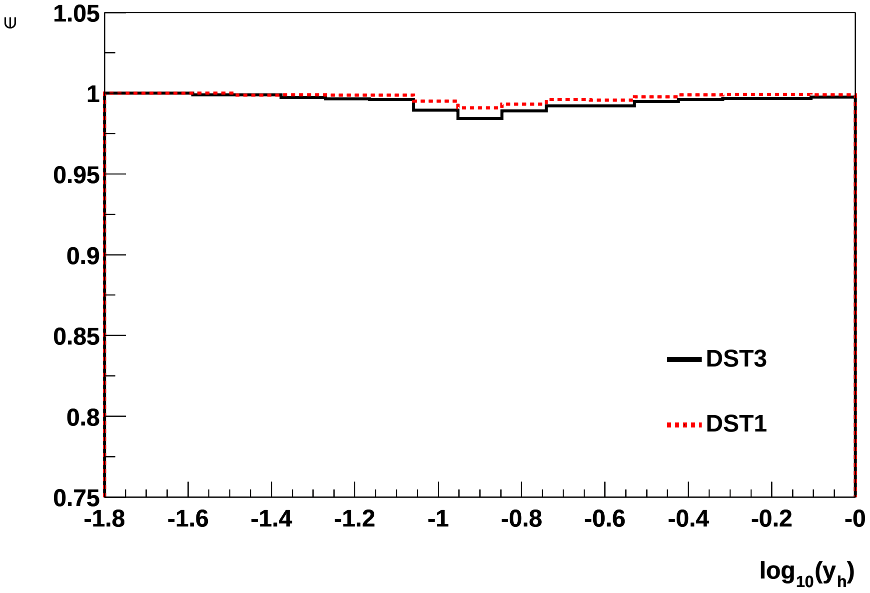

Figure 3.5: *Probability ϵ of all non-ep background finders to keep CC events in dependence of y_h. Shown is a comparison between ϵ after (full line) and before (dashed line) the reprocessing.*

3.2.2 *ep* Induced Background

The finite resolution and limited geometrical acceptance of the detector can lead to a mismeasurement of energy. In this case NC events can appear to be measured with missing transverse momentum and therefore fake CC events. Several means are available to reduce the background induced by genuine ep interactions. The NC events contributing dominantly are divided into two classes:

- **DIS NC:** High Q^2 NC events with a large scattering angle of the positron such that it can be detected in the SpaCal or the LArCal.
- **Photoproduction:** Low Q^2 events where the exchanged boson is a quasi–real photon γ, also called γp events. In these events the scattered positron leaves the H1 detector in $-z$ direction through the beam pipe.

As shown in figure 3.6 for $p_{T,miss} \geq 12\,\text{GeV}$ and $0.03 \leq y_h \leq 0.85$ background from DIS NC and γp events is accumulated at low values of $p_{T,miss}$.

The following criteria to reject NC background events are applied:

No Scattered Positron:

Only those events in which no signals of a scattered positron are measured in the electromagnetic part of the calorimeters are considered. When the positron is scattered into a region of

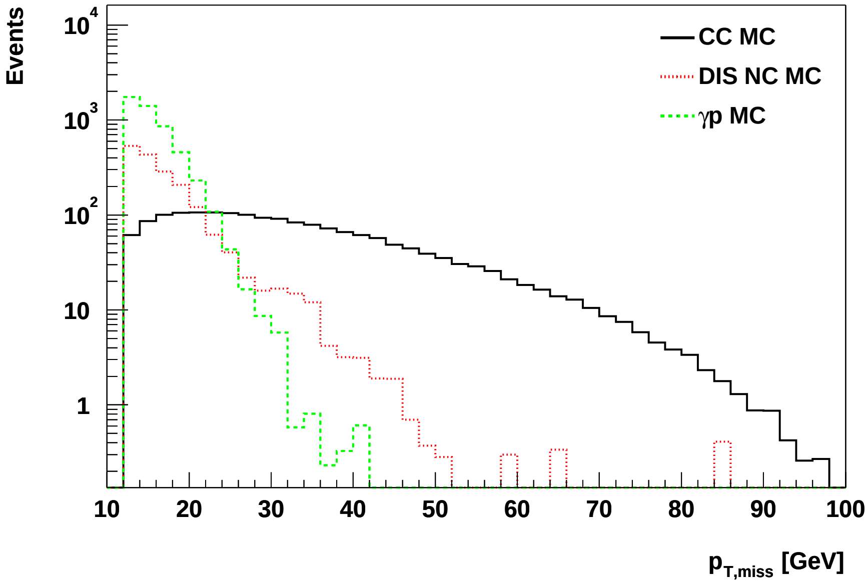

$p_{T,miss} \geq 12$ GeV

$0.03 \leq y_h \leq 0.85$

Figure 3.6: *Distribution of* $p_{T,miss}$ *for CC (full line), DIS NC (dotted line) and* γp *(dashed line) Monte Carlo events after the kinematic cuts for* $p_{T,miss} \geq 12$ *GeV and* $0.03 \leq y_h \leq 0.85$. *The number of events corresponds to the data luminosity of* 65.25 *pb*$^{-1}$.

the detector where the energy measurement is poor, DIS NC events have the same topology as CC events. In the LArCal these regions are situated between the separate calorimeter wheels (*z–cracks*) and the opening of each wheel in ϕ (ϕ*–cracks*), see section 2.1. Events with an isolated track opposite to the hadronic final state pointing in direction of such a crack are rejected.

Acoplanarity V:

The energy flow in the transverse plane is more isotropic for both types of NC events than for CC events. This can be quantified by the introduction of the ACOPLANARITY, V, of an event [42]. It is defined as the ratio of the transverse energy flow antiparallel and parallel to the direction of the transverse momentum of the event:

$$V \equiv \frac{V_{ap}}{V_p}, \tag{3.3}$$

with

$$V_{ap} \equiv -\sum_i \frac{\vec{p}_{t,i} \cdot \vec{p}_{T,h}}{p_{T,miss}} \quad \text{for} \quad \vec{p}_{t,i} \cdot \vec{p}_{T,h} < 0 \tag{3.4}$$

and

$$V_p \equiv \sum_i \frac{\vec{p}_{t,i} \cdot \vec{p}_{T,h}}{p_{T,miss}} \quad \text{for} \quad \vec{p}_{t,i} \cdot \vec{p}_{T,h} > 0, \tag{3.5}$$

where $\vec{p}_{T,h} = \sum_i \vec{p}_{t,i}$ is the summation over all particles in the detector. The V distribution for CC, DIS NC and photoproduction Monte Carlo events with $p_{T,miss} \geq 12$ GeV and $0.03 \leq y_h \leq 0.85$ is shown in figure 3.7. At low values of V the number of CC events exceeds the number of background events from NC processes whereas for higher values of the acoplanarity the expectation for CC events vanishes. By requiring $V \leq 0.15$ the background can be suppressed significantly [18].

$\Delta\phi_{h,PLUG}$:

For a further improvement on the NC rejection a new variable $\Delta\phi_{h,PLUG}$ was introduced in [12]:

$$\Delta\phi_{h,PLUG} \equiv |\phi_{miss} - \phi_{h,PLUG}|, \tag{3.6}$$

where ϕ_{miss} and $\phi_{h,PLUG}$ are the azimuthal angles of the direction of the missing momentum $\vec{p}_{T,miss}$ and of the hadronic final state vector sum measured in the PLUG, respectively. Note that $\phi_{miss} = 180° - \phi_{h,LArCal}$ is the azimuthal angle of the missing transverse momentum $\vec{p}_{T,miss}$ measured in the LArCal. A major part of the γp background arises from events that contain a jet at small polar angles in forward direction such that not all of the energy is recorded in the LArCal, resulting in a measured imbalance in transverse momentum. However, this missing momentum is generally measured in the PLUG calorimeter with such events having values of $\Delta\phi_{h,PLUG}$ close to $0°$. A smaller fraction of DIS NC events has the same topology of a very forward jet and thus is like γp events distributed at small angles of $\Delta\phi_{h,PLUG}$ whereas for CC events the distribution of $\Delta\phi_{h,PLUG}$ is rather flat as shown in figure 3.8.

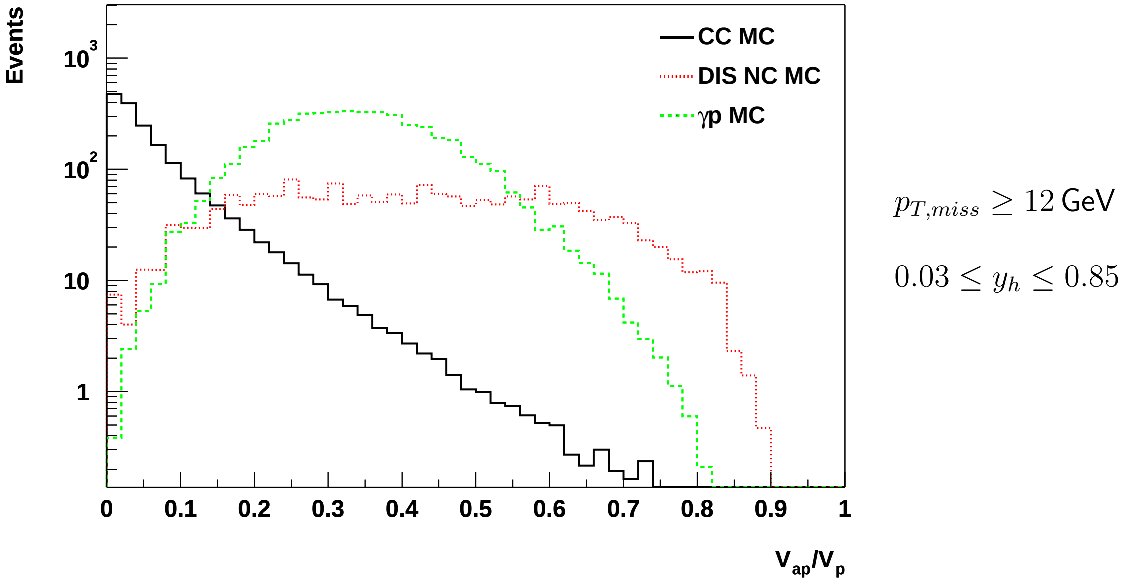

Figure 3.7: *Distribution of the acoplanarity, V, for CC events (full line), DIS NC background (dotted line) and photoproduction background (dashed line). The numbers of events correspond to the data luminosity of 65.25 pb^{-1}.*

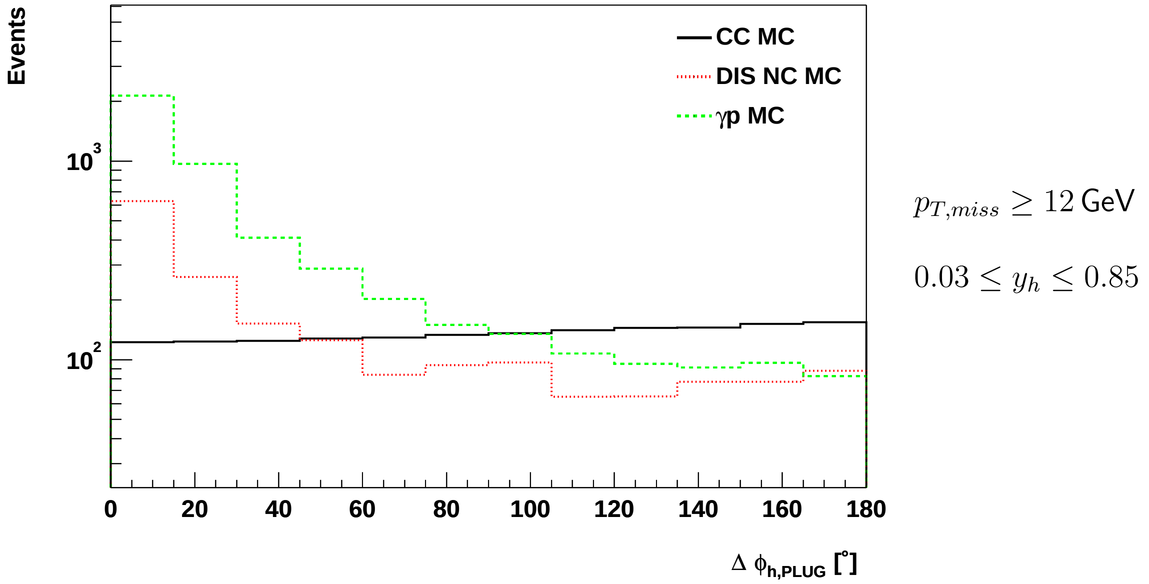

Figure 3.8: *Distribution of $\Delta\phi_{h,PLUG}$ for CC events (full line), NC background (dotted line) and photoproduction background (dashed line) for $12 \leq p_{T,miss} < 25$ GeV.*

Hence, both variables V and $\Delta\phi_{h,PLUG}$ can be employed to separate CC events from NC background. Rather than cutting on them separately they are combined in a $p_{T,miss}$ dependent variable, Δ_{3dim}.

Δ_{3dim}:

For an optimised efficiency of background reduction a $p_{T,miss}$ dependent variable in the ($\Delta\phi_{h,PLUG}$–V) plane is used in the range $12 \leq p_{T,miss} < 25$ GeV [12]:

$$\Delta_{3dim} \equiv \Delta\phi_{h,PLUG} - \left[90 - \frac{180-90}{V_{p_{T,miss}} - 0.2}(V - 0.2)\right], \tag{3.7}$$

with

$$V_{p_{T,miss}} \equiv 0.2\left(\frac{p_{T,miss} - 12}{25 - 12}\right)^2. \tag{3.8}$$

The distribution of Δ_{3dim} for CC events, DIS NC and γp background is shown in figure 3.9 for all events with $p_{T,miss} < 25$ GeV. A cut $\Delta_{3dim} \leq 0$ efficiently separates CC from background events.

In figure 3.10 the distribution of Δ_{3dim} versus V is shown for CC, DIS NC and γp Monte Carlo events. The cut $\Delta_{3dim} \leq 0$ provides an efficient suppression of γp background events for $V \leq 0.2$. It allows an extension of the V cut from 0.15 to 0.2 for $p_{T,miss} \geq 12$ GeV and thus results in a higher efficiency for the selection of CC events, especially for $p_{T,miss} > 25$ GeV.

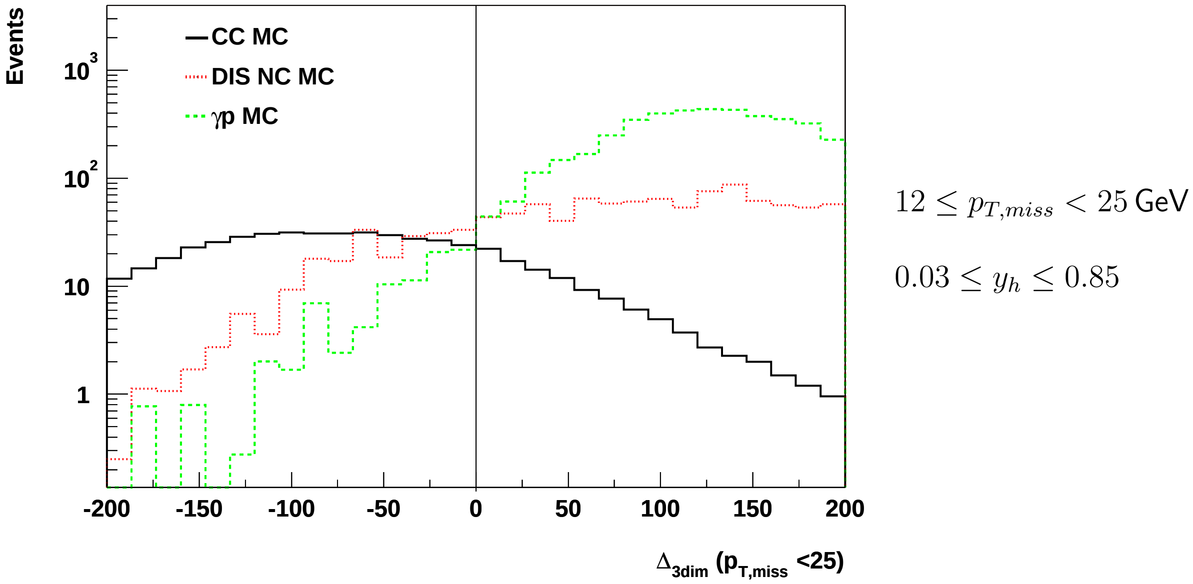

Figure 3.9: *Distribution of* Δ_{3dim} *for CC events (full line), NC background (dotted line) and photoproduction background (dashed line) for* $p_{T,miss} < 25$ *GeV. The vertical line at* $\Delta_{3dim} = 0$ *indicates the cut.*

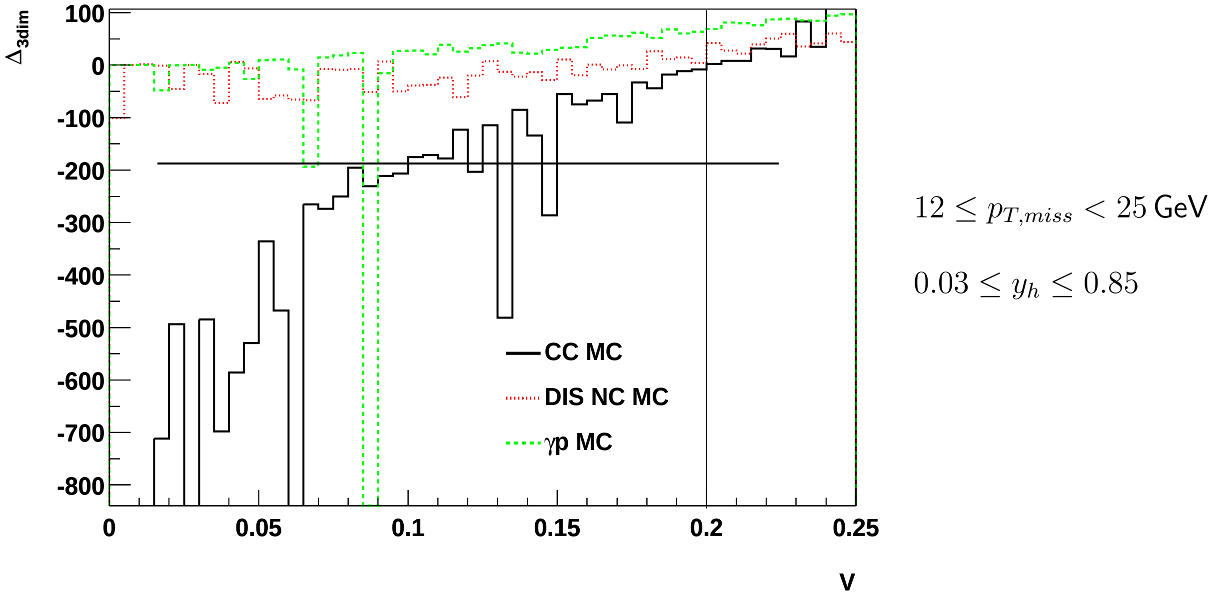

Figure 3.10: *Distribution of* Δ_{3dim} *as a function of the acoplanarity,* V*, for CC events (full line), NC background (dotted line) and photoproduction background (dashed line). The horizontal line indicates the cut* $\Delta_{3dim} \le 0$ *for events with* 12 *GeV* $\le p_{T,miss} < 25$ *GeV and the vertical line indicates the cut* $V \le 0.2$.

3.2.3 Visual Scanning

After all cuts against non–ep and ep induced background (see section 3.2.2) the remaining 1657 events are scanned visually. 141 events are identified by eye as cosmic ray or halo muon events and excluded from the sample. The majority of the events not being rejected by the background finders consists of cosmic events that overlay with a genuine ep interaction.
Only non–ep background events are rejected by visual scanning since remaining ep–background is modeled by the Monte Carlo simulations.

3.2.4 Final Event Sample

As a summary all selection criteria are listed in the following:

- Subtriggers 66, 67, 71, 75 and 77
- $p_{T,miss} \geq 12\,\text{GeV}$
- $0.03 \leq y_h \leq 0.85$
- $-32.2\,\text{cm} \leq z_{vertex} \leq 37.8\,\text{cm}$
- All available non–ep background finders except for bits IBGAM three and four of the QBGFMAR finder (see [59]).
- Cuts against events with a scattered positron
- $\Delta_{3dim} \leq 0$ for $p_{T,miss} \leq 25\,\text{GeV}$, $V \leq 0.2$
- Visual scanning

After application of all selection criteria the final sample includes 1516 events.

Figure 3.11 shows the distributions of $p_{T,miss}$ and $E_h - p_{z,h}$ for all selected events compared to the Monte Carlo expectation from CC and background events. Both distributions are well described by the models.
Note that the trend of the data to overshoot the Monte Carlo expectation in the region $15 < E - P_z < 30\,\text{GeV}$ has been observed already in other analyses [9]. The same is valid for low values of $p_{T,miss}$ and the bin at $p_{T,miss} = 40\,\text{GeV}$. None of these bins shows a significant discrepancy between data and simulation.

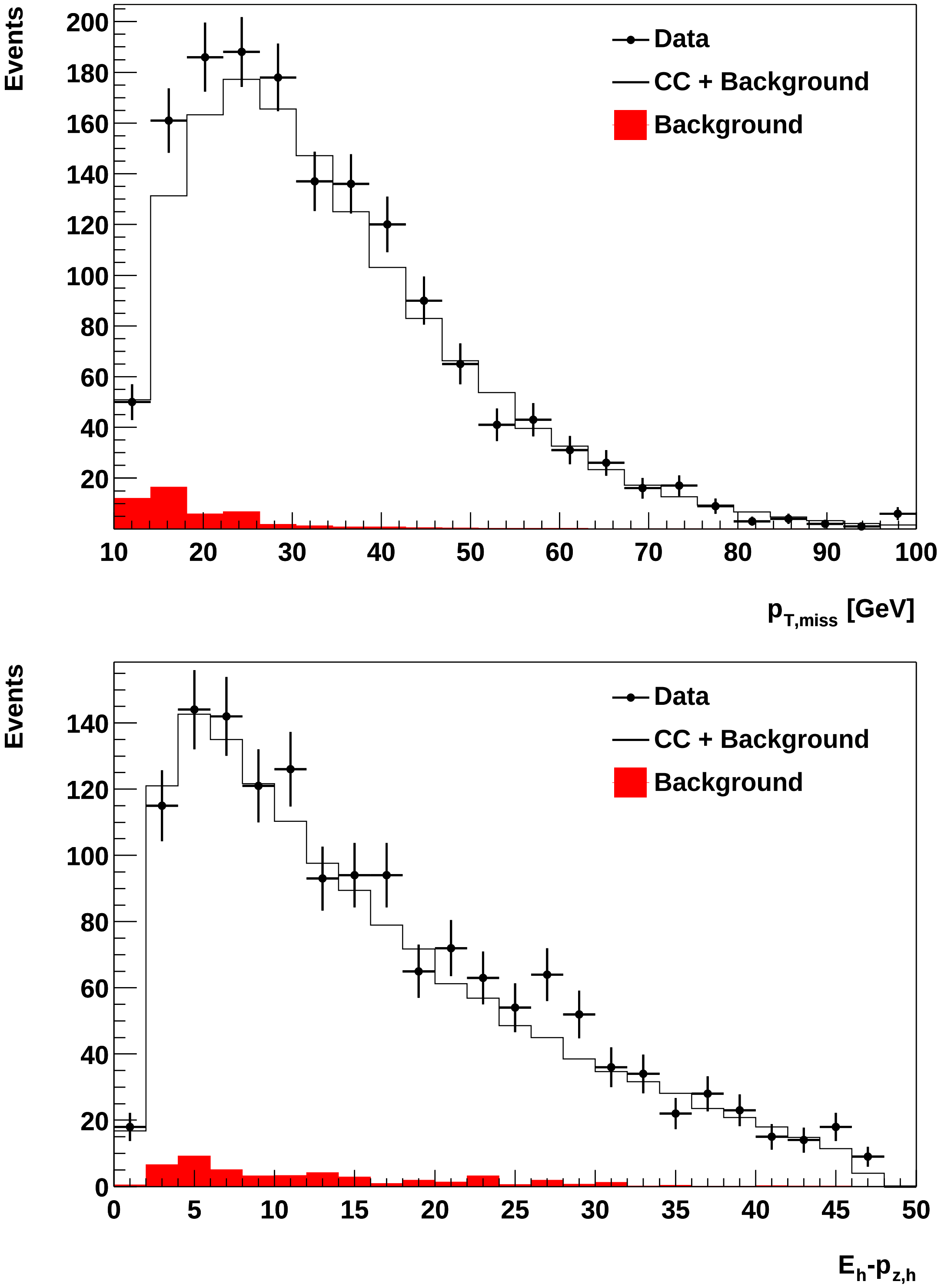

Figure 3.11: *Distribution of* $p_{T,miss}$ *(top) and* $E_h - P_{z,h}$ *(bottom) for the selected CC sample. The data points are compared to the simulation of signal and background events (open histogram). The simulated background is shown as filled histogram.*

Chapter 4

Extraction of the Charged Current Cross Section

The procedure for the extraction of the CC double differential cross section is presented in this chapter. First the kinematic plane is divided into bins of x and Q^2. For each bin the number of events combined with values for detector acceptance, efficiency and radiative correction terms is converted into a cross section value. The systematic uncertainties are quoted and discussed. Finally the procedure for the extraction of the single differential and total CC cross sections is described.

4.1 Extraction of the Double Differential Cross Section

4.1.1 The Binning

The CC cross section measurement is performed in bins of x and Q^2. The same binning as in the latest H1 publication on the CC cross section [9] is chosen for this analysis in order to allow for a comparison of the results. This corresponds to eight bins in x and nine bins in Q^2 with three bins per order of magnitude in x and Q^2. Thus, the two dimensional bin grid includes 72 bins in total with the following bin boundaries and bin centres :

Bin boundaries:

$\log_{10}(x)$	-2.33	-2	-1.67	-1.33	-1	-0.75	-0.5	-0.25	0	
x	0.005	0.010	0.021	0.047	0.100	0.178	0.316	0.562	1.000	

$\log_{10}(Q^2/\,\text{GeV}^2)$	2.35	2.6	2.85	3.1	3.35	3.6	3.85	4.1	4.4	4.7
$Q^2[10^2\ \text{GeV}^2]$	2.2	4.0	7.1	12.6	22.4	39.8	70.8	125.9	251.2	501.2

Bin centres:

$\log_{10}(x)$	-2.10	-1.89	-1.49	-1.10	-0.89	-0.60	-0.40	0.19	
x	0.008	0.013	0.032	0.080	0.130	0.250	0.400	0.650	

$\log_{10}(Q^2/\,\text{GeV}^2)$	2.48	2.70	3.00	3.30	3.70	3.90	4.18	4.48	
$Q^2[10^2\,\text{GeV}^2]$	3	5	10	20	30	50	80	150	300

The bin boundaries are predefined by the selection of $p_{T,miss} > 12$ GeV and $0.03 < y_{had} < 0.85$ which limits the accessible kinematic range. Furthermore the choice of the bin boundaries was influenced by requirements on acceptance ($\mathcal{A}$), purity ($\mathcal{P}$) and stability ($\mathcal{S}$) in each bin i which are defined as follows:

$$\mathcal{A}_i = \frac{N_i^{rec}}{N_i^{gen}} \tag{4.1}$$

$$\mathcal{P}_i = \frac{N_i^{gen,rec}}{N_i^{rec}} \tag{4.2}$$

$$\mathcal{S}_i = \frac{N_i^{gen,rec}}{N_i^{gen,sel}} \tag{4.3}$$

with

- $N_i^{gen,rec}$ being the number of Monte Carlo events generated and reconstructed in bin i,
- N_i^{gen} being the number of Monte Carlo events generated in bin i,
- N_i^{rec} being the number of Monte Carlo events reconstructed in bin i and
- $N_i^{gen,sel}$ being the number of Monte Carlo events generated in bin i that fulfill all selection requirements.

The three quality criteria are entirely determined from simulated CC events. Since the selected data are described well by the Monte Carlo simulation as shown in chapter 3 this procedure is justified. In figure 4.1 acceptance, purity and stability are shown for all bins where the value for the respective quality criterion is non-zero. Low values of x correspond to high y values where the resolution of the hadron method is low. Thus, also the purity in the corresponding bins is low. In events with high x values the hadronic final state goes into forward direction. Here the detector acceptance degrades due to the opening for the beam pipe and thus the reconstruction of the hadronic final state becomes poor.

For the cross section measurement only bins with purity and stability above 30% are taken into account. For the acceptance a minimum of 20% is required. The measurement bins in the kinematic plane of x and Q^2 are shown in figure 4.2. The number of events found in each bin are given, also for those bins which do not fulfill the quality criteria. Note that all

28 bins accepted in [9] are also accepted in this analysis. Additionally, the bin centreed at $\log_{10}(x) = -0.19$ and $Q^2 = 15,000$ fulfills the quality criteria and thus 29 bins enter into the measurement. The numbers of selected events in these bins is 1462 compared to 1497 entering into the 28 bins in the publication. Both measurements have 1317 events in common. It has been verified that those events which only pass the selection criteria of one of the analyses mainly migrate into the other because of the differences in the track and vertex reconstruction after the reprocessing as discussed in chapter 3. About 2% of the selected events migrate due to the changes in the non ep background finders. Migrations between the bins in x and Q^2 are also observed. The numbers of events entering each bin in x and Q^2 are listed in tables A.4 to A.5 for both measurements.

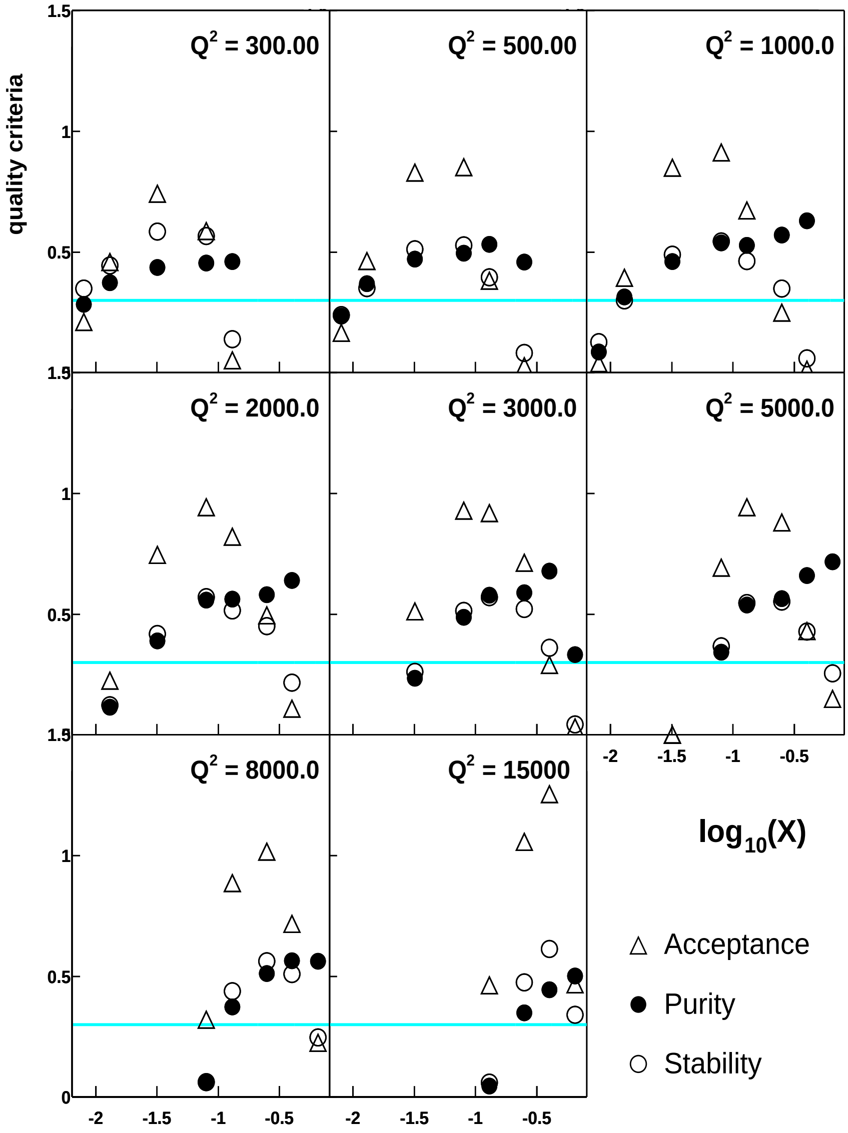

Figure 4.1: *Acceptance, purity and stability for all bins where the value is non-zero. The line indicates the cut value for purity and stability at 0.3.*

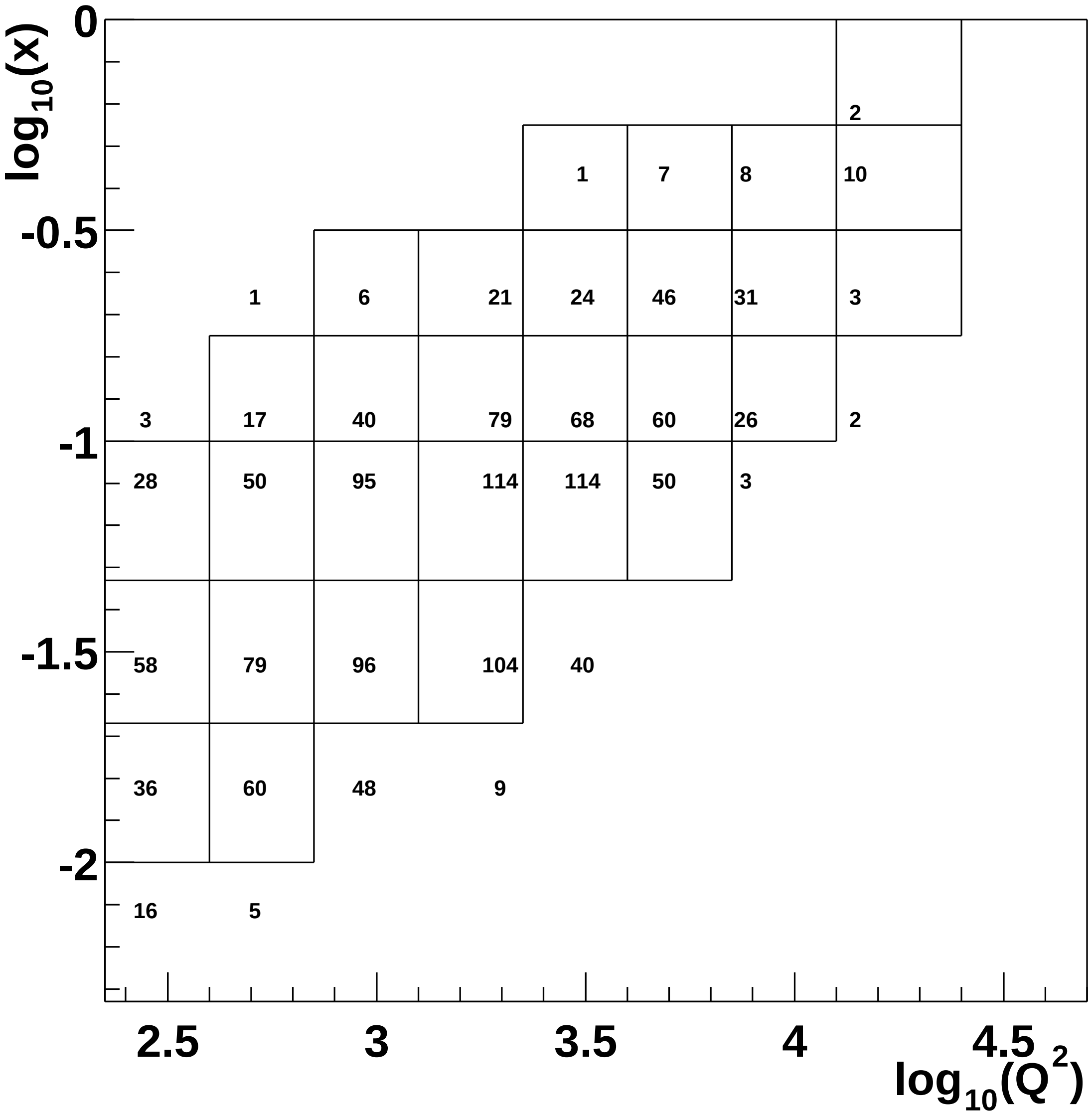

Figure 4.2: *The measurement bins in the kinematic plane of x and Q^2. The number of events found in each bin is plotted at the bin centre. For all those bins which enter into the measurement the bin boundaries are shown. The number of events for the bins which do not fulfill the quality criteria is shown without bin boundaries. A comparison of these number with the numbers in [9] is given in table A.4.*

4.1.2 Determination of the Double Differential Cross Section

For the calculation of the cross section the following notations are used:

- i: Bin number, $i = 1...72$
- N_i^{data}: Number of selected data events in bin i
- N_i^{bg}: Number of background events in bin i determined from Monte Carlo simulation

- $\mathcal{L}^{data}$: Integrated luminosity of the analysed data set
- $\mathcal{L}^{MC}$: Integrated luminosity of the CC Monte Carlo sample
- δ_i^{BC}: Bin centre correction factor. It accounts for the correction due to a projection of the cross section measured in a bin of size $\Delta x_i = x_{i,max} - x_{i,min}$ and $\Delta Q_i^2 = Q_{i,max}^2 - Q_{i,min}^2$ to the bin centre position (x_i, Q_i^2).

  $$\delta_i^{BC} = \frac{\frac{d^2\sigma}{dxdQ^2}\big|_{x=x_i,Q^2=Q_i^2}}{\int\limits_{x_{i,min}}^{x_{i,max}} \int\limits_{Q_{i,min}^2}^{Q_{i,max}^2} \frac{d^2\sigma}{dxdQ^2} dxdQ^2} \equiv \frac{\sigma_i^{theo}}{\hat{\sigma}_i^{theo}} = \frac{\sigma_i^{theo} \cdot \mathcal{L}^{MC}}{N_i^{gen}} \tag{4.4}$$

  The bin centre correction is determined from the theoretical prediction of the double differential cross section at the bin centre position, σ_i^{theo}, and the integrated cross section over bin i, $\hat{\sigma}_i^{theo}$.

- δ^{RC}: Radiative correction factor:

  $$\delta_i^{RC} \equiv \frac{\sigma_i^{theo}}{\sigma_i^{nonrad}} - 1 \tag{4.5}$$

  The radiative correction is estimated by the DJANGOH Monte Carlo simulation, where σ_i^{theo} is the predicted cross section with radiative effects and σ_i^{nonrad} without. In this measurement QED radiative effects from leptonic corrections of $\mathcal{O}(\alpha)$ are included.

The double differential cross section at the centre value of x and Q^2 in bin i is given by:

$$\frac{d^2\sigma}{dxdQ^2}(x_i, Q_i^2) = \frac{N_i^{data} - N_i^{bg}}{\mathcal{L}^{data} \cdot \mathcal{A}_i} \cdot \delta_i^{BC} \cdot \frac{1}{1 + \delta_i^{RC}}. \tag{4.6}$$

Since acceptance $\mathcal{A}_i$, bin centre and radiative corrections are determined using the DJANGOH simulation in which QED radiative corrections are implemented (see section 2.5), equation 4.6 can be simplified using equations 4.1, 4.4 and 4.5:

$$\frac{d^2\sigma}{dxdQ^2}(x_i, Q_i^2) = \frac{N_i^{data} - N_i^{bg}}{N_i^{rec}} \cdot \frac{\mathcal{L}^{MC}}{\mathcal{L}^{data}} \cdot \sigma_i^{nonrad} \tag{4.7}$$

σ_i^{nonrad} is the non-radiative cross section and is taken from the H1+BCDMS PDF 2000 fit [9] to H1 data combined with data from BCDMS.

4.2 Single Differential Cross Sections

The single differential cross sections in x and Q^2 are defined as:

$$\frac{d\sigma}{dx} = \int\limits_{x_{min}}^{x_{max}} \frac{d^2\sigma}{dxdQ^2} dx \qquad \frac{d\sigma}{dQ^2} = \int\limits_{Q_{min}^2}^{Q_{max}^2} \frac{d^2\sigma}{dxdQ^2} dQ^2. \tag{4.8}$$

They can be determined using equation 4.7. The limits for x and Q^2 are chosen to be the lowest and the highest bin edge in x and Q^2.

We define the experimentally measured total CC cross section as

$$\sigma_{tot}^{CC} = \int\limits_{x_{min}}^{x_{max}} \int\limits_{Q^2_{min}}^{Q^2_{max}} \frac{d^2\sigma}{dxdQ^2} dxdQ^2. \tag{4.9}$$

4.3 Systematic Uncertainties

Next to the statistical uncertainty, which is determined by the number of selected events, systematic uncertainties in the measurement procedure (e.g. calibration) and the apparatus (e.g. detector acceptance) contribute to the error[1].

The systematic uncertainties are split into uncorrelated and bin–to–bin correlated uncertainties. Local fluctuations in the measurement conditions cause uncorrelated uncertainties. They can be different for every measurement bin. An example for such an uncorrelated uncertainty is the uncertainty on the vertex reconstruction efficiency which varies with y_h as discussed in section 3.2.1. Correlated uncertainties are systematic shifts which influence the related quantities in every measurement bin in the same way, i.e. shift the measurement in the same direction for each bin. Such an uncertainty evolves, for instance, from a constant difference between the true amount of hadronic energy deposits and the measured hadronic energy deposits in the LArCal.

Uncorrelated and correlated uncertainties are added in quadrature in order to calculate the total systematic uncertainty. The total error is formed by adding the total systematic and the statistical uncertainties in quadrature. All uncertainties on the CC cross section measurements are presented in tables A.1 to A.3.

The systematic uncertainties on trigger efficiency, vertex reconstruction efficiency and non-ep background finding efficiency can be adopted from [11] as discussed in sections 3.1.1 and 3.2. The uncertainty on the hadronic energy scale of the LArCal is composed of an uncorrelated part of 1.7% and a correlated part of 1% arising from the calibration method and the uncertainty on the electromagnetic reference scale [9]. The radiative corrections on the CC cross section are studied in [61]. They are determined with the Monte Carlo generator DJANGOH and compared to results from analytical calculations. Within a systematic uncertainty of 3% good agreement is observed. Uncorrelated and correlated uncertainties are listed below:

---

[1] The active role of the experimentalist is also a source of systematic uncertainties which is usually very difficult to disentangle. This uncertainty includes imperfect programming algorithms, for example.

Uncorrelated uncertainties:

- 3% uncertainty on the efficiency of the non–ep background finders.
- 4% uncertainty on the CC trigger efficiency.
- 3% uncertainty on the CC cross section due to the radiative corrections.
- 2% uncertainty due to the efficiency of the vertex reconstruction increasing to 5% for $y \leq 0.1$.

Correlated uncertainties [9]:

- 25% uncertainty on the energy attributed to noise in the LArCal yielding an uncertainty on the cross section of $< 1\%$.
- $\leq 5\%$ uncertainty on the cross section due to the cut on V_{ap}/V_p.
- 30% uncertainty on the subtracted photoproduction background resulting in an uncertainty on the cross section of $\approx 1\%$.
- 1.5% global uncertainty on the luminosity measurement.

Overall the statistical uncertainty of $\approx 24.5\%$ in average dominates over the systematic uncertainty of $\approx 9.7\%$ as shown in figure 4.3.

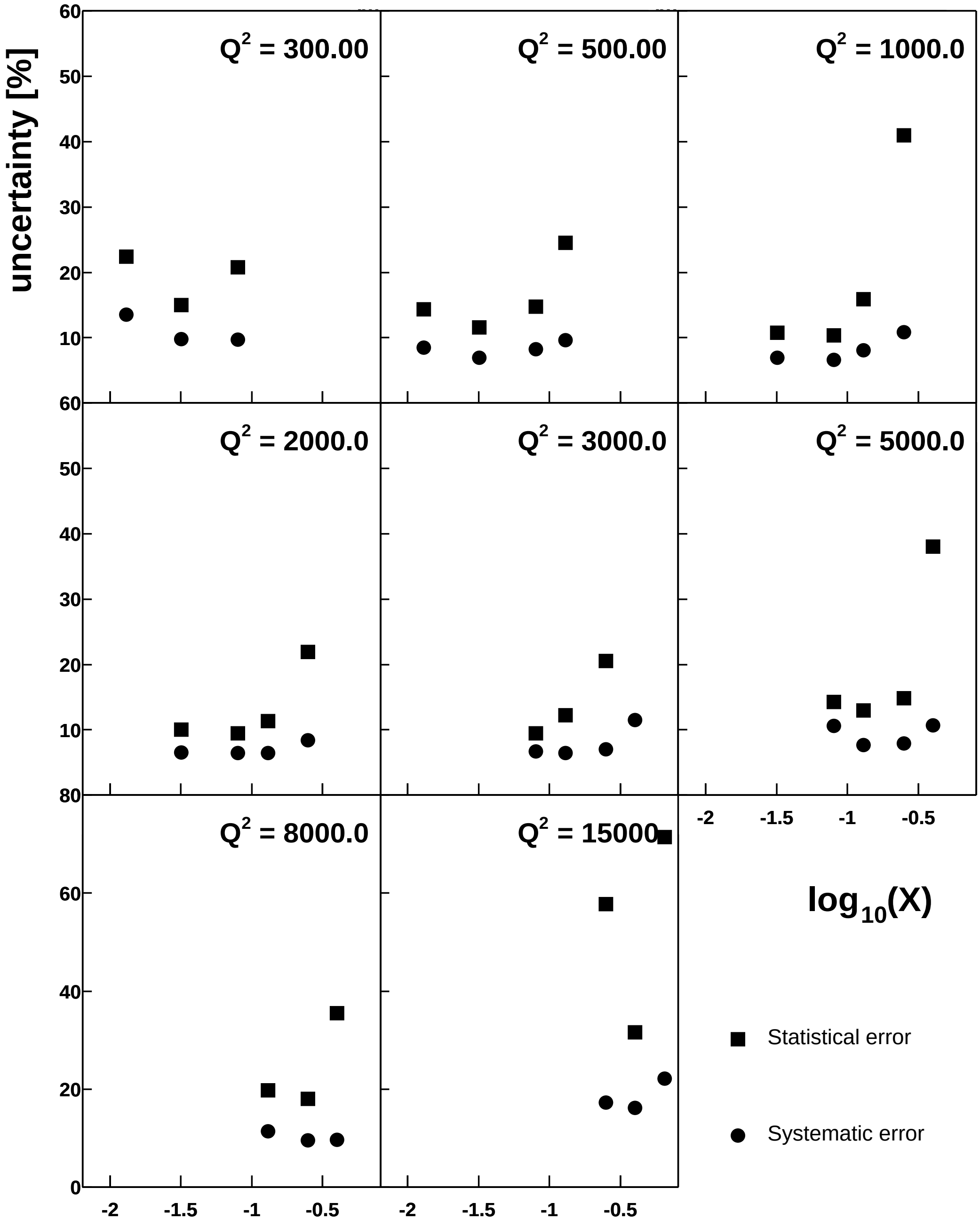

Figure 4.3: *Statistical (squares) and systematic (circles) uncertainties for the CC cross section measurement in bins of x and Q^2.*

Chapter 5

Results

The results of the analysis are presented in this chapter. The CC cross section is measured double differentially in x and Q^2 and single differentially in both of these variables. Finally the measured value for the total CC cross section is presented.

For all measurements the data are compared to the Standard Model prediction. For the theoretical prediction the parton density functions from the latest H1 NLO QCD fit to H1 and fixed target experiment data from BCDMS [2] based on DGLAP evolution equations are used. This H1 PDF+BCDMS 2000 fit and the latest H1 measurement of the CC cross section are presented in [9]. All results of this analysis are compared to the measurements presented in that publication.

5.1 The Double Differential Cross Section

The double differential CC cross section ϕ_{CC} is measured for e^+p interactions at a centre–of–mass energy of $\sqrt{s} = 320\,\text{GeV}$. The bin centres of the measurement are chosen to lie in the kinematic region of $0.013 \leq x \leq 0.65$ and $300 \leq Q^2 \leq 15,000\,\text{GeV}^2$. In figure 5.1 the result for the measurement of the reduced CC cross section as defined in equation 1.11 is shown as a function of x in eight bins of Q^2 and compared to the Standard Model prediction. In total the measurement comprises 29 measurement bins. For the theoretical prediction the latest H1 NLO QCD fit is used. The rise of the measured cross section towards low x is well described by the H1 PDF+BCDMS 2000 fit. The results are summarised in table A.1.

In figure 5.2 the measurement of this analysis is compared to the measurement presented in [9]. Within the errors both analyses are compatible and well described by the H1+BCDMS PDF 2000 fit.

Figure 5.3 shows the ratio $((d\sigma^2/dxdQ^2)^{Data} - (d\sigma^2/dxdQ^2)^{SM})/(d\sigma^2/dxdQ^2)^{SM}$ for this analysis compared to the published results, where $(d\sigma^2/dxdQ^2)^{Data}$ is the measured CC cross section and $(d\sigma^2/dxdQ^2)^{SM}$ is the Standard Model prediction. The error bars include the total uncertainty for both measurements.

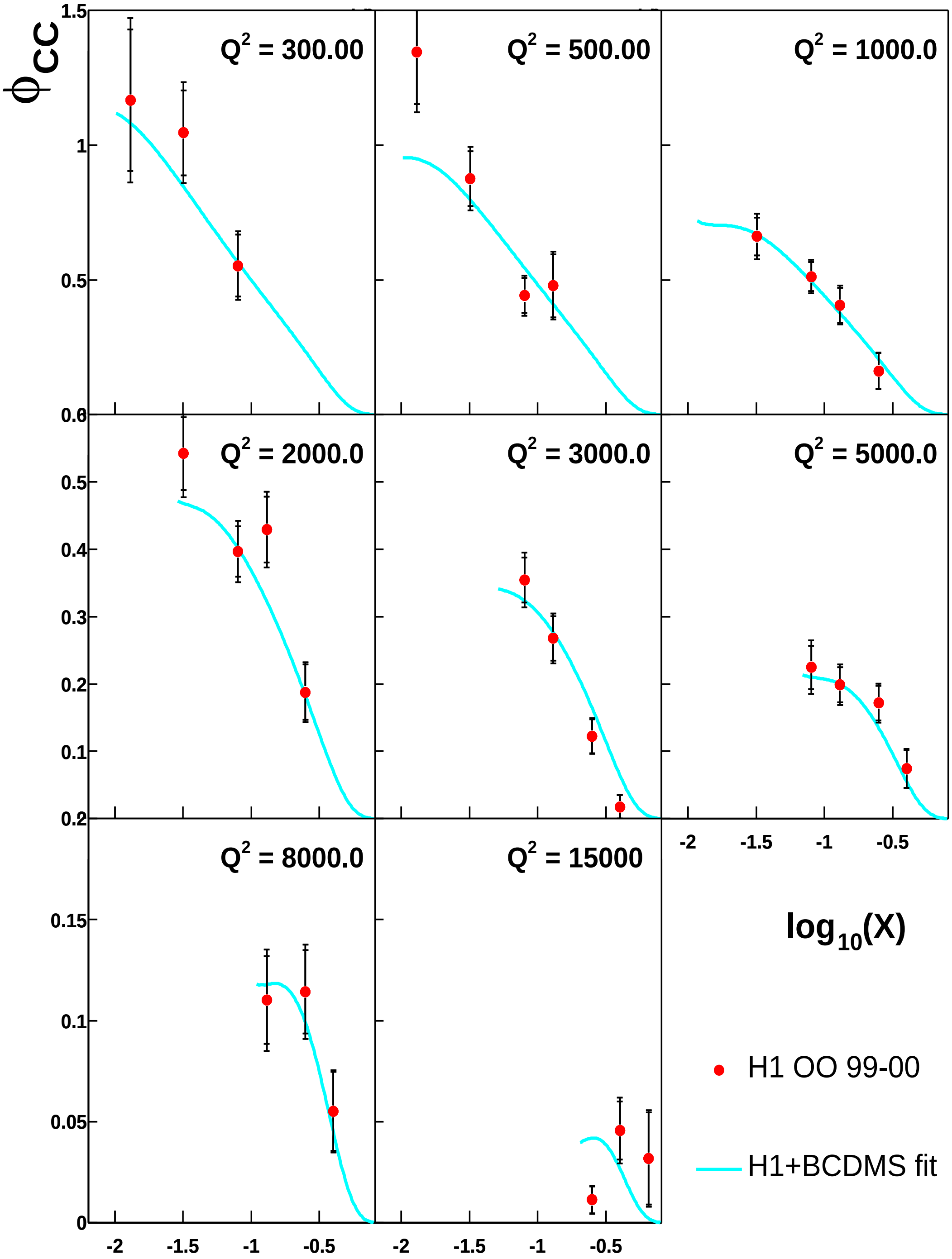

Figure 5.1: *The reduced CC cross section ϕ_{CC} as a function of x in eight bins of Q^2. Shown are data points compared to the Standard Model expectation using a NLO QCD fit to the parton distributions, H1+BCDMS PDF 2000. The fit was performed by the H1 Collaboration using H1 data combined with fixed target experiment data from BCDMS. The inner error bars correspond to the statistical uncertainties, the outer ones to the total uncertainty.*

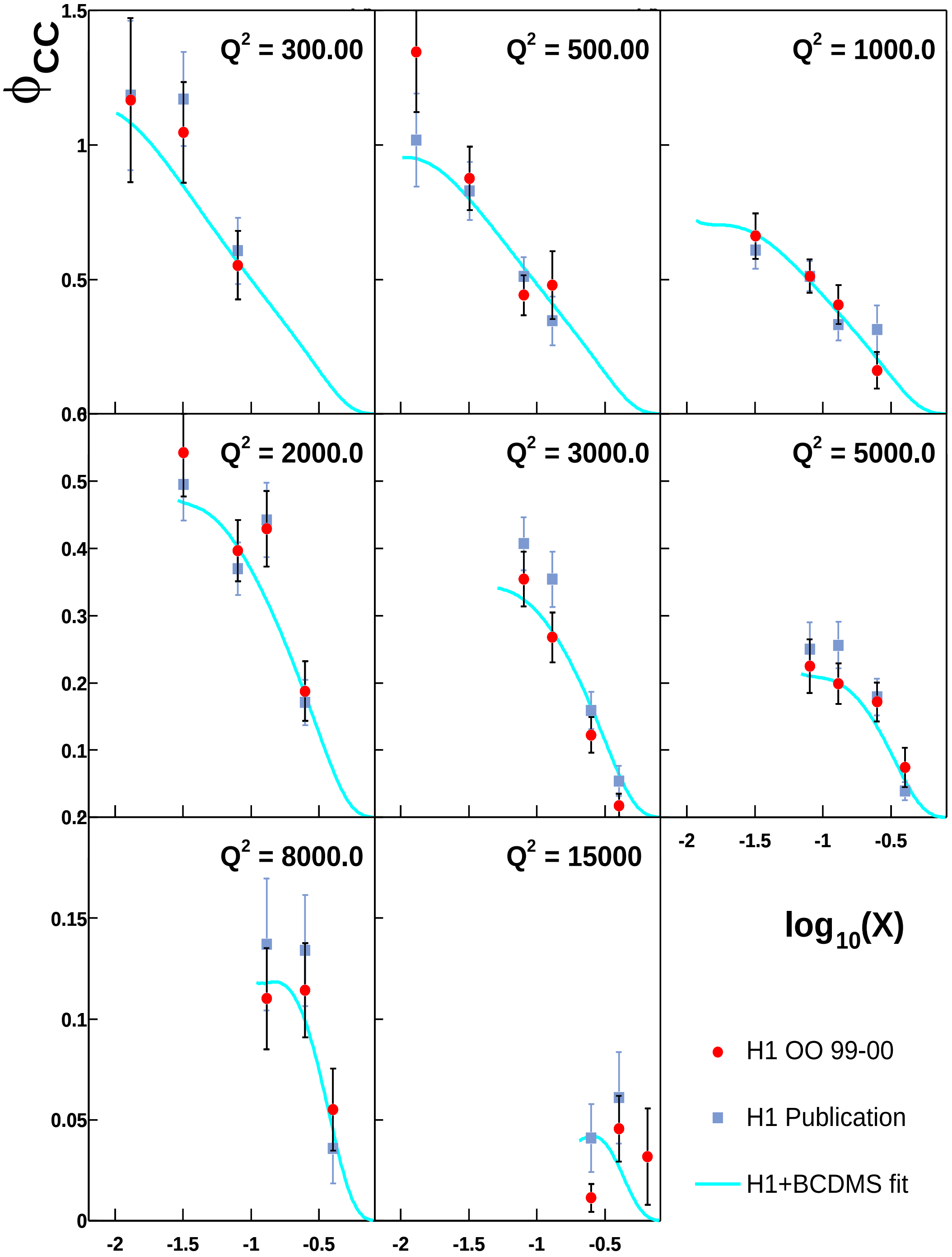

Figure 5.2: *The reduced CC cross section ϕ_{CC} as a function of x in eight bins of Q^2. Shown are data points from this analysis and from the H1 publication [9] compared to the Standard Model expectation using a NLO QCD fit to the parton distributions, H1+BCDMS PDF 2000. The fit was performed by the H1 Collaboration using H1 data combined with fixed target experiment data from BCDMS. The error bars correspond to the total uncertainty for both measurements.*

Note that the bin with the centre at $\log_{10}(x) = -0.60$ and $Q^2 = 15,000\,\mathrm{GeV}^2$ which shows the largest disagreement contains three events in this analysis and four additional events in the published one (see table A.4). The measurement point at $\log_{10}(x) = -0.19$ and $Q^2 = 15,000\,\mathrm{GeV}^2$ is not plotted in figure 5.3 because it lies off the scale at a ratio of 13.8 with an error of ± 11.2. Only two events contribute to this bin. It does not enter into the published measurement. The bin at $\log_{10}(x) = -0.4$ and $Q^2 = 3000\,\mathrm{GeV}^2$ contains one event in this analysis and seven events in the published analysis. None of the bins shows a significant discrepancy from the theory.

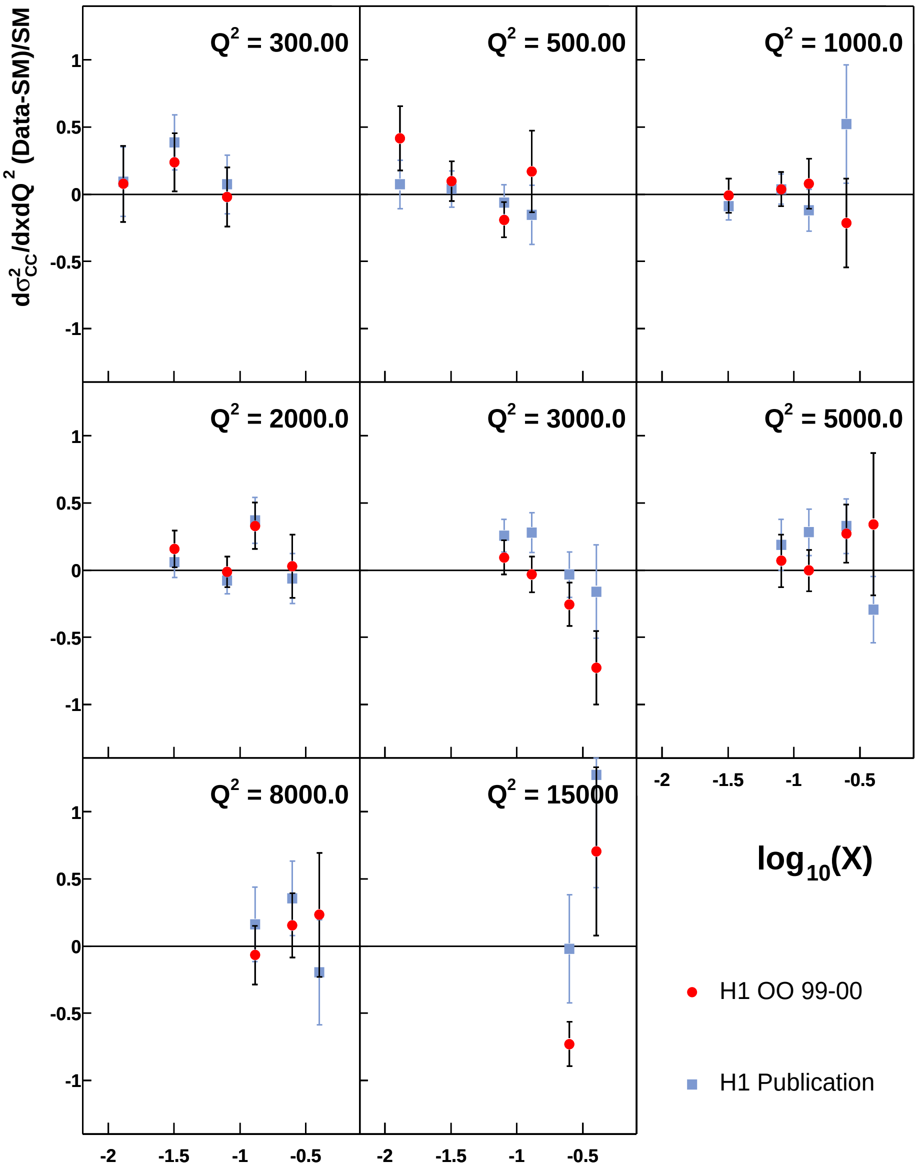

Figure 5.3: *The relative deviation of the measured CC cross section from the Standard Model prediction,* $((d\sigma^2/dxdQ^2)^{Data} - (d\sigma^2/dxdQ^2)^{SM})/(d\sigma^2/dxdQ^2)^{SM}$*, for this analysis (circles) and for the results of [9] (squares). The error bars correspond to the total uncertainty of the measurements neglecting the theoretical uncertainty.*

5.2 The Single Differential Cross Sections

The bin–to–bin correlations of the single differential cross section measurements are in general smaller than those of the double differential cross section measurement. This is due to the fact that migrations of events can only occur in one variable instead of two. Therefore purity and stability are generally larger in the individual bins. Figure 5.4 shows acceptance, purity and stability for the bins of the single differential cross sections $d\sigma_{CC}/dQ^2$ and $d\sigma_{CC}/dx$, respectively. As for the double differential cross section we require purity and stability to be greater than 30% and acceptance to be greater than 20%.

The numbers of events entering in each bin of Q^2 and x are listed in tables A.6 and A.5, respectively. They are compared to the numbers of the published measurement. The number of those events which overlap in both analyses is given.

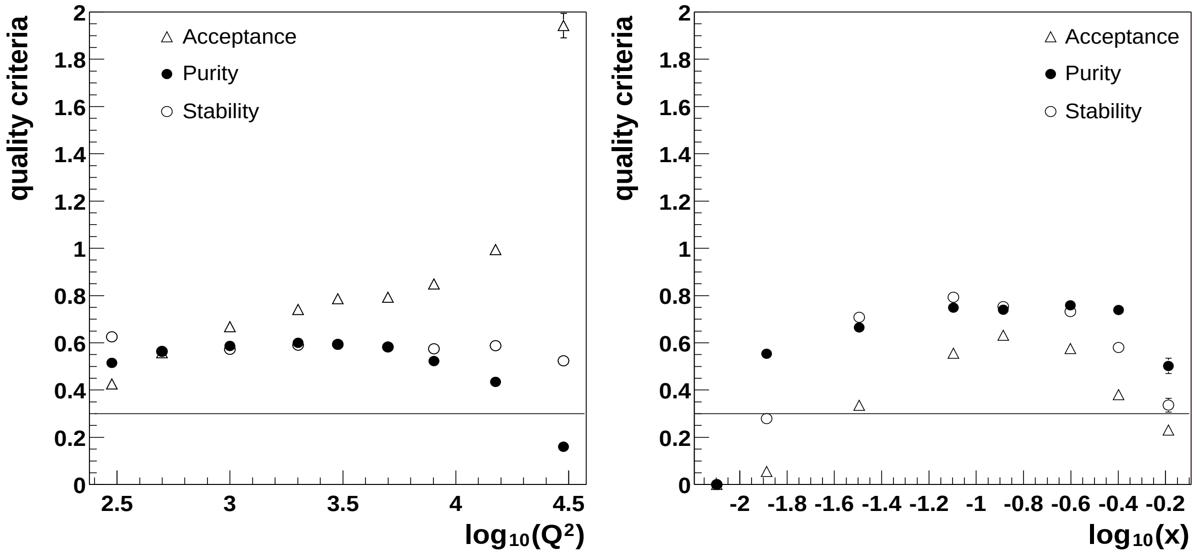

Figure 5.4: *Acceptance (triangles), purity (full circles) and stability (empty circles) for the nine bins in Q^2 and the eight bins in x. The line indicates the requirement for purity and stability to be greater than 0.3.*

5.2.1 The Q^2 Dependence of the Cross Section

The single differential cross section $d\sigma_{CC}/dQ^2$ for CC events in the kinematic region $300 \leq Q^2 \leq 15,000\,\text{GeV}^2$ is measured. Figure 5.5 shows the result of the measurement compared to the Standard Model prediction based on the H1+BCDMS PDF 2000 fit. The decline of the cross section with Q^2 is well described by the Standard Model prediction.
In order to be comparable with the measurement presented for $y < 0.9$ in [9] the CC cross section $d\sigma/dQ^2$ is corrected for the range $0.85 < y < 0.9$. The values for this correction are obtained from the NLO QCD fit. The results of the measurement are summarised in table A.2.

Figure 5.6 (a) shows the measurement of the single differential cross section $d\sigma_{CC}/dQ^2$ in comparison to the published measurement. Both measurements are in agreement with each other. In the lower part of figure 5.6 the relative deviation from the Standard Model prediction, $((d\sigma/dQ^2)^{Data} - (d\sigma/dQ^2)^{SM})/(d\sigma/dQ^2)^{SM}$, is shown. In most of the bins the agreement with the theoretical prediction has improved with this analysis.

Note that the Monte Carlo model used in this analysis is based on the cross section calculated with the CTEQ5L [52] parameterisations for the PDFs whereas for the model used in the publication MRSH [58] parameterisations are used. The total cross section in the model used for this analysis is 1.6% lower.

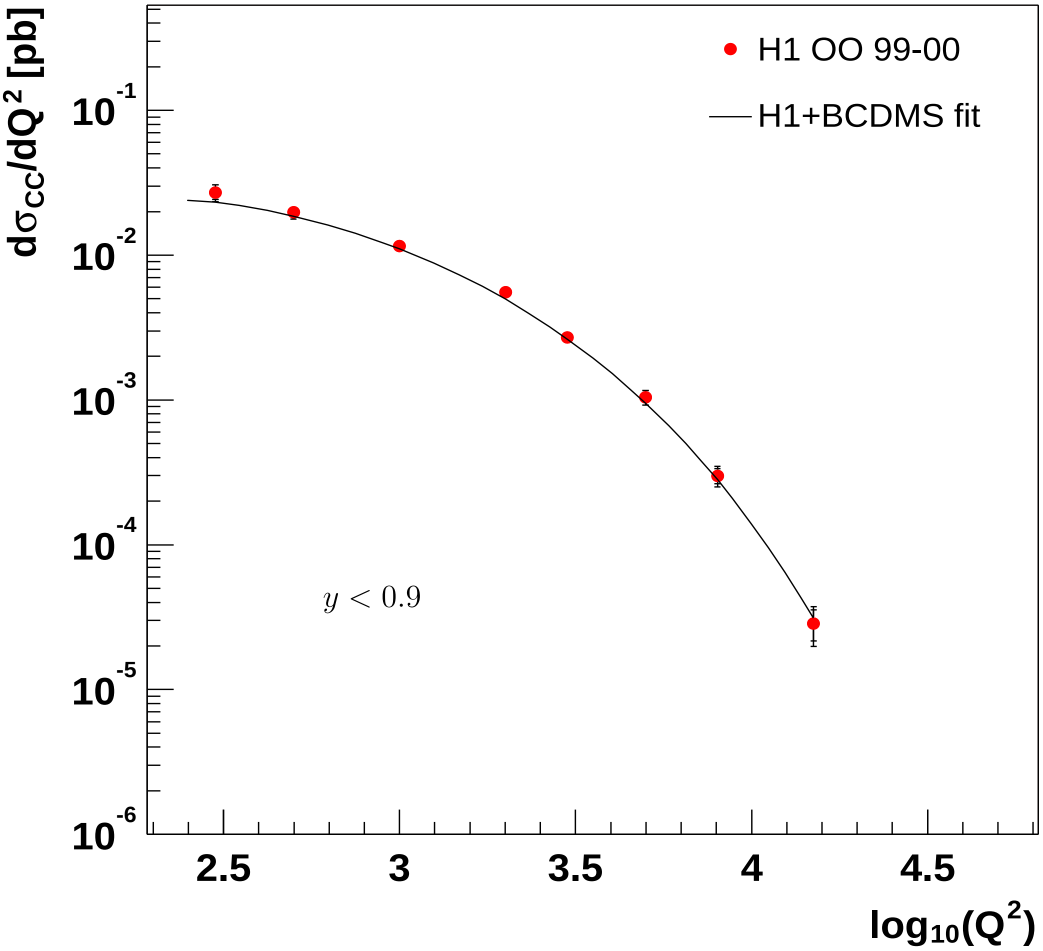

Figure 5.5: *The CC cross section as a function of Q^2. Shown are data points compared to the Standard Model expectation using the H1+BCDMS PDF 2000 fit to the parton distributions. The fit was performed by the H1 Collaboration using H1 data combined with fixed target experiment data from BCDMS. The inner error bars correspond to the statistical uncertainties, the outer ones to the total uncertainty.*

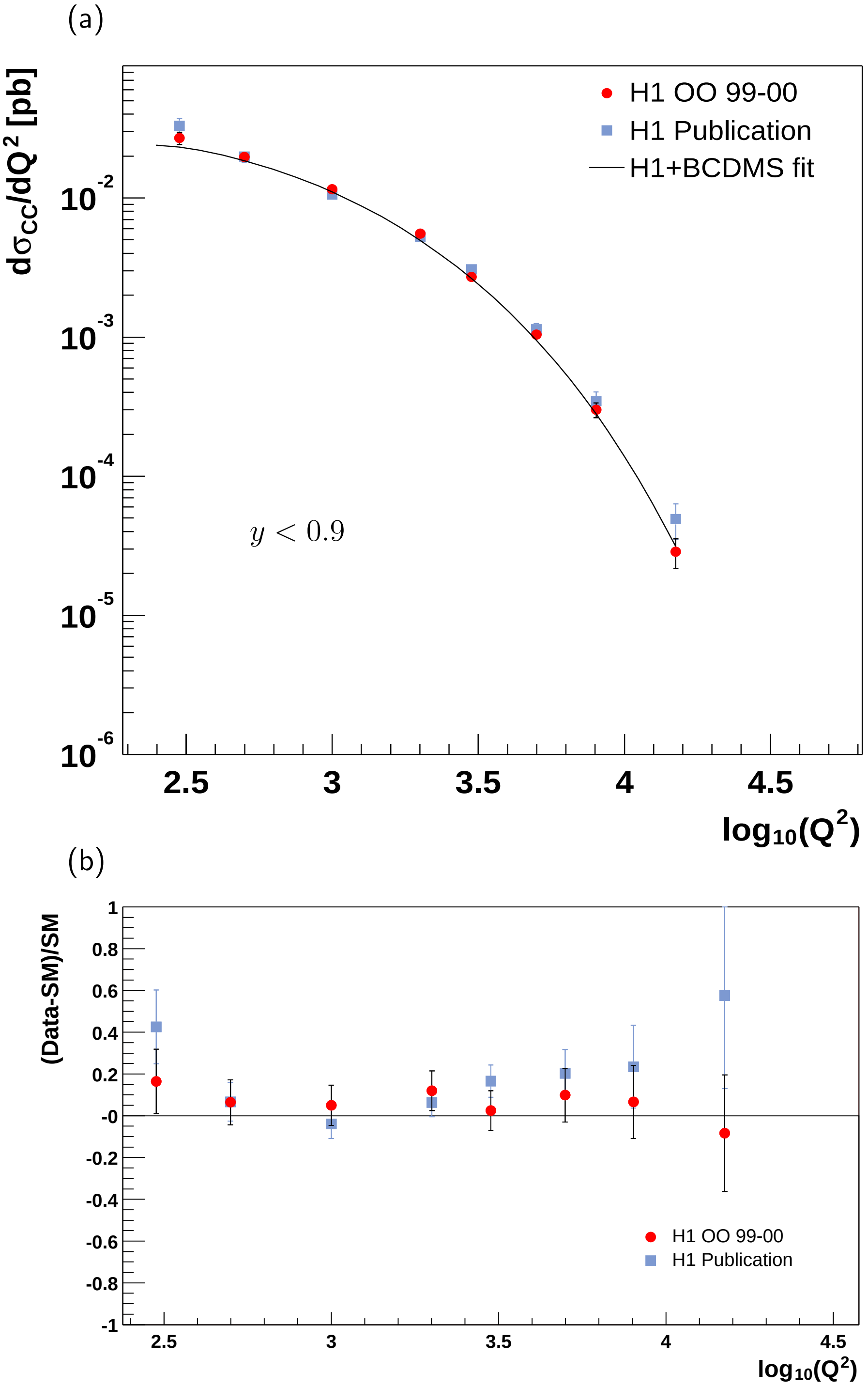

Figure 5.6: *(a) The CC cross section as a function of Q^2 compared to the H1 publication and to the H1+BCDMS PDF 2000 fit [9]. The fit was performed using H1 data combined with fixed target experiment data from BCDMS. (b) The relative deviation of the measured CC cross section from the Standard Model prediction, $((d\sigma/dQ^2)^{Data} - (d\sigma/dQ^2)^{SM})/(d\sigma/dQ^2)^{SM}$, measured in this analysis (points) and in [9] (squares). For the data points in (a) and (b) the error bars correspond to the total uncertainty of the measurements.*

5.2.2 The x Dependence of the Cross Section

The single differential cross section $d\sigma_{CC}/dx$ for CC events is measured in the kinematic region $Q^2 > 1000\,\text{GeV}^2$, $0.03 < y < 0.85$ and extrapolated to the region $y < 0.9$ using the NLO QCD fit H1+BCDMS PDF 2000. The results for six bins in x are listed in table A.3 and shown in figure 5.7. The data are in good agreement with the theoretical prediction from the NLO QCD fit. Towards low values of x the cross section rises. Due to the cuts $y < 0.9$ and $Q^2 > 1000\,\text{GeV}^2$ the curve for the Standard Model expectation decreases at very low x.

Figure 5.8 (b) shows the ratio $((d\sigma/dx)^{Data} - (d\sigma/dx)^{SM})/(d\sigma/dx)^{SM}$ for both measurements, where $(d\sigma/dx)^{Data}$ is the measured CC cross section and $(d\sigma/dx)^{SM}$ is the prediction obtained from the H1+BCDMS PDF 2000 fit. For all bins the measurements are within the corresponding errors in good agreement with the theoretical prediction.

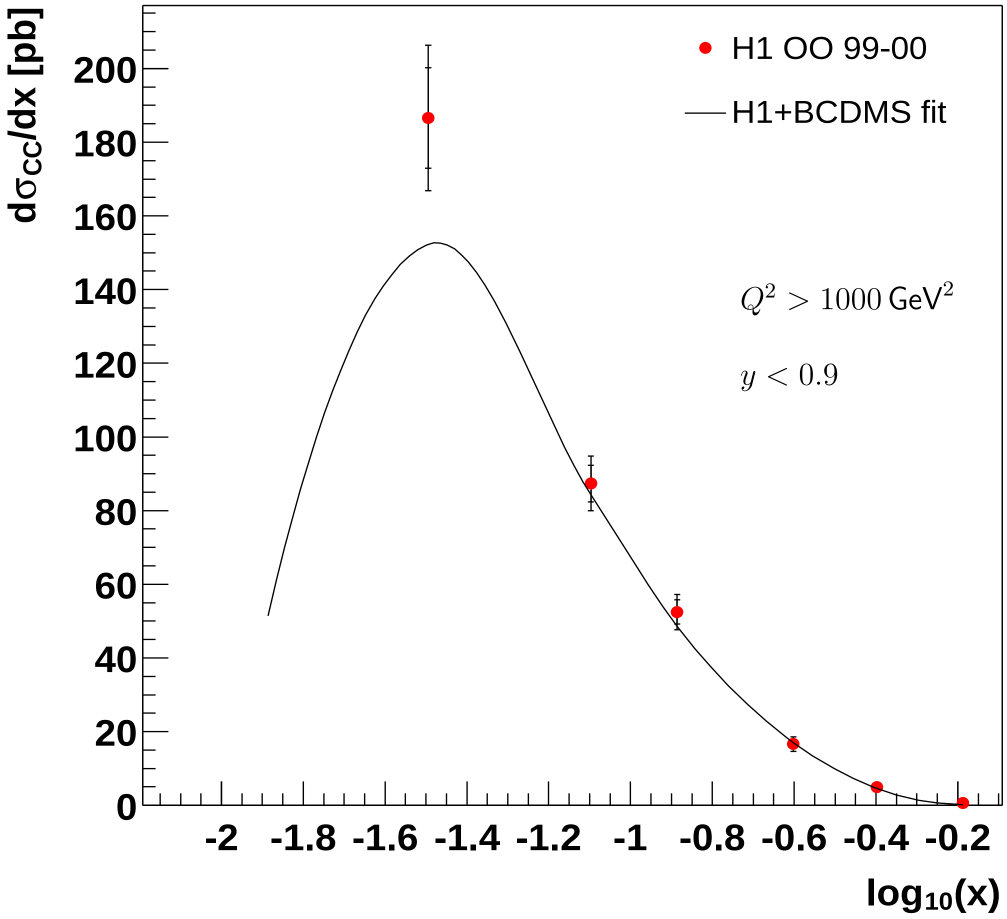

Figure 5.7: *The single differential CC cross section $d\sigma_{CC}/dx$ in six bins of x. Shown are data points compared to the Standard Model expectation using the NLO QCD fit H1+BCDMS PDF 2000 to the parton distributions. The fit was performed by the H1 Collaboration using H1 data combined with fixed target experiment data. The inner error bars correspond to the statistical uncertainties, the outer ones to the total uncertainty.*

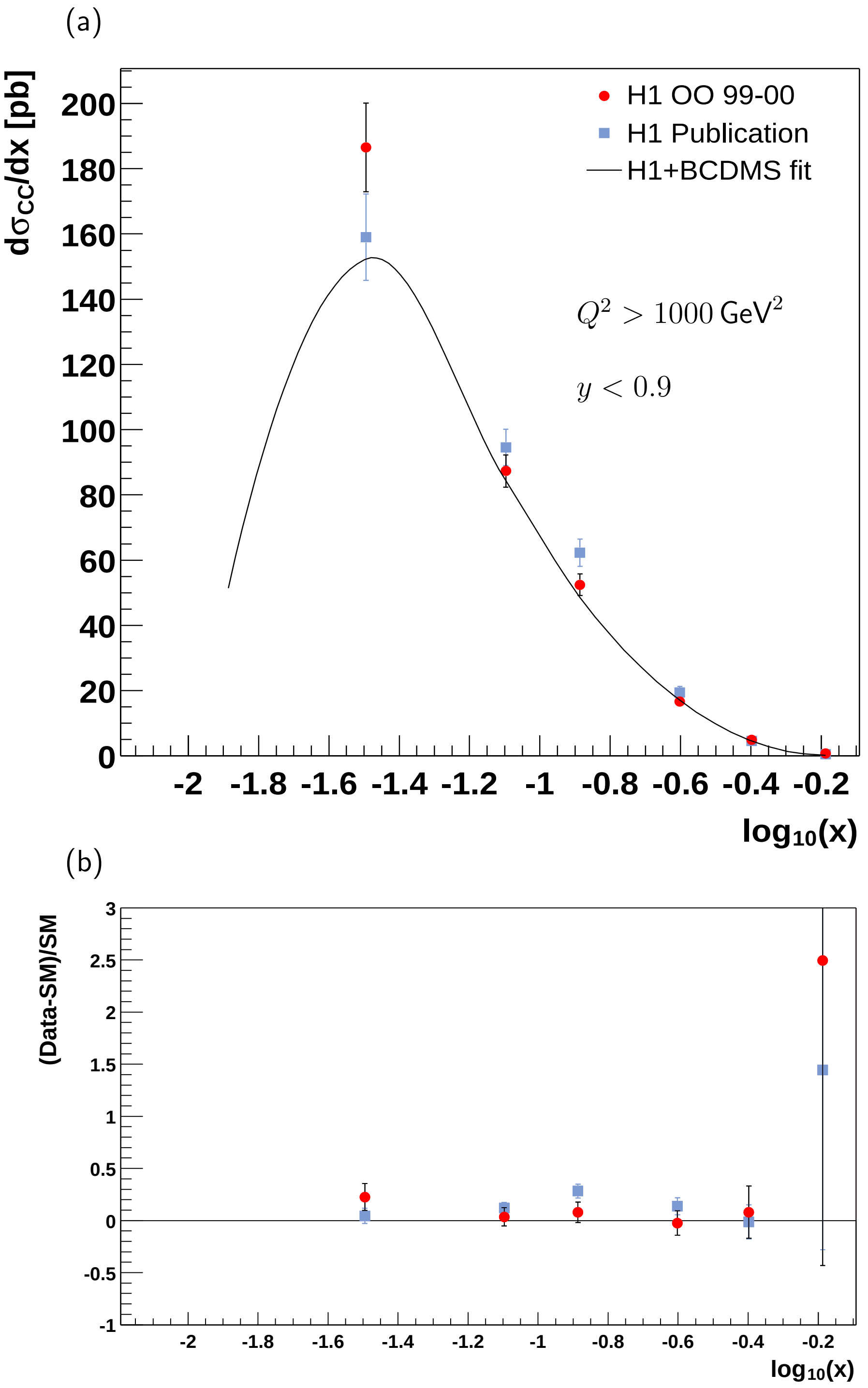

Figure 5.8: *(a) The CC cross section as a function of x compared to the H1 publication and to the H1+BCDMS PDF 2000 fit [9]. The fit was performed using H1 data combined with fixed target experiment data from BCDMS. (b) The relative deviation of the measured CC cross section from the Standard Model prediction, $((d\sigma/dx)^{Data} - (d\sigma/dx)^{SM})/(d\sigma/dx)^{SM}$, measured in this analysis (points) and in [9] (squares). For the data points in (a) and (b) the error bars correspond to the total uncertainty of the measurements.*

5.3 The Total CC Cross Section σ_{CC}^{tot}

The total CC cross section is measured in the region $Q^2 > 1000\,\text{GeV}^2$ and $y < 0.9$. For the ranges $0.85 < y < 0.9$ and $P_{T,miss} < 12\,\text{GeV}$ a small correction factor of 1.03, determined from the H1 PDF+BCDMS 2000 fit, is applied. The result is

$$\sigma_{CC}^{tot} = (18.11 \pm 0.59(stat.) \pm 1.16(sys.))\,\text{pb}.$$

This value is to be compared with the theoretical prediction from the H1 PDF+BCDMS 2000 fit of $\sigma_{CC}^{tot} = (16.77 \pm 0.32)\,\text{pb}$. The measured total CC cross section is found to deviate from the theoretical predication by 8.0%. Compared to the earlier measurement ($\sigma_{CC}^{tot} = (19.19 \pm 0.61(stat.) \pm 0.82(sys.))\,\text{pb}$) published in [9], which uses the H1 PDF 2000 fit including H1 data only, the deviation has decreased by 6.5%. Using the 97 H1 PDF fit [42] in equation 4.7 for the extraction of the cross section the total cross section increases by 2.5%.

Summary and Outlook

A study of charged current processes in deep–inelastic positron–proton scattering is presented in this thesis. At a center–of–mass energy of $\sqrt{s} = 320\,\text{GeV}$ the inclusive cross section for charged current events is measured double differentially in x and Q^2, single differentially in both of these variables and in total. The measurement is based on data collected with the H1 detector in the years 1999 and 2000 which correspond to an integrated luminosity of $\mathcal{L} = 65.25\,\text{pb}^{-1}$. For this analysis the latest reprocessed data are taken, assuring that the best understanding of the detector enters into the measurement.

The inclusive charged current cross sections are measured in the kinematic range $300 \leq Q^2 \leq 15,000\,\text{GeV}^2$ and $0.013 \leq x \leq 0.65$. The data are compared to theoretical predictions from a dedicated NLO QCD fit, H1 PDF 2000, based on DGLAP parton evolution. All cross sections show good agreement with the theoretical expectation. The results are compared to the latest H1 results published in [9]. Both measurements are found to agree within their uncertainties. The result obtained for the total charged current cross section in the kinematic range $Q^2 > 1000\,\text{GeV}^2$ and $y < 0.9$ is $\sigma_{CC}^{tot} = (18.11 \pm 0.59(stat.) \pm 1.16(sys.))$ pb. Compared to the previous measurement the deviation from the Standard Model expectation has decreased by 6.5%.

The present analysis is performed in the new $\mathrm{H1\ OO}$ framework, a new data storage and physics analysis environment based on C++. This is an important preparation for the upcoming measurement of the charged current cross section as a function of the lepton beam polarisation, a crucial test of the Standard Model. The agreement of the present analysis with former results confirms a good performance of the new analysis framework and justifies its application for future analyses.

The statistical uncertainty is still limiting the precision of the charged current cross section measurement. In the future the determination of the cross section will profit from the luminosity upgrade of the HERA accelerator and the H1 detector. The charged current cross section is particularly sensitive to the valence quark content of a proton. With higher statistics of positron– (electron–) proton collision data a precise measurement of the d– (u–) quark distribution will become possible.

Appendix A

Tables of Results

Q^2 [GeV^2]	x	$d\sigma_{CC}/dxdQ^2$ [pb/GeV^2]	ϕ_{CC}	δ_{stat} [%]	δ_{sys} [%]	δ_{tot} [%]
300	0.013	$0.693 \cdot 10^{0}$	1.167	22.4	13.5	26.2
300	0.032	$0.252 \cdot 10^{0}$	1.046	15.0	9.8	17.9
300	0.080	$0.534 \cdot 10^{-1}$	0.553	20.7	9.7	22.9
500	0.013	$0.754 \cdot 10^{0}$	1.345	14.3	8.5	16.7
500	0.032	$0.199 \cdot 10^{0}$	0.875	11.6	6.9	13.5
500	0.080	$0.402 \cdot 10^{-1}$	0.441	14.8	8.3	16.9
500	0.130	$0.268 \cdot 10^{-1}$	0.478	24.5	9.6	26.3
1000	0.032	$0.131 \cdot 10^{0}$	0.661	10.7	7.0	12.8
1000	0.080	$0.406 \cdot 10^{-1}$	0.512	10.4	6.6	12.3
1000	0.130	$0.198 \cdot 10^{-1}$	0.406	15.9	8.0	17.8
1000	0.250	$0.410 \cdot 10^{-2}$	0.162	40.9	10.8	42.3
2000	0.032	$0.836 \cdot 10^{-1}$	0.542	10.0	6.5	11.9
2000	0.080	$0.245 \cdot 10^{-1}$	0.397	9.4	6.4	11.4
2000	0.130	$0.163 \cdot 10^{-1}$	0.429	11.4	6.4	13.1
2000	0.250	$0.370 \cdot 10^{-2}$	0.188	21.9	8.4	23.5
3000	0.080	$0.175 \cdot 10^{-1}$	0.354	9.4	6.7	11.6
3000	0.130	$0.812 \cdot 10^{-2}$	0.268	12.2	6.4	13.8
3000	0.250	$0.193 \cdot 10^{-2}$	0.123	20.5	7.0	21.7
3000	0.400	$0.173 \cdot 10^{-3}$	0.018	100.1	11.5	100.8
5000	0.080	$0.755 \cdot 10^{-2}$	0.225	14.2	10.6	17.8
5000	0.130	$0.411 \cdot 10^{-2}$	0.199	13.0	7.7	15.1
5000	0.250	$0.185 \cdot 10^{-2}$	0.172	14.9	8.0	16.9
5000	0.400	$0.498 \cdot 10^{-3}$	0.074	38.0	10.7	39.5
8000	0.130	$0.143 \cdot 10^{-2}$	0.110	19.7	11.4	22.8
8000	0.250	$0.772 \cdot 10^{-3}$	0.114	18.1	9.5	20.4
8000	0.400	$0.233 \cdot 10^{-3}$	0.055	35.5	9.7	36.8
15000	0.250	$0.348 \cdot 10^{-4}$	0.011	57.8	17.3	60.3
15000	0.400	$0.876 \cdot 10^{-4}$	0.046	31.7	16.2	35.5
15000	0.650	$0.375 \cdot 10^{-4}$	0.032	71.5	22.2	74.8

Table A.1: *The CC double differential cross section $d\sigma^2_{CC}/dxdQ^2$ and the reduced cross section ϕ_{CC}. The statistical uncertainty (δ_{stat}), the systematic uncertainty (δ_{sys}) and the total error (δ_{tot}) are given.*

Q^2 [GeV^2]	$d\sigma_{CC}/dQ^2$ [pb/GeV^2]	δ_{stat} [%]	δ_{sys} [%]	δ_{tot} [%]
300	$0.270 \cdot 10^{-1}$	9.9	8.8	13.3
500	$0.198 \cdot 10^{-1}$	7.3	7.0	10.1
1000	$0.116 \cdot 10^{-1}$	6.2	6.8	9.2
2000	$0.555 \cdot 10^{-2}$	5.6	6.4	8.5
3000	$0.270 \cdot 10^{-2}$	6.4	6.7	9.3
5000	$0.104 \cdot 10^{-2}$	7.9	8.6	11.7
8000	$0.300 \cdot 10^{-3}$	12.2	11.1	16.4
15000	$0.286 \cdot 10^{-4}$	24.3	18.4	30.5

Table A.2: *The CC single differential cross section* $d\sigma_{CC}/dQ^2$ *for* $y_h < 0.9$ *after correction according to the Standard Model expectation determined from the H1 PDF 2000 fit for the kinematic cuts* $0.03 < y_h < 0.85$ *and* $P_{T,h} > 12$ *GeV. The statistical uncertainty (*δ_{stat}*), the systematic uncertainty (*δ_{sys}*) and the total error (*δ_{sys}*) are given.*

x	$d\sigma_{CC}/dx$ [pb]	δ_{stat} [%]	δ_{sys} [%]	δ_{tot} [%]
0.032	$0.187 \cdot 10^{3}$	7.3	7.6	10.6
0.080	$0.873 \cdot 10^{2}$	5.6	6.4	8.5
0.130	$0.525 \cdot 10^{2}$	6.3	6.5	9.1
0.250	$0.166 \cdot 10^{2}$	8.9	7.9	11.9
0.400	$0.494 \cdot 10^{1}$	19.7	12.2	23.1
0.650	$0.670 \cdot 10^{0}$	80.0	24.6	83.7

Table A.3: *The CC single differential cross section* $d\sigma_{CC}/dx$ *for* $y_h < 0.9$ *and* $Q^2 > 1000$ *GeV*^{2} *after correction according to the Standard Model expectation determined from the H1 PDF 2000 fit for the kinematic cuts* $0.03 < y_h < 0.85$ *and* $P_{T,h} > 12$ *GeV. The statistical error (*δ_{stat}*), the total error (*δ_{tot}*) and the systematic error (*δ_{sys}*) are given.*

Q^2 [GeV^2]	x	number of events in this analysis	number of events in publication	number of common events	included in this analysis	included in publication
300	0.008	18	16	4	no	no
300	0.013	36	39	18	yes	yes
300	0.032	58	62	30	yes	yes
300	0.080	28	34	19	yes	yes
300	0.130	3	1	1	no	no
500	0.008	5	8	0	no	no
500	0.013	60	54	26	yes	yes
500	0.032	79	77	43	yes	yes
500	0.080	50	55	28	yes	yes
500	0.130	17	18	7	yes	yes
500	0.250	1	0	0	no	no
1000	0.013	48	35	16	no	no
1000	0.032	96	89	58	yes	yes
1000	0.080	95	91	61	yes	yes
1000	0.130	40	36	25	yes	yes
1000	0.250	6	18	5	yes	yes
2000	0.013	9	12	0	no	no
2000	0.032	104	100	64	yes	yes
2000	0.080	114	97	65	yes	yes
2000	0.130	79	78	48	yes	yes
2000	0.250	21	29	13	yes	yes
2000	0.400	0	1	0	no	no
3000	0.032	40	37	17	no	no
3000	0.080	114	122	78	yes	yes
3000	0.130	68	83	45	yes	yes
3000	0.250	24	37	15	yes	yes
3000	0.400	1	7	0	yes	yes
5000	0.080	50	51	29	yes	yes
5000	0.130	60	64	47	yes	yes
5000	0.250	46	48	30	yes	yes
5000	0.400	7	9	3	yes	yes
8000	0.080	3	4	0	no	no
8000	0.130	26	24	14	yes	yes
8000	0.250	31	33	24	yes	yes
8000	0.400	8	6	3	yes	yes
8000	0.650	0	1	0	no	no
15000	0.130	2	1	0	no	no
15000	0.250	3	7	3	yes	yes
15000	0.400	10	12	10	yes	yes
15000	0.650	2	1	1	yes	no

Table A.4: *The number of data events in each bin of the double differential CC cross section measurement compared for this analysis and the analysis presented in [9]. In the fifth column the number of those events which are common in both analyses is given. The last to columns show whether the bin fulfills the quality criteria or not. In all those bins which are not listed no events are found.*

Q^2 [GeV^2]	number of events in this analysis	number of events in publication	number of common events
300	143	152	85
500	212	212	127
1000	285	269	187
2000	327	317	223
3000	247	286	179
5000	163	172	123
8000	68	68	50
15000	17	21	14

Table A.5: *The numbers of data events in each bin of Q^2 compared for this analysis and the analysis presented in [9]. In the fifth column the number of those events which are common in both analyses is given.*

x	number of events in this analysis	number of events in publication	number of common events	included in this analysis	included in publication
0.008	23	24	7	no	no
0.013	153	140	94	no	no
0.032	377	365	276	yes	yes
0.080	454	454	346	yes	yes
0.130	295	305	220	yes	yes
0.250	132	172	110	yes	yes
0.400	26	35	21	yes	yes
0.650	2	2	1	yes	yes

Table A.6: *The numbers of data events in each bin of x compared for this analysis and the analysis presented in [9]. In the fifth column the number of those events which are common in both analyses is given. The last to columns show whether the bin fulfills the quality criteria or not. In all those bins which are not listed no events are found.*

Appendix B

The Upgraded Central Inner Proportional Chamber CIP2k

In the years 2000–2002 HERA and the collider experiments were upgraded in order to increase the specific luminosity by a factor between three and four. New super–conducting focusing magnets were installed inside the collider experiments and beam currents increased. Due to the additional material close to the interaction region the upgrade leads to higher background rates. Higher synchrotron radiation heating up the beam pipe and releasing gas molecules is another reason for the increased background rates. Many parts of the detectors had to be modified to cope with this new situation.

In H1 a new first level z–vertex trigger was installed in order to efficiently reject background events with an interaction vertex outside the region of ep interactions. The new trigger is based on signals from a cylindrical five–layer multiwire proportional chamber, the CIP2k which replaces the old **C**entral **I**nner **P**roportinal chamber, CIP.

In the following sections the geometry and the construction of the CIP2k chamber are discussed. The configuration of the high voltage supply and measurements of the high voltage performance are presented. Further details on the readout electronics and the z–vertex trigger can be found in [62], [63] and [64].

B.1 Mode of Operation and Construction of the CIP2k

The CIP2k is a cylindrical multiwire proportional chamber with cathode pad readout. It is situated around the H1 silicon vertex detector close to the beam pipe and surrounded by the H1 **C**entral **J**et **C**hambers CJC [1] as shown in figure B.1. The pads of five concentric layers provide space points which define the direction of tracks. Backward extrapolation of the tracks to the beam axis allows for a fast determination of the z–vertex position with a resolution of 164 mm. With this information available after 2 μs the new z–vertex trigger decides whether an event is kept as ep event or rejected as background.

---

[1] These are the central tracking chambers.

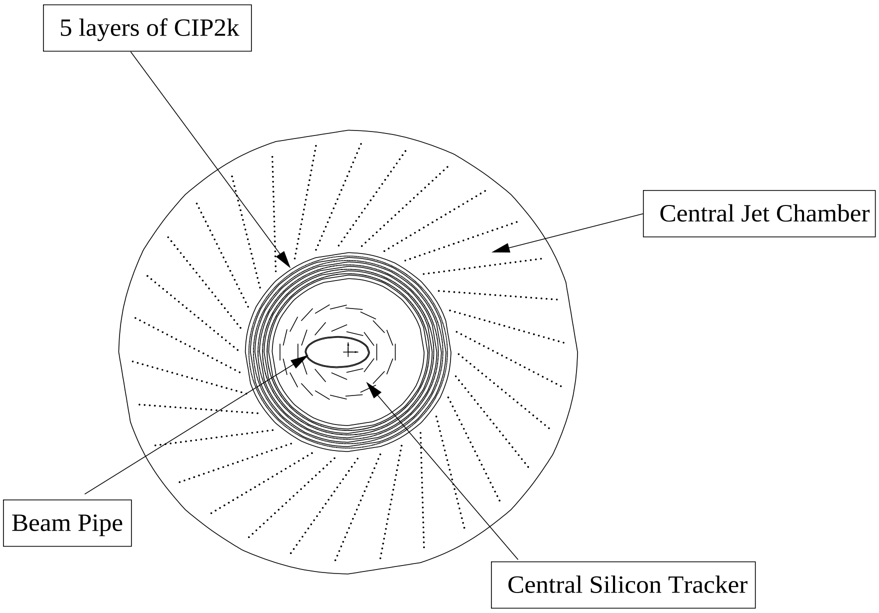

Figure B.1: *Cross section of the beam pipe and the H1 central tracking devices.*

B.1.1 Geometry of the Chamber

The five cylindrical layers of the CIP2k have an active length of 2183 mm with radii between 157 mm to 193 mm. The pads of all layers have a 16–fold segmentation in the azimuth angle ϕ. The segmentation in the z–direction of the proton beam varies for each layer giving a projective geometry [63]. The innermost layer is segmented into 119 pads with a pad length of 18.25 mm. The outermost chamber has 93 pads of 23.46 mm length. The radii and pad segmentation of all five layers are given in table B.1.

The readout electronics consisting of 16 boards for each layer, connectors for high voltage supply and gas supply lines are all situated at the $-z$ end of the chamber.

Layer	Radius [mm]	Number of Pads in z	Pad Length [mm]
0	157	119	18.25
1	166	112	19.32
2	175	106	20.53
3	184	99	21.90
4	193	93	23.46

Table B.1: *Radii and pad segmentation of the five cylindrical layers of anode pads.*

B.1.2 Readout Electronics

The total number of readout channels is 9600. In a custom designed chip named CIPix [65] groups of 60 channels are read out, amplified, shaped, digitised and multiplexed. Each of the 5x16x2=160 chips reads out either the $-z$ or the $+z$ half of a ϕ–sector of one layer. Groups of two CIPix chips are mounted on 80=5x16 readout boards. The multiplexed signals of two boards together are sent via 40 optical links to the trigger electronics outside the detector [63].

B.1.3 Mechanical construction

The five–layer CIP2k consists of six concentric cylinders. From inside to outside the first layer starts with a wire layer, the following layers continue with a pad and a wire layer each up to the sixth layer with pads only. The same handling of materials and formation of cylinders on a steel mandril as used in the construction of the old CIP was adopted [26]. From inside to outside the innermost layer is constructed as follows:

- **Electromagnetic shielding:** A 10 μm aluminum foil serves as electromagnetic shielding at the inside of each layer.
- **Rohacell support:** A 1 mm Rohacell foam around the aluminum shielding serves as mechanical support.
- **Cathode**: The inner cathode is formed by a second 25 μm thick aluminum foil around the Rohacell foam.
- **Anode wires:** With a spacing of 2 mm 480 anode wires out of gold plated tungsten of 25 μm diameter are strung around the cylinder.

The second cylinder forms the outer cathode of the first chamber and the inner cathode of the third cylinder. The same principle holds for the next four cylinders which form the outer cathode for the previous cylinder and the inner cathode for the next cylinder. The construction of the second, third, forth and fifth cylinder is depicted in figure B.2 and in the following described from the inside to the outside.

- **Readout pads**: The induced signals on a carbon film cathode couple through a 25 μm thick kapton foil on to the copper signal pads of 10 μm thickness. The cathode is formed by carbon of a resistance of 550-600 kΩ/m^2.
- **Rohacell support and readout cables:** The carbon cathode with readout pads is surrounded by 2 mm of Rohacell foam. Above each pad a hole is punched into the Rohacell foam for the connection to the readout cable and undercuts parallel to the z–axis are milled out of the Rohacell for the cable ducts. A shielded coaxial cable is connected to each pad and lead through the ducts to the $-z$ end.

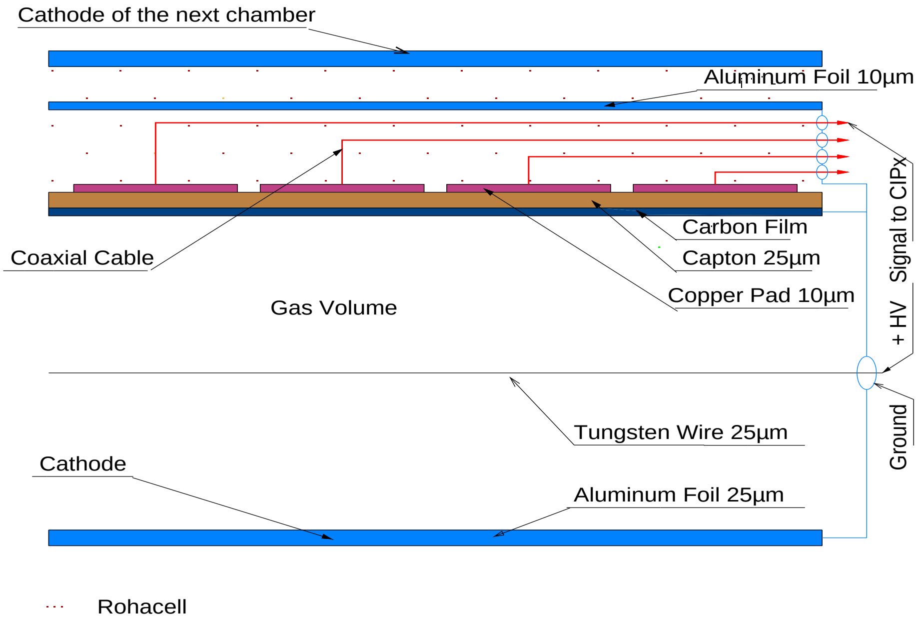

Figure B.2: *Construction of the four middle cylinders of the CIP2k.*

- **Electrical Shielding:** Final plugging of the cables in their canals with Araldite provides isolation of the contacts to the pads. From here on the construction continues as for the first layer starting with a $10\,\mu$m thick aluminum foil as electromagnetic shielding surrounded by 1 mm of Rohacell.

The spacing between the anode wires increases up to 2.5 mm in the outermost layer. The construction of the sixth layer is the same as for the four middle layers but ends with the 10 μm thick aluminum foil.

At both ends O-ring gaskets seal the chamber. At the $-z$ end connectors for high voltage supply are connected to the anode wires. The 25 μm aluminum cathodes and the carbon cathodes are grounded. The readout cables of each ϕ–sector are connected to a connector of 120 channels on which finally a board with two CIPix chips is mounted.

A sketch of the final assembly of all five layers on a carbon fibre reinforced plastic (CFK) cylinder is shown in figure. B.3.

B.1.4 The gas system

The gas inlets are situated at the $-z$ end. The gas volume of the CIP2k is separated into two parts. One closed loop is built by the inner two layers and the other one by the outer three layers as can be seen in figure B.4. The inner volume has an inlet, an outlet and an access for pressure measurement. The outer volume has two gas inlets.

The CIP2k is operated with the same gas mixture as the old CIP. It is consists of Argon, Ethane and Freon in the ratio of $49.9\% : 49.9\% : 0.2\%$.

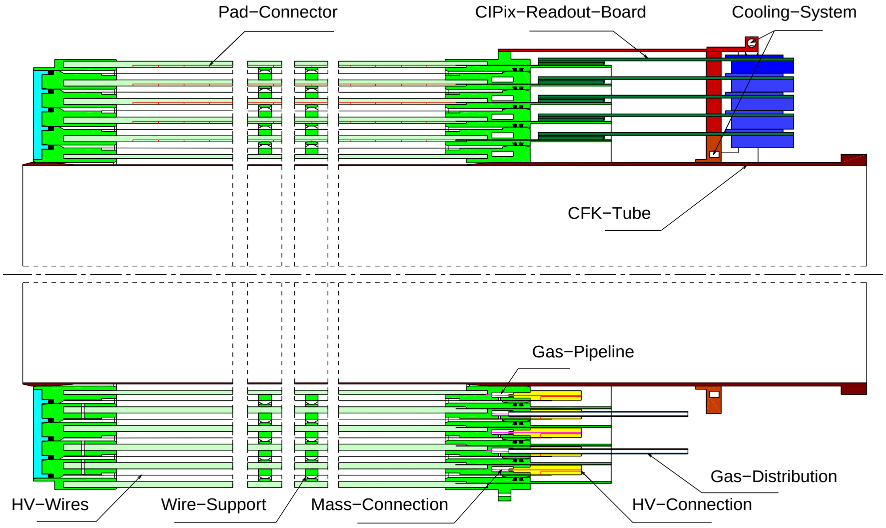

Figure B.3: *Final assembly of the five CIP2k layers on a CFK cylinder with all connectors.*

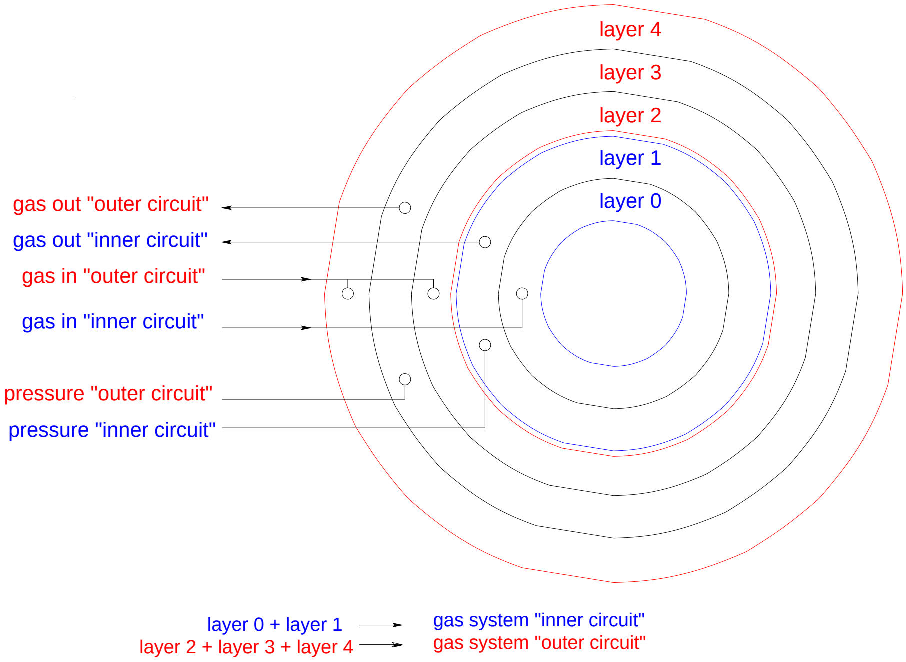

Figure B.4: *The two gas volumes of the CIP2k with inlets, outlets and access for pressure measurement.*

B.2 High Voltage

B.2.1 High Voltage Supply

The 480 anode wires of each layer are connected to each neighbour with an 1 MΩ resistor and grouped into 32 sectors. Groups of 15 wires are connected to 32 high voltage cables via a 3.3 MΩ resistor at each end. An illustration of the high voltage supply for one layer is given in figure B.5. The 32x5=160 high voltage cables are merged in five distributor boxes such that two cables at a time can be supplied by one high voltage channel out of a CAEN high voltage crate. Thus, only two crates of 40 channels are needed to provide positive high voltage to all 480x5=2400 anode wires of the CIP2k.
This arrangement of anode wires and high voltage cables allows a voltage degrading in case of a broken wire with a corresponding short circuit between anode and cathode. In an optimal case where only one wire is broken in a group of 15 only 1 1/2 ϕ–sectors are affected by the degrading.

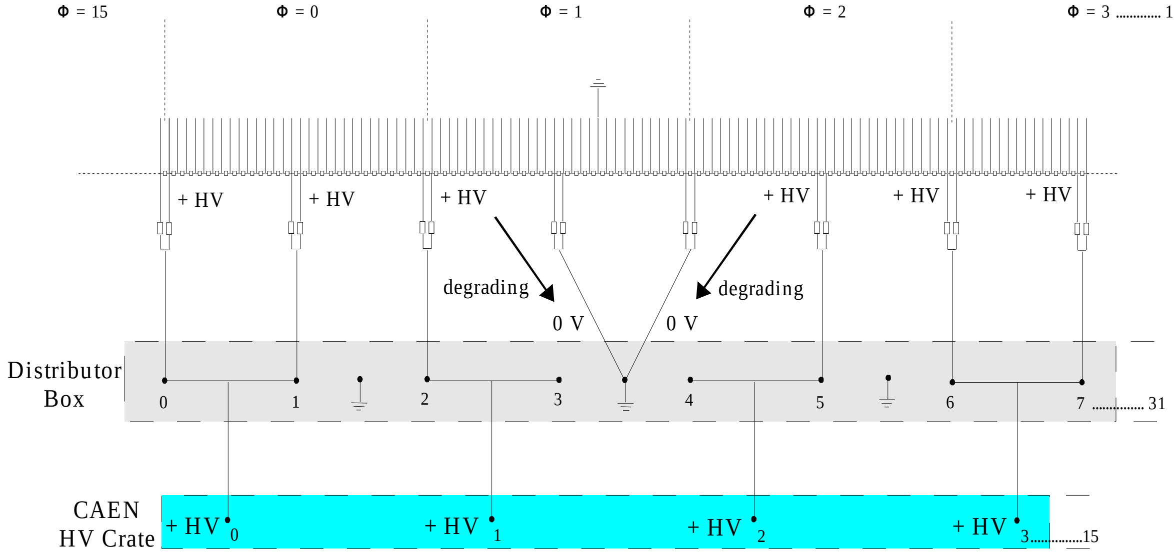

Figure B.5: *High voltage supply configuration. The high voltage degrading for a broken wire in sector $\phi = 1$ is shown.*

B.2.2 High Voltage Performance

The measured efficiency of the CIP2k as a function of the high voltage is shown in figure B.6. The measurement was performed outside the H1 detector for a single pad of the outermost layer with a Ruthenium source and two scintillation counters. Inside the H1 detector the efficiency was measured with cosmic muons. The data were taken in dedicated cosmic muon runs in October 2003. The measurement was performed by extrapolating single muon tracks

from the CJC to each layer of the CIP2k.
Only those events are considered in which two CJC tracks in opposite hemispheres are found to match in θ and ϕ and can be fitted to one single cosmic track. In addition the two opposite tracks are required to have a distance of closest approach to the nominal z–axis, $d_{ca} < 10\,$cm, and a transverse momentum, $p_t > 0.5\,$GeV. All events found within $\pm 30\,$ns of the nominal event timing (bunch crossing) and with exactly two CJC tracks fulfilling the track requirements are accepted for the measurement.
A CJC track was considered to be measured by the CIP2k if a signal from a pad in a z–region of five pads on either side of the extrapolated CJC track was measured.

With increasing high voltage the gain of the chamber increases up to a maximum gain where a plateau of the efficiency curve is reached. The working voltage is taken to be at the beginning of this plateau. In figure B.6 the plateau is reached for all layers and the actual working voltage of each layer is indicated by larger markers. The decreased working voltage from inside to outside arises from the increased wire spacings.

The comparison to the single pad efficiency in layer 4 shows a shift of the plateau to higher voltages for the measurement over all pads because the CIPix parameters, preamplifier and shaper currents for instance, are not the same in both measurements. The absolute value of the efficiency depends on the adjustment and the efficiency of the readout electronics. For figure B.6 all sectors where the CIPix chips did not work properly are excluded from the measurement. However, inefficient single channels still enter into the measurement. In layer 3 the overall efficiency is lowest due to inefficient readout chips.

Figure B.7 shows the z dependence of the efficiency for all layers at the working voltage of $2450\,$V in layer 0 decreasing in steps of $50\,$V for each following layer. The median over ϕ is plotted for each bin in z. Again, all sectors where the CIPix chips did not work are excluded from the measurement. However, inefficient CIPix chips and broken channels enter into the measurement. For all layers except for the third the efficiency exceeds 92% for the median over z. In the third layer the median over z for the efficiency is 88.5%. The optimisation of the CIP efficiency is an ongoing task.

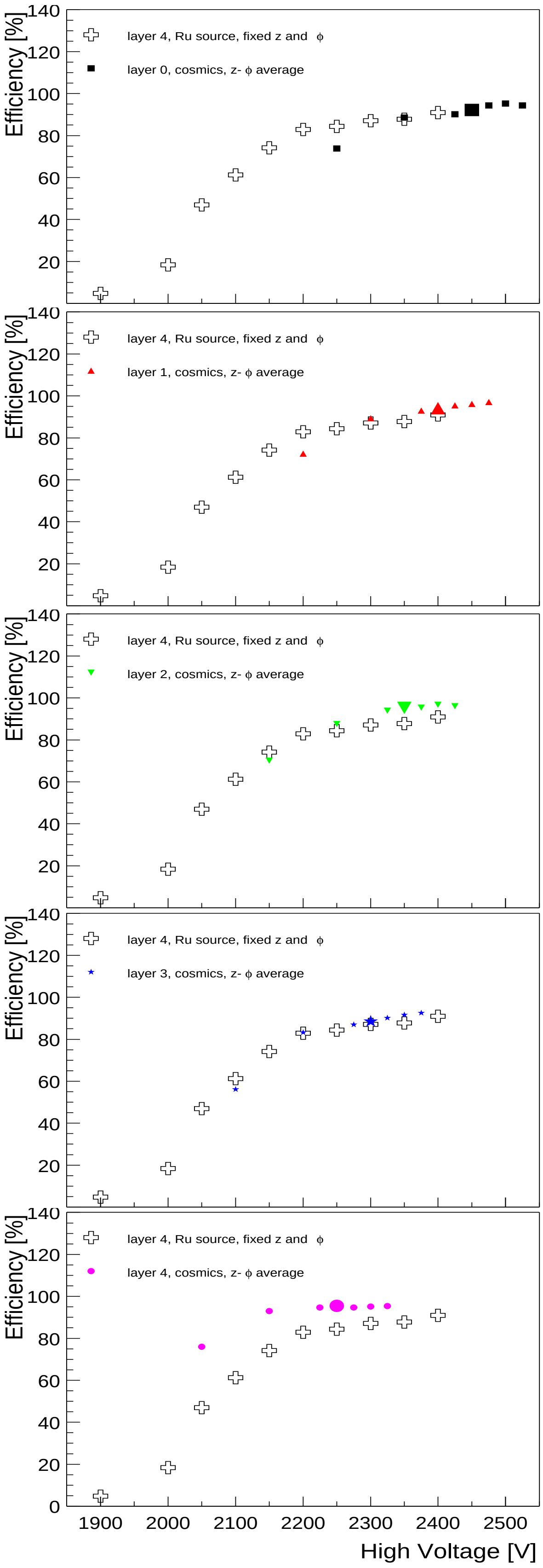

Figure B.6: *Result of the efficiency measurements for each layer compared to the measurement for a single pad in the outermost layer with a Ruthenium source. The working voltage for each layer is indicated by a larger marker.*

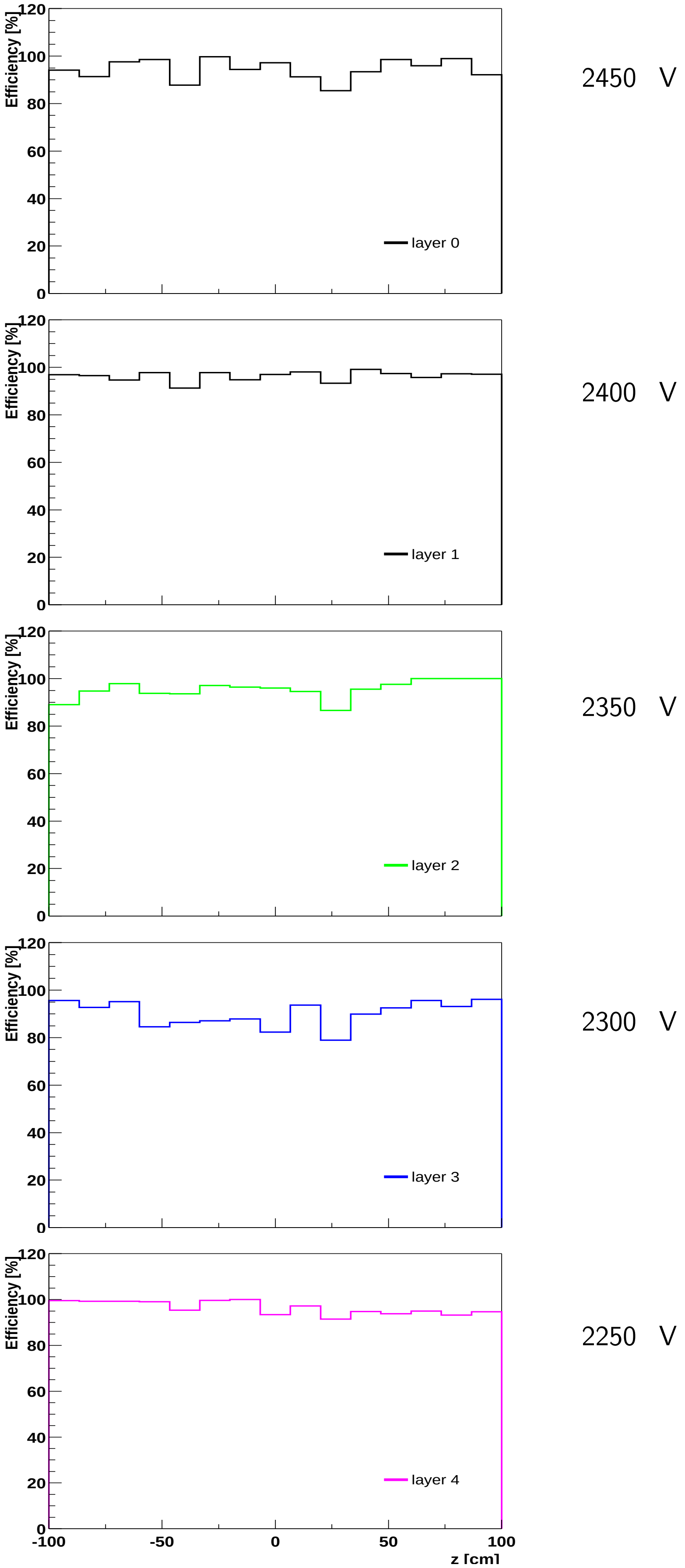

Figure B.7: *The z dependence of the efficiency for all five layers of the CIP2k at their working voltages.*

Bibliography

[1] **BEBC WA59 Collaboration, K. Varvell et al.**
Measurement of the Structure Functions F_2 and xF_3 and Comparison With QCD Predictions Including Kinematical and Dynamical Higher Twist Effects,
Z. Phys. C36 (1987) 1.

[2] **BCDMS Collaboration, A. C. Benvenuti et al.**
A High Statistics Measurement of the Proton Structure Functions F(2) (X, Q^2) and R From Deep Inelastic Muon Scattering at High Q^2,
Phys. Lett. B223 (1989) 485.

[3] **CCFR Collaboration, P. Z. Quintas et al.**
A Measurement of Λ_{QCD} from $\nu_\mu - -Fe$ Nonsinglet Structure Functions at the Fermilab Tevatron,
Phys. Rev. Lett. 71 (1993) 1307.

[4] **L. W. Whitlow, E. M. Riordan, S. Dasu, S. Rock and A. Bodek**
Precise measurements of the proton and deuteron structure functions from a global analysis of the SLAC deep inelastic electron scattering,
Phys. Lett. B282 (1992) 475.

[5] **New Muon Collaboration, M. Arneodo et al.**
Measurement of the proton and the deuteron structure functions, F2(p) and F2(d),
Phys. Lett. B364 (1995) 107.

[6] **E665 Collaboration, M. R. Adams et al.**
Proton and deuteron structure functions in muon scattering at 470 GeV,
Phys. Rev. D54 (1996) 3006.

[7] **H1 Collaboration, S. Aid et al.**
Measurement of the Q^2 dependence of the Charged and Neutral Current Cross Sections in ep Scattering at HERA,
Phys. Lett. B379 (1996) 319.

[8] **ZEUS Collaboration, J. Breitweg et al.**
Measurement of High Q^2 Charged–Current e^+p Deep Inelastic Scattering Cross Sections at HERA,
Eur. Phys. J. C12 (2000) 411, [Erratum-ibid. C27 (2003) 305].

[9] **H1 Collaboration, C. Adloff et al.**
Measurement and QCD Analysis of Neutral and Charged Current Cross Sections at HERA,
Eur. Phys. J. C30 (2003) 1.

[10] **ZEUS Collaboration, S. Chekanov et al.**
ZEUS next–to–leading–order QCD analysis of data on deep inelastic scattering,
Phys. Rev. D67, 012007 (2002).

[11] **J. Rauschenberger**
Prozesse des geladenen Stromes in tiefunelastischer Positron–Proton Streuung bei HERA,
Dissertation, Fachbereich Physik der Universität Hamburg, 2002.

[12] **Z. Zhang**
Nouveaux aspects de la structure du proton avec le collisionneur HERA,
Habilitation, Université de Paris–Sud, Centre d'Orsay, 2000.

[13] **R. K. Ellis, W. J. Stirling and B. R. Webber**
QCD and Collider Physics,
Cambridge University Press, 1996.

[14] **R.G. Roberts**
The Structure of the Proton,
Cambridge Univeristy Press, 1990.

[15] **S.L. Glashow**
Partial Symmetries of Weak Interactions,
Nucl. Phys. 22, 597 (1961),
S. Weinberg
A Model of Leptons,
Phys. Rev. Lett. 19, 1264 (1967),
A. Salam
Weak and electromagnetic interactions,
Proc. of the 8th Nobel Symposium on 'Elementary particle theory, relativistic groups and analyticity', Stockholm, Sweden, 1968, edited by N. Svartholm, 367.

[16] **J. Blümlein et al.**
Structure Functions, Quark Distributions and Λ_{QCD} at HERA,
Proceedings of the HERA WORKSHOP, Vol.1, ed. R.D. Peccei, Hamburg 1989.

[17] **M. Bloom et al., M. Breidenbach et al.**
Observed Behavior Of Highly Inelastic Electron–Proton Scattering,
Phys. Rev. Lett. 23 (1969) 935.

[18] **H1 Collaboration, C. Adloff et al.**
Measurement of Charged and Neutral Current Cross Sections in Electron–Proton Collisions at high Q^2,
Eur. Phys. J. C19 (2001) 269.

[19] **A. Mehta** *Private communication*

[20] **D. J. Fox et al.**
Test Of Scale Invariance In High–Energy Muon Scattering,
Phys. Rev. Lett. 33 (1974) 1504.

[21] **Yu. L. Dokshitzer**
Calculation Of The Structure Functions For Deep Inelastic Scattering And e^+e^- Annihilation By Perturbation Theory In Quantum Chromodynamics,
Sov. Phys. JETP 46 (1977) 641 (In Russian).
V. N. Gribov and L. N. Lipatov
Deep Inelastic E P Scattering In Perturbation Theory,
Sov. J. Nucl. Phys. 15 (1972) 438.
e^+e^- Pair Annihilation And Deep Inelastic E P Scattering In Perturbation,
Sov. J. Nucl. Phys. 15 (1972) 675.
G. Altarelli, G. Parisi
Asymptotic Freedom In Parton Language,
Nucl. Phys. B126 (1977) 298.

[22] **A. D. Martin, W. J. Stirling, R. G. Roberts, R. S. Thorne**
MRST2001: Partons and alpha(s) from precise deep inelastic scattering and Tevatron jet data,
Eur. Phys. J. C23 (2002) 73.

[23] **J. Pumplin et al.**
New generation of parton distributions with uncertainties from global QCD analysis,
JHEP 0207 (2002) 012. see also: The Coordinated Theoretical–Experimental Project on QCD,
http://www.phys.psu.edu/ cteq.

[24] **H1 Collaboration, I. Abt et al.**
The H1 detector at HERA,
Nucl. Instrum. Meth. A386 (1997) 310.

[25] **H1 Collaboration, I. Abt et al.**
The Tracking, calorimeter and muon detectors of the H1 experiment at HERA,
Nucl. Instrum. Meth. A386 (1997) 348.
See also: *http://www-h1.desy.de/h1/www/h1det/list.html.*

[26] **K. Müller et al.**
Construction and Performance of a Thin Cylindrical Multiwire Proportional Chamber with Cathode Pad Readout for the H1–Experiment,
Nucl. Instrum. Meth. A312 (1992), 457.

[27] **S. Egli et al.**
The Central Inner Z Drift Chamber Of The H1 Experiment,
Nucl. Instrum. Meth. A283 (1989) 487.

[28] **J. Haack**
Calibration of the Outer z Drift Chamber of the H1 Experiment,
DESY–ZEUTHEN–94–03.

[29] **J. Burger et al.**
The Central Jet Chamber of the H1 Experiment,
Nucl. Instrum. Meth. A279 (1989) 217.

[30] **S. Burke et al.**
Track Finding and Fitting in the H1 Forward Track Detector,
Nucl. Instrum. Meth. A373 (1996) 227.

[31] **B. Andrieu et al.**
Electron/Pion Separation with the H1 LAr Calorimeters,
Nucl. Instrum. Meth. A344 (1994) 492.

[32] **W. Hildesheim, V. Riech, M. Seidel**
The PLUG Calorimeter User's Guide,
H1-IN-372(08/1994).

[33] **H1 Collaboration**
http://www-h1.desy.de/trigger/.

[34] **V. Shekelyan**
Simulation and Reconstruction in H1 Liquid Argon Calorimetry
Internal Report H1-IN-288(04/1993).

[35] **R. Brun, F. Rademakers**
ROOT: An Object Oriented Data Analysis Framework,
Nucl. Instrum. Meth. A389 (1997) 81,
http://root.cern.ch.

[36] **R. Brun, O. Couet, C. E. Vandoni, P. Zanarini**
PAW: A General Purpose Portable Software Tool for Data Analysis and Presentation,
Comput. Phys. Commun. 57 (1989) 432.

[37] **The H1 OO Group**
https://www-h1.desy.de/icas/oop/2.4.20/oo.ps.gz.

[38] **P. Laycock**
A Measurement of the Diffractive Reduced Cross–Section $\sigma_r^{D(3)}$ at High Q^2 with the H1 Detector at HERA,
Dissertation, University of Liverpool, 2003.

[39] **H1 Collaboration**
The H1PHAN manual, version 2.03/11,
https://www-h1.desy.de/icas/imanuals/h1phan/h1phaninfo.html.

[40] **A. Blondel, F. Jacquet**
Proceedings "Study of an ep Facility for Europe", ed. U. Amaldi, DESY 79-48 (1979) 391.

[41] **H1 Collaboration, C. Adloff et al.**
Diffraction Dissociation in Photoproduction at HERA,
Z. Phys. C74 (1997) 221.

[42] **H1 Collaboration, C. Adloff et al.**
Measurement of Neutral and Charged Current Cross-Sections in Positron–Proton Collisions at Large Momentum Transfer,
Eur. Phys. J. C13 (2000) 609.

[43] **B. Heinemann**
Measurement of Charged Current and Neutral Current Cross Sections in Positron–Proton Collisions at $\sqrt{s} \approx 300\,\text{GeV}$,
Dissertation, Fachbereich Physik der Universität Hamburg, 1999.

[44] **O. Henshaw**
Calibration methods at H1,
talk presented at H1 Cross Talk, Hamburg, October 2002,
https://www-h1.desy.de/ipublications/crosstalk/2002/henshaw.ps.gz,
thesis in preparation.

[45] **G. A. Schuler and H. Spiesberger**
Proceedings of the Workshop "Physics at HERA", vol. 3, eds. W. Buchmüller, G. Ingelmann, DESY (1992) 1419.

[46] **T. Sjöstrand**
High–Energy Physics Event Generation with PYTHIA 5.7 and JETSET 7.4,
Comput. Phys. Commun. 82 (1994) 74,
see also: *http://www.thep.lu.se/tf2/staff/torbjorn/Pythia.html.*

[47] **R. Brun et al.**
GEANT3 User's Guide,
CERN-DD/EE-84-1 (1987).

[48] **G. Ingelmann**
Proceedings of the Workshop "Physics at HERA", vol. 3, eds. W. Buchmüller, G. Ingelmann, DESY (1992) 1366.

[49] **H. Spiesberger**
HERACLES and DJANGOH: Event Generation for ep Interactions at HERA Including Radiative Processes,
Fakultät für Physik, Universität Bielefeld, Germany (1998), unpublished,
http://www.desy.de/ hspiesb/djangoh.html.

[50] **T. Sjöstrand and M. Bengtsson**
The Lund Monte Carlo for Jet Fragmentation and e^+e^- Physics: Jetset Version 6.3: An

Update,
Comput. Phys. Commun. 43 (1987) 367.

[51] **B. Andersson, G. Gustafson, G. Ingelmann, T. Sjöstrand**
Parton Fragmentation and String Dynamics,
Phys. Rept. 97 31, 1983.

[52] **CTEQ Collaboration, H. L. Lai et al.**
Global QCD Analysis of Parton Structure of the Nucleon: CTEQ5 Parton Distributions
Eur. Phys. J. C12 (2000) 375.

[53] **M. Erdmann**
The Partonic Structure of the Photon: Photoproduction at the Lepton–Proton Collider HERA,
preprint DESY 96-090.

[54] **M. Glück, E. Reya, A. Vogt**
Photonic Parton Distributions,
Phys. Rev. D46 1973, 1992.

[55] **U. Bauer, J. A. M. Vermaseren, D. Zeppenfeld**
Electroweak Vector Boson Production in High–Energy ep Collisions,
Nucl. Phys. B375 (1992) 3.

[56] **A. Schöning**
Untersuchung von Prozessen mit virtuellen und reellen $W^{\pm}$–Bosonen am H1–Detektor bei HERA,
Dissertation, Fachbereich Physik der Universität Hamburg, 1996.

[57] **F. Keil**
Dijet Production in Charged and Neutral Current e^+p Interactions at High Q^2 at HERA,
Dissertation, Kirchhoff–Institut für Physik, Universität Heidelberg, 2001.

[58] **A. D. Martin, W. J. Stirling and R. G. Roberts**
Parton Distributions of the Proton,
Phys. Rev. D50 (1994) 6734. **H1 Collaboration, C. Adloff et al.**
Dijet Production in Charged and Neutral Current e^+p Interactions at High Q2,
Eur. Phys. J. C19 (2001) 429.

[59] **C. Veelken**
H1NonepBgFinder – Rejection of Cosmic Muon and Beam–Halo Events in the H1OO Framework,
H1-IN-603(09/ 2002).

[60] **V.Efremenko, N.Tobien**
ARMON Liquid Argon Calorimeter Monitor Program,
H1 internal note H1-IN-540(05/1998).

[61] **B. Heinemann, S.Riess, H.Spiesberger**
Radiative Corrections for Charged Current Scattering: A Comparison of Computer Codes,
Proceedings of the workshop "Monte Carlo Generators for HERA Physics", DESY (1999).

[62] **A. Vollhardt**
Entwurf und Bau einer Frontend–Steuerung für das CIP–Upgrade Projekt für H1 bei HERA,
Diploma Thesis, Physik–Institut der Universität Zürich, 2001.

[63] **M. Urban**
The new z–vertex trigger at H1 at HERA,
Dissertation, Physik–Institut der Universität Zürich, in preparation.
Ein schneller Trigger für H1 bei HERA,
Diploma Thesis, Fakultät für Physik und Astronomie, Universität Heidelberg, 1999.

[64] **K. Müller**
CIP and z–vertex Trigger Upgrade for H1,
http://www.physik.unizh.ch/groups/grouptruoel/cipupgrade/cip.html.

[65] **D. Baumeister**
Entwicklung und Charakterisierung eines ASICs zur Kathodenauslese vom MWPCs für das H1–Experiment bei HERA,
Diploma Thesis, Fakultät für Physik und Astronomie, Universität Heidelberg, 2000.

Acknowledgements

Only the endeavours of many people have made this thesis and its associated work possible, most of whom cannot be mentioned here by name. Amongst these I am particularly grateful to my collegues and friends in Hamburg and Zürich.

I wish to express my gratitude to Ueli Straumann who gave me the opportunity to work as a PhD student in his research group. I thank him for allowing me the freedom to pursue the research topics that interested me most.

Also I am indebted to Andrew Mehta who has supported my work on the physics analysis and kindly agreed to be referee of this thesis.

Many thanks to my collegues and friends who gave much time to reading this thesis, correcting mistakes and suggesting how it can be improved: Florian Keil, Stefania Xella-Hansen, Eram Rizvi, Katharina Müller and Matthew Beckingham.

Eram deserves particular thanks for providing me with all necessary knowledge about charged current analysis techniques. I would also like to thank Paul Laycock for his patience while introducing me to the world of C++ programming and all other DESY-UK group members for their readiness to include me in their work and fruitful discussions.

Thanks to the pleasant atmosphere provided by all members of the Physik-Institut, I enjoyed every short and long stay in Zürich. In particular I wish to thank Kurt Bösiger and Stefan Steiner for their help and explanations during the time of the CIP construction.

Finally, I am most grateful to my friends in Hamburg and Zürich who supported and encouraged me during the last four years, among them Annette, Christiane, Felix, Florian, Kathle, Sebastian, Seetha and Thöme.

Curriculum Vitae

Personalien:

Name:	Werner
Vorname:	Nicole
Geburtsdatum:	26.05.1972
Nationalität:	deutsch

Ausbildung:

1982–1991	Kreisgymnasium Itzehoe
1991	Abitur
1991–1992	Studium generale am *Leibniz Kolleg* Tübingen
1992–1996	Studium der Physik an der *Eberhard–Karls–Universität* Tübingen
Oktober 1994	Vordiplom in Physik
1995–1996	Studium an der *Pontificia Universidad Católica de Chile* in Santiago de Chile
1996–1999	Studium der Physik an der Universität Hamburg
1998–1999	Diplomarbeit am H1–Experiment unter der Leitung von Prof. Dr. Beate Naroska
Oktober 1999	Diplom in Physik
2000–2004	Wissenschaftliche Mitarbeit beim H1–Experiment am Physik–Institut der Universität Zürich, Dissertation unter der Leitung von Prof. Dr. Ulrich Straumann
2001–2003	Forschungsaufenthalt am DESY in Hamburg